UCLA
UCLA Electronic Theses and Dissertations

Title
Chaos, Synchronization, and Signal Detection in Systems of Coupled Inner-Ear Hair Cells

Permalink
https://escholarship.org/uc/item/2tt2j2kj

Author
Faber, Justin

Publication Date
2021

Peer reviewed|Thesis/dissertation

eScholarship.org Powered by the California Digital Library
University of California

UNIVERSITY OF CALIFORNIA
Los Angeles

Chaos, Synchronization, and Signal Detection in Systems of Coupled Inner-Ear Hair Cells

A dissertation submitted in partial satisfaction
of the requirements for the degree
Doctor of Philosophy in Physics

by

Justin Daniel Faber

2021

© Copyright by
Justin Daniel Faber
2021

ABSTRACT OF THE DISSERTATION

Chaos, Synchronization, and Signal Detection in Systems of Coupled Inner-Ear Hair Cells

by

Justin Daniel Faber
Doctor of Philosophy in Physics
University of California, Los Angeles, 2021
Professor Dolores Bozovic, Chair

Hair cells of the auditory and vestibular systems display astonishing sensitivity, frequency selectivity, and temporal resolution to external signals. These specialized cells utilize an internal active amplifier to achieve highly sensitive mechanical detection. One of the manifestations of this active process is the occurrence of autonomous motion of the hair-cell bundle. Using experimental recordings from *in vitro* preparations, we demonstrate that these spontaneous oscillations exhibit chaotic dynamics and are therefore sensitive to initial conditions. We further show, using experimental recordings and a numerical model, that chaotic dynamics enhance the ability of individual hair cells to detect weak signals.

As hair bundles under *in vivo* conditions are typically coupled to each other by overlying structures, we explore the role of this coupling on the dynamics of the system, using a combination of theoretical and experimental approaches. Our numerical model suggests that the presence of chaotic dynamics in the response of individual bundles enhances their ability to synchronize when coupled, resulting in significant improvement in the system's ability to detect weak signals. This synchronization persists even for a large frequency dispersion and when tens of oscillators comprise the system. Further, the amplitude and coherence of the active motion are not reduced upon increasing the number of oscillators. Using artificial membranes, we impose mechanical coupling on groups of live and functional hair bundles, allowing us to explore the role of coupling experimentally. Consistent with the numerical simulations of the chaotic system, synchronization occurs even for large frequency dispersion and a large number of hair cells. Further, the amplitude and coherence of the spontaneous oscillations are independent of the number of hair cells in the network. We therefore propose that hair cells utilize their chaotic dynamics to stabilize the synchronized state and avoid the amplitude death regime, resulting in collective coherent motion that could play a role in generating spontaneous otoacoustic emissions and enhance the system's ability to detect weak signals.

The dissertation of Justin Daniel Faber is approved.

Alan Garfinkel

Mayank Mehta

Shenshen Wang

Dolores Bozovic, Committee Chair

University of California, Los Angeles

2021

To my mother and father . . .

who taught me to read, count,

and be curious about how things work.

TABLE OF CONTENTS

1 Introduction **1**

2 Chaotic Hair-Cell Dynamics **5**

2.1 Introduction 5

2.2 Results 6

2.2.1 Dimensionality Test 6

2.2.2 Correlation Dimension 8

2.2.3 Poincaré Maps 10

2.2.4 Complexity and Entropy 12

2.2.5 Kolmogorov Entropy 13

2.2.6 Theoretical Model 16

2.3 Discussion 19

2.4 Experimental Techniques 20

2.5 Appendix 21

2.5.1 Simulated Control Data Sets 21

2.5.2 Test for Determinism 21

2.5.3 False Nearest Neighbor Test 23

2.5.4 Stimulus Near the Resonance Frequency 24

2.5.5 Stimulus Above the Resonance Frequency 26

2.5.6 Transition to Chaos in the Theoretical Model 26

2.5.7 Poincaré Maps and Stochastic Processes 26

3 Chaos and Signal Detection by Individual Hair Cells 32

3.1 Introduction 32

3.2 Numerical Model 33

3.3 Theoretical Results 35

3.4 Experimental Results 39

3.5 Discussion 45

3.6 Methods 46

3.6.1 Analytic Approximation of the Lyapunov Exponent 46

3.6.2 Transfer Entropy 49

3.6.3 Biological Preparation 50

3.6.4 Mechanical Stimulus 50

3.6.5 Data Collection 50

3.6.6 Stimulus Waveforms 51

3.6.7 Data Analysis 51

3.7 Appendix 52

4 Nonisochronicity, Sensitivity, and Temporal Resolution 57

4.1 Introduction 57

4.2 Theoretical Model 58

4.3 Response to a Constant-Force Stimulus 60

4.3.1 Response Amplitude 61

4.3.2 Temporal Resolution 63

4.3.3 Non-monotonic response 64

4.4 Response to a Short-Pulse Stimulus 65

4.5 Effects of a Spike Train 67

4.6 Discussion 69

4.7 Appendix 71

4.7.1 SNIC Bifurcation 71

4.7.2 Response Time 72

4.7.3 Parameter Conditions for the Twitch 72

5 Synchronization in Coupled Hair-Cell Networks 74

5.1 Introduction 74

5.2 Numerical Model of Coupled Hair Bundle Dynamics 75

5.3 Methods 76

5.3.1 Biological Preparation 76

5.3.2 Artificial Membranes 76

5.3.3 Data Collection 77

5.3.4 Cross-Correlation Coefficient 77

5.3.5 Correlation Time 78

5.4 Theoretical Results 78

5.5 Experimental Results 83

5.6 Discussion 86

5.7 Appendix 88

5.7.1 Approximation of Artificial Membrane Drag 88

5.7.2 Cross-Correlation Coefficient Noise Floor 89

5.7.3 Amplitude and Coherence of Synchronized Hair Bundles 90

6 Chimera States and Frequency Clustering in Coupled Hair-Cell Networks 91

6.1 Introduction 91

6.2 Chimera and Cluster states *in vitro* 92

6.3 Numerical Model of coupled hair cells 97

6.4 Chimera and Cluster States in the numerical simulations of hair cell dynamics . . . 98

6.5 Optimization of Signal Detection 100

6.6 Discussion 103

References 105

LIST OF FIGURES

2.1 (**a**) Position of a driven hair bundle (top) and spontaneously oscillating hair bundle (bottom). The positive direction corresponds to the direction of channel opening. Red and black traces correspond to the stimulus waveform and the hair bundle response, respectively. The small red dots depict how the time intervals are calculated for the Poincaré maps. The schematic image of a hair cell (left) describes the bundle of stereovilli protruding from the cell body. The large red dot depicts the location of probe attachment to the hair bundle. (**b**) Reconstructed attractor of the hair cell system without stimulus, using delayed coordinates ($\tau = 20$ ms). 6

2.2 (**a**) Average angle between neighboring flow vectors as the embedding dimension is varied. The angles are calculated for a 1 minute recording of a typical spontaneously oscillating hair bundle, obtained at 1 kHz sample rate, resulting in 6×10^4 data points. Data were filtered with a low-pass filter to remove high-frequency, stochastic processes. The cutoff frequency was set to 100 Hz, sufficiently above the dominate frequency of the hair bundle ($\sim$20 Hz). To maintain a densely-filled phase space, data were not sub-sampled upon filtering. (**b**) Slopes of the extracted linear region vs. embedding dimension for estimation of the correlation dimension. All data sets plotted are of length $N = 1.8 \times 10^5$, unless otherwise specified. "$\bullet$" and "$\circ$" represent raw hair bundle data without stimulus and corresponding phase-shuffled surrogate data, respectively. "$\blacktriangle$" represents raw hair bundle data during the torus breakdown, at stimulus amplitude of $\sim$10 pN ($N = 2.9 \times 10^4$). "$\star$" and "$\Box$" represent results obtained from a numerical simulation of a limit cycle with and without 10% additive noise, respectively. "$\diamond$" represents a numerical simulation of telegraphic noise. The inset displays the linear regime, in a log-log plot, of the correlation sum vs. hypersphere radius, averaged over 100 reference vectors for embedding dimensions 2 (left) to 10 (right), computed for the raw hair bundle oscillation data. 7

2.3 (**a**) Poincaré maps representing oscillations of hair bundles driven by a sinusoidal stimulus below the resonance frequency ($\omega \sim \frac{2}{3}\omega_0$). Blue lines connect consecutive points in the series. The uncertainty associated with interval measurements is approximately 15 ms (standard deviation). (**b**) Angles formed by vectors from the center of the ring to each point in the Poincaré map (inset). "▲" and "●" represent data obtained for stimulus amplitudes of 9 pN and 12 pN, respectively. 11

2.4 (**a**) Complexity-entropy diagram for the spontaneously oscillating hair bundle in Figure (2.2). For all data sets, “■" and “▲" represent fully sampled and sub-sampled data sets, respectively. Blue and teal colors represent raw hair bundle oscillation data and phase-shuffled surrogate data, respectively. Red represents the time series of a numerical simulation of the normal form equation for the supercritical Hopf bifurcations, driven by noise. Orange represents the corresponding phase-shuffled surrogate data set of this Hopf oscillator. Dark green and light green represent telegraphic noise and the corresponding surrogate data, respectively. “●" corresponds to fractional Brownian motion with Hurst exponent ranging from 0.02 to 0.98. The black curves confine all possible probability distributions. The dashed curve is the half-way point between the upper and lower bounds and serves as an approximate boundary between stochastic and chaotic processes. (**b**) The Kolmogorov entropy of an oscillatory hair bundle subject to a sinusoidal drive (“○"), and transfer entropy from stimulus to hair bundle (“●"). As a control (“○"), transfer entropy from hair bundle to stimulus is also plotted as a function of the stimulus amplitude. Vertical dashed lines delineate approximate regions that correspond to Poincaré maps displaying cloud, ring, and point structures, as illustrated by the schematic diagrams above the graph. Noise floors are indicated by horizontal dashed lines. The noise floor on the K-entropy is estimated by tracking the motion of a passive hair bundle driven by a 10 – 25 pN sinusoidal stimulus. The noise floor on the transfer entropy is estimated based on bundle oscillations in the absence of a stimulus. Uncertainties in K-entropy are estimated by taking the standard deviation of the residuals from the linear fit of Shannon entropy with time. Uncertainties in transfer entropy are estimated from a bootstrapping technique that incorporates the uncertainties in position measurements. 14

2.5 Scatter plot of the largest Lyapunov exponent (λ) versus the transfer entropy from a stimulus to hair bundle oscillator, obtained from a numerical simulation. The applied stimulus was a square wave with stochastic variations of the period. The mean of these periods was set to $\frac{1}{2\pi\omega_0}$ (on resonance) with a standard deviation that is 30% of its mean. The amplitude was set to $f_A = 0.3$. This numerical value corresponds to forcing amplitude of approximately 1 pN. "●", "●", and "●" correspond to variations in parameters k_{on} (0.3 – 0.6), k_{off} (1.0 – 2.2), and x_0 (0.2 – 0.7), respectively. "●" represents variations in the cubic parameter, A ($10^{-5} - 0.15$), when the system is poised in the limit cycle regime. In this regime, the Lyapunov exponent of largest magnitude is calculated analytically. As any parameter is varied, all others are held constant ($x_0 = 0.4$, $k_{on} = \frac{5}{12}$, $k_{off} = \frac{7\pi}{12\arccos(0.4)}$, and $A = 10$.) Error bars in transfer entropy are the standard deviation from repeating the calculation on 10 different stimulus forms, each containing $N = 10^5$ data points. Open circles of all colors correspond to calculations of transfer entropy in the reverse direct (bundle to stimulus) and serve as controls. 18

2.6 Data sets used as controls. Telegraphic noise (top), suprcritical Hopf system (middle), and sine wave with added noise (bottom). 22

2.7 Direct test for determinism on a spontaneously oscillating hair bundle. Red and blue points represent the raw data and phase-shuffled surrogate data, respectively ($N = 1.8 \times 10^5$ data points). Black points represent a sine wave with additive white noise (signal-to-noise ratio = 5). Grey points represent telegraphic noise. Points and error bars represent the mean and standard deviation across all occupied hypercubes in the phase space. 23

2.8 False nearest neighbor test performed on a spontaneously oscillating hair bundle recording with $N = 1.8 \times 10^5$ data points. 24

2.9 Poincaré maps representing spontaneous oscillations of hair bundles (left) and hair bundle response to a sinusoidal stimulus of $\sim$5 pN applied near the resonance frequency (right). 25

2.10 The Kolmogorov entropy of an oscillatory hair bundle subject to a sinusoidal drive (red), transfer entropy from the stimulus to the bundle (black-filled), and transfer entropy from bundle to stimulus (black-open) plotted as a function of the stimulus amplitude. Noise floors are indicated by horizontal dashed lines. Stimulus frequency was selected to be near the resonance frequency of the hair bundle. 25

2.11 Poincaré maps representing oscillations of hair bundles driven by a sinusoidal stimulus above the resonance frequency ($\omega \sim \frac{5}{3}\omega_0$). The four clusters of points indicate a flicker between 1:1 and 1:2 mode-locking. Blue lines connect consecutive points in the series. 27

2.12 The Kolmogorov entropy of an oscillatory hair bundle subject to a sinusoidal drive (red), transfer entropy from the stimulus to the bundle (black-filled), and transfer entropy from bundel to stimulus (black-open) plotted as a function of the stimulus amplitude. Noise floors are indicated by horizontal dashed lines. Stimulus frequency was above the resonance frequency of the hair bundle ($\omega \sim \frac{5}{3}\omega_0$). 28

2.13 (Model) Poincaré maps representing oscillations of hair bundles driven by a sinusoidal stimulus below the resonance frequency ($\omega \sim \frac{2}{3}\omega_0$), for a range of forcing amplitudes, as indicated in the top right corners. Blue lines connect consecutive points in the series. $x_0 = 0.4$, $k_{on} = \frac{5}{12}$, $k_{off} = \frac{7\pi}{12\arccos(0.4)}$,$A = 10$, and $\alpha = 0.15$. 29

2.14 Poincaré map representing telegraphic noise generated by simulating a particle in a quartic potential driven by white noise and sinusoidal forcing. 30

2.15 (**a**) Poincaré map representing a simulation of the supercritical Hopf system driven by white noise and sinusoidal forcing below the resonance frequency ($\omega \sim \frac{2}{3}\omega_0$). (**b**) Corresponding Circle Map. 31

3.1 (**a**) The divergence of two neighboring solutions to Eq. (3.1). The two time-dependent solutions are depicted with black (solid) and red (dashed) lines. (**b**) The natural logarithm of the average separation of neighboring trajectories. Each of the five colors represents an average of 200 pairs of neighboring trajectories, taken with different initial conditions and realizations of common noise. The dashed line represents the linear fit to all of the data within the first 400 time steps. (**c**) The spreading of trajectories throughout the phase space. 10^4 initial conditions were randomly selected in the same neighborhood (red points). After 500 time steps, these solutions spread across the phase space to reveal the fractal structure of the attractor (black points). Side panels show zoomed-in sections corresponding to the colored squares in the main figure. . . . 35

3.2 (**a-b**) Time-domain responses to (off-resonance) sinusoidal and step stimulus, respectively. The top, black traces show the stimulus waveform. Bottom, middle, and top blue traces represent responses of a system with no chaos, weak chaos, and strong chaos, respectively. The degree of chaos was modulated by varying β and ω_0, while keeping the natural frequency fixed at $\Omega_0 = 1$. (**c-e**) Power spectral density of the response to on-resonance sinusoidal stimulus ($\omega_{stim} = \Omega_0 = 1$, as indicated by the vertical, dashed lines) for systems exhibiting no chaos (c), weak chaos (d), and strong chaos (e). Red and black curves represent the spectral density in the presence and absence of the stimulus, respectively. (**f-h**) Power spectral density of the response to off-resonance sinusoidal stimulus ($\omega_{stim} = \frac{1+\sqrt{5}}{2}\Omega_0$, as indicated by the vertical, dashed lines) for systems exhibiting no chaos (f), weak chaos (g), and strong chaos (h). The stimulus frequency was set to the golden ratio with respect to the natural frequency to avoid mode locking. Red and black curves represent the spectral density in the presence and absence of the stimulus, respectively. 37

3.3 (**a**) Phase-locked amplitude gain for on-resonance, sinusoidal stimulus. (**b**) Transfer entropy from burst noise stimulus to response of the Hopf oscillator. For (a-b), β, ω_0, and D, were varied, resulting in a range of Lyapunov exponents. All other parameters were fixed ($\mu = \alpha = \Omega_0 = 1$). Color was generated by linearly interpolating a grid of 21 Lyapunov exponent values and 29 noise strengths. The stimulus amplitude was set to 0.5 for both panels. The vertical dashed lines indicate the points where the signal-to-noise ratio is 1, as defined by the ratio of the signal power to the noise power. (**c**) Phase-locked amplitude gain for on-resonance, sinusoidal stimulus. (**b**) Transfer entropy from burst noise stimulus to response of the Hopf oscillator. (**c**) Mean displacement in response to a step stimulus. (**d**) Response time to the step stimulus, calculated by taking the decay time of an exponential fit to the mean response. For (c-f), the Kolmogorov entropy was modulated by varying β and ω_0. All other parameters were fixed ($\mu = \alpha = \Omega_0 = 1, D = 0.05$). 38

3.4 (**a**) Spontaneous oscillations of a hair bundle under various calcium concentrations of the endolymph. From bottom to top: 100 μM (low calcium), 250 μM (natural calcium), and 325 μM (high calcium). (**b**) Spontaneous oscillations of a hair bundle with various endolymph viscosities. From bottom to top: 0, 70, and 100 $\frac{mg}{ml}$ of Dextran 500. (**c**) Power spectral density of the traces in (a). (**d**) Power spectral density of the traces in (b). 40

3.5 (**a**-**c**) Poincaré maps constructed from the time intervals between the steepest rising flanks of consecutive hair bundle oscillations under low ($175\mu M$), natural ($250\mu M$), and high ($325\mu M$) calcium concentrations of the endolymph, during presentation of off-resonance stimulus. (**d**) Circle map corresponding to the low-calcium conditions. The monotonic function suggests the absence of chaos. (**e**-**f**) Circle maps corresponding to the natural- and high-calcium conditions, respectively. The absence of a monotonic function indicates the presence of chaos. We use Spearman's rank correlation coefficient to test for monotonicity of the circle maps. Under low-, natural-, and high-calcium conditions, Spearman's coefficient is 0.60 ± 0.01, 0.14 ± 0.01, and 0.30 ± 0.02, respectively. Uncertainties represent 1 standard deviation from a sample of 100 bootstraps. 42

3.6 (**a**) Phase-locked amplitude gain for 2 pN sinusoidal stimulus, presented at the natural frequency. Data points and error bars on this measure represent the mean and standard deviation from 100 bootstraps. The noise floor (dashed curve) was calculated by treating a segment of the spontaneous oscillation recording as if a stimulus were present and calculating the gain. This curve represents the mean plus one standard deviation from 100 bootstraps. (**b**) Transfer entropy from burst noise stimulus to hair bundle response. Data points and error bars represent the mean and standard deviation obtained from 100 bootstraps. The noise floor (dashed curve) was determined by calculating the transfer entropy in the reverse direction (response to stimulus). This curve represents the mean plus one standard deviation from 100 bootstraps. (**c**) Average displacement induced on the hair bundle from the step stimulus, averaged over ~ 200 square waves. Data points and error bars represent the mean and standard deviation of the response plateau. Orange-open and purple-filled data points represent averages over steps in the positive (channel open) and negative (channel closed) directions, respectively. The noise floor is represented by the dashed line. (**d**) Response time to step stimulus, characterized by fitting the mean response to an exponential and extracting the decay time. Error bars represent the standard deviation of the residual associated with the exponential fit. All measurements were performed on the same cell. 44

3.7 Comparison of the analytic calculation of the Lyapunov exponent (red line) to the numerical calculation (black points). (**a**) The noise strength is varied, while all other parameters are fixed ($\mu = \alpha = \Omega_0 = 1,\ \beta = 50$). (**b**) β is varied, while all other parameters are fixed ($\mu = \alpha = \Omega_0 = 1, D = 0.05$) 52

3.8 Phase-locked amplitude gain for above-resonance ($\omega_{stim} = 1.05\Omega_0$), sinusoidal stimulus as the noise strength and Lyapunov exponent are varied. Color was generated by linearly interpolating a grid of 10 Lyapunov exponent values and 10 noise strengths. . . 53

3.9 (**a**) Phase-locked amplitude gain for on-resonance, sinusoidal stimulus as the noise strength and Lyapunov exponent are varied. Color was generated by linearly interpolating a grid of 10 Lyapunov exponent values and 10 noise strengths. (**b**) Transfer entropy from burst noise stimulus to response of the Hopf oscillator as noise strength and Lyapunov exponent are varied. In the $\lambda < 0$ regime, the system is quiescent, and the Lyapunov exponent characterizes the stability of this fixed point. Color was generated by linearly interpolating a grid of 10 Lyapunov exponent values and 10 noise strengths. For both panels, the Lyapunov exponent was modulated by varying μ. . . . 53

3.10 The dependence of Kolmogorov entropy on the endolymph calcium concentration. Each of the six colors corresponds to a different cell. 54

3.11 Phase-locked amplitude gain for 2 pN sinusoidal stimulus at the natural frequency (**a-c**) and above the natural frequency (**d-f**) for three additional cells. Data points and error bars on the gain represent the mean and standard deviation from 100 bootstraps. The noise floor (dashed curve) was calculated by treating a segment of the spontaneous oscillation recording as if a stimulus were present and calculating the gain. This curve represents the mean plus one standard deviation from 100 bootstraps. (**g-i**) Transfer entropy from burst noise stimulus to response. Data points and error bars represent the mean and standard deviation obtained from 100 bootstraps. The noise floor (dashed curve) was determined by calculating the transfer entropy in the reverse direction (response to stimulus). This curve represents the mean plus one standard deviation from 100 bootstraps. 55

3.12 (**a-c**) Average displacement induced on the hair bundle from the step stimulus, averaged over ~ 200 square waves. Data points and error bars represent the mean and standard deviation of the response plateau. (**d-f**) Response time to step stimulus, characterized by fitting the mean response to an exponential and taking the decay time. Error bars represent the standard deviation of the residual associated with the exponential fit. (**g-i**) Response times from (d-f) scaled to the natural periods of oscillation for each recording. For all panels, open-dashed and closed-solid data points represent averages over steps in the positive (channel open) and negative (channel closed) directions, respectively. 56

4.1 (a) The fractal structure of the Hopf oscillator with common noise: 10^4 slightly different initial conditions (confined to the grey circle) were evolved by 500 time steps under the same realizations of stochastic forces to produce the black points. (b) A zoomed-in version of the region in the grey box. $\mu = \alpha = \Omega_0 = 1$, $\beta = 100$, $D = 0.05$, where D is the noise strength and $\Omega_0 = \omega_0 - \frac{\beta\mu}{\alpha}$ is the natural frequency. 58

4.2 (a) Mean displacement of the Hopf oscillator in response to a constant-force stimulus found semi-analytically (black points) and fully analytically (solid curve). (b) Response time of the oscillator characterized by the exponential decay time in response to a step force. Black points represent the values found from numerical simulations, and the solid curve represents the analytic approximation. For (a-b), $\mu = \alpha = \Omega_0 = 1$ and $f_0 = 0.01$. The dashed line indicates the point where the forcing is able to induce a SNIC bifurcation. (c) An example of the twitch, a non-monotonic response (solid) to a step force (dashed), for $\mu = \alpha = \Omega_0 = 1$, $\beta = 50$, and $f_0 = 0.1$. The response curve represents the average over 200 different initial conditions, evenly separated in phase. . 62

4.3 Mean displacement of the Hopf oscillator in response to a brief, constant-force stimulus. (a) and (b) represent the responses to a pulse of duration $\frac{1}{4}$ and $\frac{1}{16}$ of the natural period of oscillation, respectively. $\mu = \alpha = \Omega_0 = 1$, $f_0 = 0.01$, and the vertical dashed line represents the value of β at which the forcing is able to induce a SNIC bifurcation. 66

4.4 Bifurcation diagrams generated from the radial stroboscopic map at each impulse of the spike train. The interval between spikes was set to be the natural period of oscillations ($\tau = \frac{2\pi}{\Omega_0}$, $\mu = \alpha = \Omega_0 = 1$). (a) $\beta = 3$, while f_0 is varied. (b) $f_0 = 0.1$, while β is varied. 67

4.5 Illustration of the SNIC bifurcation. The solid and dashed curves represent the stable limit cycle and angular nullcline, respectively. Filled and empty points represent attracting and repelling fixed points, respectively. (a) Phase space diagram with no forcing. (b) A constant force in the $\hat{x}$ direction pushes the limit cycle into the angular nullcline, producing a semi-stable fixed point. (c) Upon increasing the force, the semi-stable fixed point splits into an attracting and a repelling fixed point. (d) Stronger forcing causes these two points to separate further. 71

5.1 (**a**) Time traces of five coupled isochronous oscillators (bottom) and five coupled nonisochronous oscillators with β_j linearly spaced from 0 to 6 (top). (**b**) Average cross-correlation coefficient (Eq. 5.4) between all pairs of oscillators as a function of the frequency dispersion. This system consists of five oscillators in the isochronous (black-open) and nonisochronous (green-filled) cases. (**c-e**) Illustrations of the instantaneous frequencies (Eq. 5.7) of four oscillators as a function of the oscillation amplitude for the isochronous, nonisochronous with identical β_j, and nonisochronous with dispersion in β_j systems, respectively. 79

5.2 (**a-b**) Time traces of coupled oscillators for the isochronous and nonisochronous ($\beta_{max} = 6$) systems, respectively. The bottom, middle, and top sets of traces correspond to system sizes of $N = 1$, 3, and 10, respectively. (**c**) Root mean square (RMS) amplitude of the autonomous oscillations for a range of system sizes for the isochronous (black-open) and nonisochronous (orange-filled) cases. (**d**) Normalized correlation time (Eq. 5.6) for the isochronous (black-open) and nonisochronous (purple-filled) systems. . . . 80

5.3 (**a**) Average response of the system to weak sinusoidal stimulus, illustrated by the black curves. The stimulus frequency was set to the median limit-cycle frequency of the network, $F(t) = 0.05\sin(\Omega_{\frac{N+1}{2}}t)$. The responses (blue, red, and orange curves) represent the average over all oscillators, over 20 presentations of the stimulus, each with random initial conditions. Bottom, middle, and top traces correspond to $\beta_{max} =$ 0, 2, and 6, respectively. (**b**) Spectral curves in response to low-level white-noise stimulus. The curves get increasingly narrow for increasing β_{max}. (**c**) Average oscillator response to a step stimulus, as indicated by the black-dashed curve. Middle, top, and bottom plateau curves correspond to $\beta_{max} =$ 0, 2, and 6, respectively. For (a-c), the system size was $N = 10$, and the blue, red, and orange curves represent $\beta_{max} =$ 0, 2, and 6, respectively. (**d**) Spectral value of the nonisochronous ($\beta_{max} = 6$) system at the resonance frequency in response to weak white-noise stimulus, scaled to the corresponding spectral response of the isochronous system. (**e**) Quality factor of the system with $\beta_{max} = 6$ in response to weak white-noise stimulus, scaled to the quality factor of the isochronous system. (**f**) Response time of the nonisochronous ($\beta_{max} = 6$) system to a step stimulus, scaled to the response time of the isochronous system. Points and error bars represent the mean and the standard deviation over 100 presentations of the stimulus, each with random initial conditions. 81

5.4 (**a**) Illustration of the experimental system from a side view, displaying the hair cells (HC), hair bundles (HB), and an artificial membrane. (**b-c**) Top-down images of biological preparations. The hair bundles appear as white dots, and the shadow cast by the transparent artificial membrane can be seen in the center of the images. (**d-e**) Time traces and power spectra of 3 spontaneously oscillating hair bundles coupled by an artificial membrane. These bundles are circled in (b) with colors corresponding to their time traces. The top, middle, and bottom traces correspond to the topmost, leftmost, and bottommost circles in (b). (**f-g**) Time traces and power spectra of the 3 hair bundles in (d-e) after removal of the artificial membrane. 84

5.5 (**a-b**) Overlaid traces of coupled hair bundles (top) for system sizes of $N = 4$ and $N = 6$, respectively. Below the overlaid traces are the traces of the individual hair bundles obtained in the absence of coupling. (**c-d**) RMS amplitude and the normalized correlation time of spontaneous oscillations of coupled hair bundles, obtained for various system sizes. Each hair bundle had a cross-correlation coefficient of at least 0.1 with other bundles in the network. For both panels, points and error bars represent, respectively, the mean and the standard deviation of the coupled oscillators in the system. For systems with $N > 1$, each data point represents a separate group of coupled hair bundles. The points and error bars at $N = 1$ represent the collective mean and standard deviation across all 10 groups of hair bundles in the absence of coupling. These 10 groups of hair bundles were obtained from four sacculi from four different frogs. 85

5.6 Histogram of the cross-correlation coefficients between pairs of uncoupled, spontaneously oscillating hair bundles (1225 unique pairs). The standard deviation of this distribution is < 0.02 and no points exceed 0.1. 89

5.7 (**a-b**) RMS amplitude and normalized correlation time of spontaneous oscillations of coupled hair bundles, obtained for various system sizes. Each hair bundle had a cross-correlation coefficient of at least 0.5 with other bundles in the network in order to ensure the network is synchronized. For both panels, points and error bars represent, respectively, the mean and the standard deviation of the coupled oscillators in the system. For systems with $N > 1$, each data point represents a separate group of coupled hair bundles. The points and error bars at $N = 1$ represent the collective mean and standard deviation across all 10 groups of hair bundles in the absence of coupling. . . . 90

6.1 (a) Illustration of the experimental system from a side view, displaying the hair cells (HC), hair bundles (HB), and an artificial membrane. (b) Time traces of three spontaneously oscillating hair bundles coupled by an artificial membrane. (c) Top-down images of a biological preparation. The hair bundles appear as white ovals, and the shadow cast by the transparent artificial membrane can be seen in the center of the image. (d) Time traces of the three hair bundles in (b) after removal of the artificial membrane. 93

6.2 (a) Space-time plot of 17 spontaneously oscillating hair bundles coupled with an artificial membrane, exhibiting a chimera state. Oscillators 1-7 are synchronized while the others oscillate incoherently. (b) Power spectra of the 17 coupled oscillators. The 7 synchronized hair bundles are plotting with thick, green curves. (c) Correlation matrix of the coupled hair bundles. The synchronized oscillators are highlighted in the green box. 95

6.3 (a) Time traces of four spontaneously oscillating hair bundles coupled with an artificial membrane, exhibiting frequency clustering. Orange (top two) and green (bottom two) traces correspond to the high and low frequency clusters, respectively. (b) Power spectra of the four coupled oscillators, plotting in colors corresponding to the traces in (a). (c) Correlation matrix of the coupled hair bundles. The synchronized oscillators are highlighted in colors corresponding to the colors of their traces. 96

6.4 (a) Space-time plot of the numerical model exhibiting a chimera state. Oscillators 1-6 synchronize while the others oscillate incoherently. (b) Power spectra of the 10 oscillators, with the synchronized ones plotted with thick, green curves. (c) Correlation matrix of the system. The synchronized oscillators are highlighted in the green box. For all panels, the k_j values were selected from a uniform distribution spanning 0.2–3.0. The simulations were carried out with time steps of $dt = 0.001$, $\beta_j = 0$, and no noise or external forcing. 99

6.5 (a) Space-time plot of the numerical model exhibiting frequency clustering. (b) Power spectra of the 10 oscillators, with five oscillators in each of the two clusters, as indicated by the solid-green (low frequency) and dotted-orange (high frequency) curves. (c) Correlation matrix of the system. The two clusters are highlighted with colors corresponding to that of their spectral density curves. Simulations were performed with no noise or external forcing, and with time steps of $dt = 0.001$. The coupling strengths were all equal, $k_j = k = 1.5$, and the β_j values were selected from uniform distributions spanning -1–0 for the first five oscillators and 0–1 for the last five oscillators. 100

6.6 (a-h) Sensitivity maps of the numerical model in response to a sinusoidal stimulus with amplitude $f_0 = 0.2$ and noise strength $D = 0.01$ for coupling strengths $k_j = k = 0$, 0.75, 1, 1.25, 1.5, 2, 3, and 5, respectively. (i) Synchronization index as a function of the coupling strength, showing the transition to coherence. (j) Trade-off between the oscillator-average vector strength at the most sensitive stimulus frequency (purple circles) and the fraction of stimulus frequencies for which an oscillator responds with a vector strength of at least 0.2 (green squares). (k) Vector strength averaged across all oscillators and all stimulus frequencies. For (i) and (k), blue circles, orange squares, and red triangles represent system sizes of 10, 100, and 1000 coupled oscillators, respectively. 101

ACKNOWLEDGMENTS

I will forever be grateful to have worked alongside Dolores Bozovic, my research mentor and committee chair. Dolores taught me how to think like a scientist and approach each problem with curiosity, skepticism, and enthusiasm. Only with her help was I able to succeed in both theoretical and experimental research. I could not have asked for a more reasonable and supportive mentor.

I owe many thanks to our former research associates, Sebastiaan Meenderink and Yuki Quinones for teaching me to be a careful and precise experimentalist and for always pushing me to understand more. I also owe a debt of gratitude to Elizabeth Mills, who introduced me to the lab and taught me how to perform dissections, among many other things.

I am grateful to have worked alongside many other bright scientists such as Seung Ji, Tracy Zhang, Janaki Sheth, Jessica Lin, Joey Marcinik, Nick Senofsky, Samuel Li, and Martin Toderi. These people gave life to the lab and always helped me to think critically.

I express appreciation to my committee for taking the time review this manuscript and its defense. I am also grateful for our helpful discussions on data analysis, nonlinear dynamics, and sensory systems.

I extend my deepest gratitude to our collaborators and friends, Yuttana Roongthumskul and Yuval Edri. Working with them has helped me to grow as a scientist and an individual.

Lastly, I want to extend a warm thank you to my friends Yeou Chiou, Judy Saunders, and many others for providing endless support and making this journey worth perusing.

VITA

2009–2011	A.S., Morraine Valley Community College.
2011–2013	B.S. in Engineering Physics, University of Illinois, Urbana-Champaign.
2014–2017	Teaching Assistant, Physics, University of California, Los Angeles (UCLA).
2015–present	Graduate Student Researcher, Physics, UCLA.

PUBLICATIONS

Faber, J. and Bozovic, D. “Chaotic dynamics of inner ear hair cells”. *Scientific Reports* **8**, 3366 (2018).

Faber, J. and Bozovic, D. “Noise-induced chaos and signal detection by the nonisochronous Hopf oscillator”. *Chaos* **29**, 043132 (2019).

Faber, J. and Bozovic, D. “Chaotic dynamics enhance the sensitivity of inner ear hair cells”. *Scientific Reports* **9**, 18394 (2019).

Roongthumskul, Y., Faber, J., and Bozovic, D. “Dynamics of mechanically coupled hair-cell bundles of the inner ear”. *Biophysical Journal* **120**, 205 (2021).

Faber, J., Li, H., and Bozovic, D. “Synchronization and chaos in systems of coupled inner-ear hair cells”. *Physical Review Research* **3**, 013266 (2021).

Faber, J. and Bozovic, D. “Chimera states and frequency clustering in systems of coupled inner-ear hair cells”. arXiv:2105.04412 (2021).

CHAPTER 1

Introduction

The auditory and vestibular systems are extraordinary signal detectors. These end organs can reliably detect sound and mechanical vibrations that induce displacements as small as a few angstroms, comparable to or below the amplitude of motion caused by thermal fluctuations in the surrounding fluid [1]. These sensory systems also exhibit remarkable temporal resolution, frequency selectivity, and dynamic range of detection. Humans are able to resolve two stimulus impulses that are temporally separated by only 10 microseconds, where the stimulus waveform is presented simultaneously into both ears [2]. How these biological sensors achieve their signal detection properties is a long-standing open question, and the physics of hearing remains an active area of research [3].

Mechanical detection of sound waves, vibrations, and accelerations is performed by hair cells. These specialized cells are named after the rod-like stereovilli that protrude from their apical surfaces. The cluster of inter-connected stereovilli is named the hair bundle and performs the essential task of transducing the mechanical energy of sound into electrical signals that take the form of ionic currents into the cell [4, 5, 6]. A perturbation caused by sound or acceleration results in a deflection of the hair bundles and an increase in the tension of the tip links that connect adjacent rows of stereovilli. A change in tension of the tip links modulates the open probability of the transduction channels that are embedded at the tops of the stereovilli and connected to the tip links.

Auditory detection has been shown to require an active, energy-consuming process in order to achieve such remarkable signal detection [7]. This active process manifests itself in a number of phenomena, including the appearance of autonomous motion of the hair bundles, observed *in vitro* in several species [8, 9, 10]. These spontaneous oscillation have amplitudes well above the noise induced by thermal fluctuations, and they have been shown to be active, as they violate the fluctuation dissipation theorem [11]. The role of these spontaneous oscillations is not yet fully understood, but prior studies have suggested that they could be utilized as an amplification mechanism for weak signals [12]. These spontaneous oscillations also serve as a probe for studying the active cellular mechanics underlying auditory detection.

Another manifestation of this active process is the spontaneous emission of sound, observed *in vivo* in many species [13]. These spontaneous otoacoustic emissions (SOAEs) exhibit several sharp peaks in their power spectra and are metabolically sensitive, indicating an underlying energy-consuming process. Although SOAEs serve as a diagnostic for hearing-related disorders in humans, there is currently no consensus on the mechanism responsible for generating them [14, 15, 16]. One theory suggests that they arise from frequency clustering of actively oscillating coupled hair cells [17, 18].

In vivo, hair bundles are attached to overlying structures, which provide coupling between the individual active oscillators. The strength and extent of the coupling varies across species and organs [6]. In the bullfrog sacculus, several thousand hair cells are coupled together by the otolithic membrane. The sacculus is responsible for detecting low-frequency ground-borne and airborne vibrations. In contrast to auditory organs, the sacculus does not display a high degree of frequency selectivity, nor any tonotopic organization of the hair cells: there is no correlation between the characteristic frequencies of the hair cells and their location in the sensory epithelium [19]. It does, however, demonstrate extreme sensitivity of detection [20].

Dynamics of the auditory response have been modeled using the normal form equation for Hopf bifurcations [21, 22]. This simple differential equation accounts for many experimentally observed phenomena, including the sensitivity and frequency selectivity of hearing exhibited by many species. To reproduce the empirically measured sensitivity, the models have assumed that the system is poised in close proximity to the Hopf bifurcation. This assumption raises the question of how the biological system achieves and then maintains such fine-tuning of the parameters. To circumvent this issue, some models include a dynamic feedback equation responsible for automatically tuning the control parameter towards or away from criticality [23, 24]. Other studies proposed that the inclusion of a homeostatic equation can broaden the parameter regime of extreme sensitivity, frequency selectivity, and compressive nonlinearity [25]. A second issue with proximity to criticality is the phenomenon of critical slowing down: near the bifurcation, a system would exhibit a slow response, which seems inconsistent with the high temporal resolution that characterizes hearing. This second objection is not resolved by the inclusion of homeostasis or feedback. We therefore propose that the system is poised in the oscillatory state, not in the immediate vicinity of the Hopf bifurcation. We focus our theoretical and experimental studies on that regime, as it is consistent with the occurrence of SOAEs.

In chapter 2, we use a number of tests from dynamical systems theory to demonstrate experimentally that spontaneous hair-bundle oscillations exhibit chaotic dynamics. Chaotic dynamics are typically considered a harmful element to dynamical systems as they limit predictability. Chaos can also be harmful in biological systmes. For example, a chaotic heartbeat is an indicator of cardiac fibrillation [26, 27]. However, in chapter 3, we demonstrate, using experimental recordings and numerical simulations, that hair cells are most sensitive to external signals when poised in the weakly chaotic regime. Further, we demonstrate that the temporal resolution of these detectors increases with increasing levels of chaos. In chapter 4, we explore the numerical model analytically and identify the mechanisms that cause this system to exhibit a chaotic response and enhanced signal detection. These mechanisms result from nonisochronous dynamics, those with amplitude-dependent frequency. Nonisochronicity has been excluded from most prior theoretical studies. However, we find it to be essential for reproducing our experimental data. Together, chapters 2–4 demonstrate that the instabilities that give rise to chaos in hair-cell dynamics result in enhanced sensitivity and temporal resolution.

In chapter 5, we explore the dynamics of oscillatory hair cells coupled with artificial membranes. Our experimental recordings and numerical simulations of this system suggest that the chaotic dynamics of the individual hair cells result in enhanced synchronization of the entire system. We further show that this enhanced synchronization greatly improves the ability of the system to detect weak signals. Both the sensitivity and frequency selectivity grow with increasing number of oscillators in the network. Lastly, we show in chapter 6 that these systems of hair bundles coupled with artificial membranes can also exhibit partial synchronization. We identify chimera states, where some of the oscillators synchronize while others oscillate incoherently. We also identify frequency clustering, where the oscillators synchronize with one of several clusters, which oscillate at different frequencies. The existence of the frequency clustering state supports the theory that SOAEs are generated from spontaneous hair cell activity. Our numerical model reproduces both forms of partial synchronization upon introducing heterogeneity in the model parameters. Finally, we show that these states of partial synchronization could be helpful for signal detection in cases where the array of oscillators is responsible for detecting a wide range of stimulus frequencies.

CHAPTER 2

Chaotic Hair-Cell Dynamics

2.1 Introduction

The presence of chaos may help to explain the extreme sensitivity of hearing, as it has been shown in nonlinear dynamics theory that chaotic systems can be highly sensitive to weak perturbations [28]. In this chapter, we therefore explore experimentally whether innate bundle motility exhibits signatures of chaos [29]. Since establishing the dimensionality of the system is crucial for accurate modeling of this remarkable mechanical detector, we apply a dimensionality test to estimate the number of state variables required to describe the dynamics of an auditory hair cell. Further, we examine the effect of an applied signal on the chaoticity of bundle motion. For this purpose, we construct Poincaré maps of the oscillator, subject to varying amplitudes of external forcing, and test for signatures of torus breakdown. We quantify the degree of chaos by computing the Kolmogorov entropy associated with the spontaneous and driven oscillation of a hair bundle. As a measure of the sensitivity to external perturbation, we compute the transfer entropy from the signal to the oscillatory bundle. Finally, we present a simple theoretical model that reproduces the quasiperiodic and chaotic dynamics that were observed experimentally. We use the theoretical model to demonstrate that a system poised in the chaotic regime shows an enhanced sensitivity to weak stimuli.

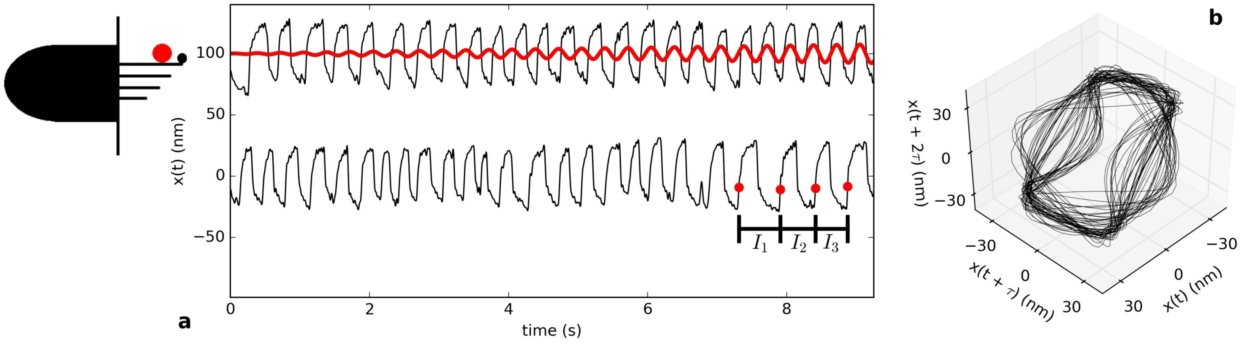

Figure 2.1: (**a**) Position of a driven hair bundle (top) and spontaneously oscillating hair bundle (bottom). The positive direction corresponds to the direction of channel opening. Red and black traces correspond to the stimulus waveform and the hair bundle response, respectively. The small red dots depict how the time intervals are calculated for the Poincaré maps. The schematic image of a hair cell (left) describes the bundle of stereovilli protruding from the cell body. The large red dot depicts the location of probe attachment to the hair bundle. (**b**) Reconstructed attractor of the hair cell system without stimulus, using delayed coordinates ($\tau = 20$ ms).

2.2 Results

2.2.1 Dimensionality Test

A useful technique for estimating the dynamical dimension, d_L, of a time series relies on the reconstruction of the phase space using delayed coordinates. It has been shown that this delayed-coordinate map from the original d_L-dimensional smooth compact manifold M to $\mathbb{R}^{d_E}$ is diffeomorphic, provided that $d_E > 2d_A$, where d_A is the box-counting dimension of the original attractor, and d_E is the embedding dimension [30, 31, 32]. Frequently, a lower embedding dimension is sufficient to fully unfold the attractor, but it is necessary that $d_E \geq d_L$ [33, 34]. In finding the optimal embedding dimension, we set an upper bound on the dynamical dimension of the original dynamics. From the original time series $x(t)$, we construct the vector,

$$\vec{X} = [x(t), x(t+\tau), x(t+2\tau), ..., x(t+(d_E-1)\tau)], \tag{2.1}$$

for each point in the time series; τ is chosen as the time at which the average mutual information of the series exhibits its first minimum [35]. For each point in the reconstructed phase space, we compute the unit vector,

$$\hat{u}(t_n) = \frac{\vec{X}(t_{n+1}) - \vec{X}(t_n)}{||\vec{X}(t_{n+1}) - \vec{X}(t_n)||}, \tag{2.2}$$

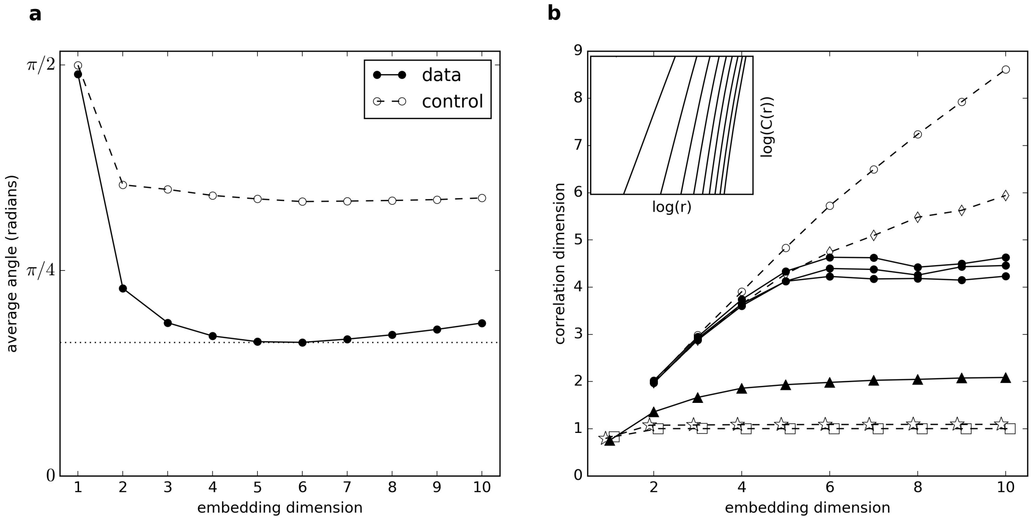

Figure 2.2: (**a**) Average angle between neighboring flow vectors as the embedding dimension is varied. The angles are calculated for a 1 minute recording of a typical spontaneously oscillating hair bundle, obtained at 1 kHz sample rate, resulting in 6×10^4 data points. Data were filtered with a low-pass filter to remove high-frequency, stochastic processes. The cutoff frequency was set to 100 Hz, sufficiently above the dominate frequency of the hair bundle (∼20 Hz). To maintain a densely-filled phase space, data were not sub-sampled upon filtering. (**b**) Slopes of the extracted linear region vs. embedding dimension for estimation of the correlation dimension. All data sets plotted are of length $N = 1.8 \times 10^5$, unless otherwise specified. “•" and “○" represent raw hair bundle data without stimulus and corresponding phase-shuffled surrogate data, respectively. “▲" represents raw hair bundle data during the torus breakdown, at stimulus amplitude of ∼10 pN ($N = 2.9 \times 10^4$). “⋆" and “□" represent results obtained from a numerical simulation of a limit cycle with and without 10% additive noise, respectively. “◇" represents a numerical simulation of telegraphic noise. The inset displays the linear regime, in a log-log plot, of the correlation sum vs. hypersphere radius, averaged over 100 reference vectors for embedding dimensions 2 (left) to 10 (right), computed for the raw hair bundle oscillation data.

where t_n is the time of the n^{th} observation. These unit vectors point in the direction of local flow on the attractor. For deterministic systems, neighboring unit vectors are nearly parallel if the attractor is densely sampled, and if the time series is not dominated by stochastic processes. The flow therefore becomes smooth when the embedding dimension is high enough to fully unfold the attractor. The smoothness of this reconstructed phase space can be quantified by finding the average angle that each unit vector (Eq. 2.2) makes with its nearest neighbor [34, 36]. Starting with one embedding dimension, we calculate the average angle among all unit vectors, then increase the embedding dimension, and repeat the calculation. The average angle either plateaus or reaches a minimum when using the optimal embedding dimension. The latter case arises when stochastic processes continue to perturb the smoothness in higher dimensions, after the deterministic component has been fully unfolded, thus leading to a gradual increase in the average angle.

For a spontaneously oscillating hair bundle (Fig. 2.1), the phase space fully unfolds between three and six dimensions (Fig. 2.2a). As a control, we perform the same analysis on a surrogate data set, generated from the original data as follows. We multiply each Fourier component by a random phase, creating a stochastic signal with the power spectrum and the autocorrelation function identical to those of the original data set. The surrogate data set does not yield a minimum similar to the original data, and the flow along phase space trajectories is much less smooth. We obtained consistent results using an alternate method, referred to in literature as the false nearest neighbor test [37] (see Appendix). Further, we performed a direct test for determinism [36] and found a statistically significant difference between the hair bundle oscillation recordings and their surrogate data sets (see Appendix). These results indicate that, although stochastic processes are present in our system, there is an underlying low-dimensional attractor. Further, up to six differential equations should be sufficient to describe the dynamic behavior of an active hair cell bundle.

2.2.2 Correlation Dimension

The fractal dimension of an attractor reflects the space filling capacity of its trajectories. The correlation dimension provides a similar measure and is frequently used to estimate the fractal dimension of a system that is contaminated by noise [38, 39]. The correlation dimension can never exceed the number of degrees of freedom of the dynamical system, and hence yields a lower bound. To measure the correlation dimension, the phase space is reconstructed using the delayed-coordinate technique (see section on dimensionality test). Hyperspheres are constructed that are centered on each of the phase space points. The correlation sum is defined as

$$C(r) \equiv \lim_{N\to\infty} \frac{1}{N^2} \sum_{i,j=1}^{N} \Theta(r - |\vec{X}_i - \vec{X}_j|), \tag{2.3}$$

where Θ is the Heaviside step function, and $\vec{X}_i$ is the vector from the origin to the location of the i^{th} point in reconstructed phase space. The correlation sum is a function of the hypersphere radius, and for small values of r, should obey the power law,

$$C(r) \propto r^{\nu}, \tag{2.4}$$

where ν is the correlation dimension. To extract ν from the data, we plot $\log(C(r))$ versus $\log(r)$ and find the slope of the linear regime. We repeat this for an increasing number of embedding dimensions, until a plateau occurs in the values of ν. This plateau onset is expected to occur when the embedding dimension exceeds the correlation dimension [40]. This plateau never occurs for a time series dominated by stochastic processes. Integer values of ν imply a non-chaotic attractor while non-integer values of ν are indicative of a chaotic attractor.

In Fig. (2.2b), we observe a plateau in the correlation dimension, which occurs at a value between 4 and 5. A correlation dimension between 4 and 5 is consistent with our previous results, which indicate that hair bundle dynamics contain between 3 and 6 degrees of freedom. Further, the non-integer correlation dimension suggests a chaotic attractor in the hair cell dynamics. We compare these results to two controls. The first is a surrogate data set generated by shuffling the phases of the Fourier components of the raw data. The second is telegraphic noise generated by solving the Langevin equation in a quartic well potential (see Appendix). The plateau in correlation dimension does not occur for either of these stochastic data sets. When a sinusoidal stimulus of approximately 10 pN was applied to the bundle, the correlation dimension showed a plateau near 2, consistent with torus breakdown.

2.2.3 Poincaré Maps

The Poincaré map provides a powerful tool for observing the dynamics of a nonlinear system in a lower dimensional space. For a perfectly periodic signal, the map takes the form of a single point. A quasiperiodic attractor is one whose trajectories densely fill the surface of a torus. The Poincaré map then comprises a ring-like structure which represents a cross section of this torus. The occurrence of trajectories that fall off the surface of this torus indicates a quasiperiodic transition to chaos via torus breakdown [41, 42, 43, 44, 45]. Stochastic and high-dimensional processes yield a cloud-like Poincaré map that has no internal structure. The presence of a chaotic attractor could therefore be obscured by the presence of noise.

Poincaré maps are most commonly constructed by strobing a measured time series at a constant rate [46]. However, this method would not be appropriate for analyzing hair bundle motion, due to the nearly bimodal distribution of bundle positions. As can be seen in Figure (2.1a), a typical oscillation approximates a square wave with a varying local period. Hence, to construct Poincaré maps from our recordings, we follow an alternate approach, developed in [47]. We determine the discrete time series, $[I_n]$, where subsequent elements are the time intervals between the steepest rising flanks of consecutive bundle oscillations. We then plot the n^{th} versus the $(n+1)^{th}$ point of the series to obtain the Poincaré map. As the series constitutes an observable in phase space, embedding theory can be applied [32]. Poincaré maps constructed for the motion of a hair bundle subject to sinusoidal stimuli at varying amplitudes of forcing are shown in Figure (2.3).

At low stimulus amplitudes, and in the absence of stimulus, the Poincaré maps form a cloud-like structure. At higher stimulus amplitudes, a ring structure emerges from the cloud. Consecutive points within the sequence migrate around the edge of the ring, rather than crossing over the center, indicative of a quasiperiodic behavior. The point density of this ring was found to be significantly distinguishable from surrogate data sets generated by randomizing the order of the elements in $[I_n]$. When the stimulus amplitude is increased above approximately 15pN, the hair bundle follows the stimulus, causing the ring structure to collapse onto a point. This quasiperiodic transition was

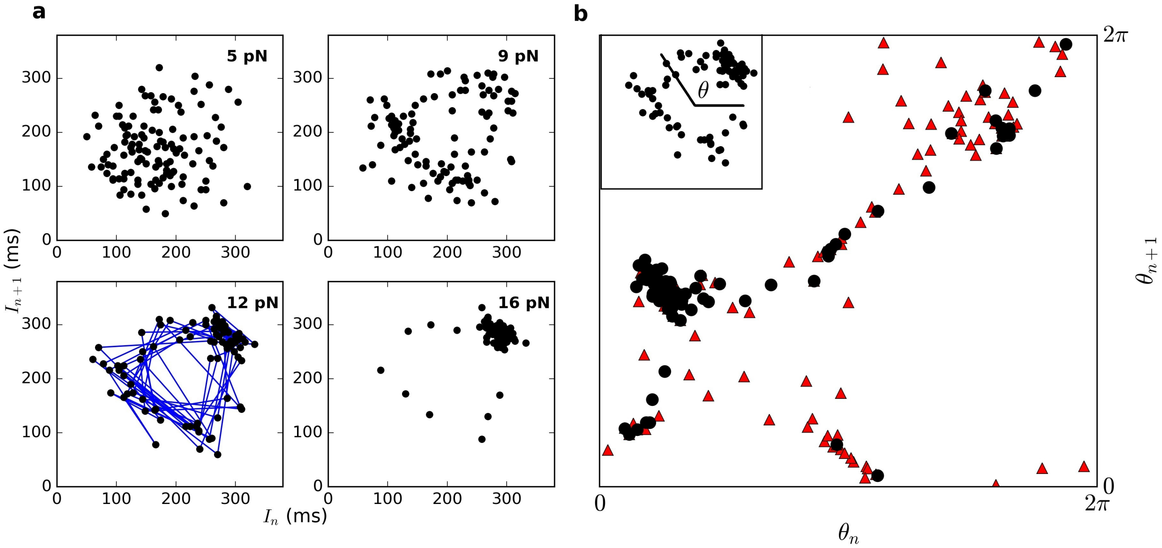

Figure 2.3: (**a**) Poincaré maps representing oscillations of hair bundles driven by a sinusoidal stimulus below the resonance frequency ($\omega \sim \frac{2}{3}\omega_0$). Blue lines connect consecutive points in the series. The uncertainty associated with interval measurements is approximately 15 ms (standard deviation). (**b**) Angles formed by vectors from the center of the ring to each point in the Poincaré map (inset). "▲" and "●" represent data obtained for stimulus amplitudes of 9 pN and 12 pN, respectively.

observed only when the stimulus frequency was below the resonance frequency of the hair bundle.

To test whether the observed quasiperiodic transition corresponds to torus breakdown, a line is drawn from the center of the ring to each point in the sequence, and the angle formed by these lines and the abscissa is computed. This series of angles yields a cirlcle map, $\theta_{n+1} = f(\theta_n)$. When chaos arises from a quasiperiodic transition via torus breakdown, points fall off the surface of a 2-torus, since chaotic dynamic can be described by no fewer than three state variables. As a result of the torus breakdown, the map, f, becomes noninvertible (multiple θ_{n+1} values for a given θ_n) and ceases to be a function [26]. As seen in Figure (2.3b), the map is non-invertible for a weak stimulus. It approaches an invertible map when a stronger stimulus is applied to the bundle, indicating the disappearance of low-dimensional chaos.

We note that quasiperiodic transitions to chaos exist in multiple forms, reported in different dynamical systems. In our measurements of hair bundle motion, the ring structure in the Poincaré map and the non-invertible circle map together indicate the torus-breakdown route to chaos. The data therefore collectively show that a chaotic attractor exists in the weak stimulus regime, in which the Poincaré map exhibits a cloud. To test the robustness of this analysis, we performed numerical simulations of purely stochastic systems, as well as non-chaotic systems with superposed stochastic processes, and verified that they do not show signatures of torus breakdown (see Appendix).

We repeated the above experiments at different frequencies of the imposed drive. For stimulus frequencies near the hair bundle's natural frequency, the Poincaré maps transition directly from a cloud (chaos) to a point (limit cycle), bypassing quasiperiodic dynamics (see Appendix). For stimulus frequencies above the hair bundle's resonance frequency, the hair bundle exhibits a flicker between 1:1 and 2:1 mode-locking, over a range of forcing amplitudes (see Appendix).

2.2.4 Complexity and Entropy

An additional test for the presence of low-dimensional chaos in a nonlinear system can be obtained from measurements of the permutation entropy and statistical complexity [48, 49, 50, 51]. Beginning with a time series, $[x_1,...,x_N]$, we take sub-chains of length d, $([x_i,...,x_{i+d-1}])$. There are $d!$ possible permutations of amplitude ordering within the sub-chain (d! different states). A data set of length N produces $N-(d-1)$ sub-chains. The probability distribution, P, of these states is used to calculate the normalized Shannon entropy, $H(P)$,

$$S(P) = -\sum_{i=1}^{i=d!} p_i \ln(p_i) \tag{2.5}$$

$$H(P) = \frac{S(P)}{\max(S)} = \frac{S(P)}{\ln(N)} \tag{2.6}$$

and the Jensen-Shannon complexity,

$$C_{js} = -2\frac{S(\frac{P+P_e}{2}) - \frac{1}{2}S(P) - \frac{1}{2}S(P_e)}{\frac{N+1}{N}\ln(N+1) - 2\ln(2N) + \ln(N)} H(P) \tag{2.7}$$

where P_e is the probability distribution of maximum entropy (with all states equally probable).

All possible probability distributions are confined to a specific region in the complexity-entropy plane. Jointly, the two measurements allow one to determine whether a chaotic attractor or stochastic noise dominates the dynamics of a system. The lower part of the complexity-entropy region (low-complexity) is occupied by probability distributions of stochastic signals, while the high-complexity region is occupied by probability distributions of signals with low-dimensional chaos. We apply this test to our measurements of spontaneously oscillating hair bundles (Figure 2.4a). We selected d=5, which yields 120 (i.e. 5!) possible states. Similar results were obtained for d=4 and d=6.

Sub-sampling is a useful technique for extracting a low-dimensional chaotic process from a signal contaminated by noise. A purely stochastic process is hardly affected by sub-sampling; if a chaotic attractor is present in the system, however, it may emerge in the sub-sampled data [52]. Recordings of hair bundle oscillations were sampled at 1 kHz, resulting in a Nyquist frequency of 500 Hz. Sub-sampling every forth point reduces the Nyquist frequency to 125 Hz, sufficiently above the dominant frequency in the signal ($\sim$20 Hz). The sub-sampled data set yields statistical features of low-dimensional chaos (Figure 2.4a).

2.2.5 Kolmogorov Entropy

Kolmogorov entropy quantifies the level of chaos in the trajectory of a dynamical system [53]. Given knowledge of the state of a system at a particular time, obtained with some uncertainty, Kolmogorov entropy (K-entropy) measures how well one can predict its state at a later time. K-entropy therefore provides a measure of how rapidly neighboring trajectories diverge, and reflects the rate at which the system is producing information. Limit cycles produce no information: for a given observation of the state of the system, all future states can be predicted with the same uncertainty as the original measurement. In contrast, systems exhibiting either low- or high-dimensional chaos constantly produce information. Hence, K-entropy is zero for limit cycles, positive for systems

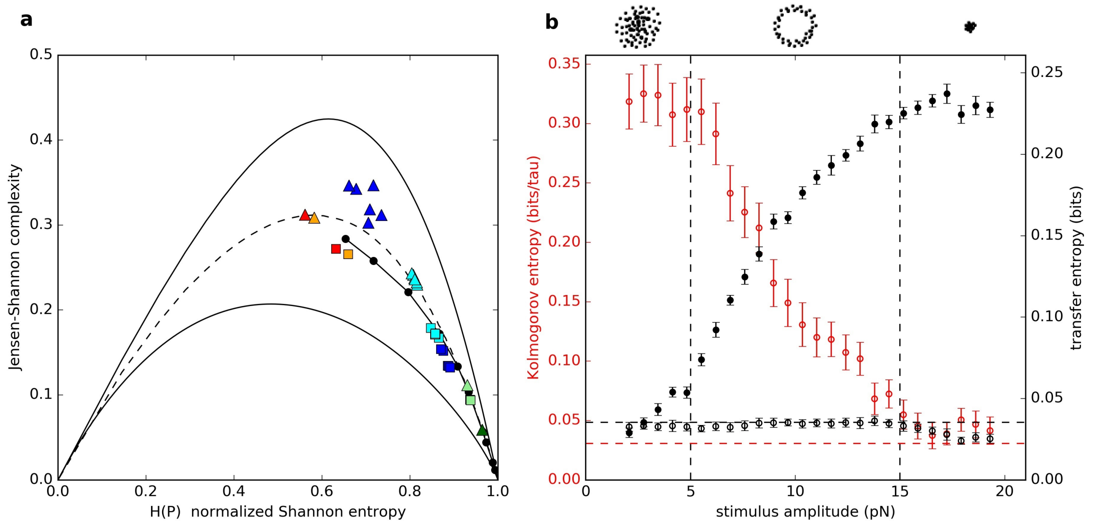

Figure 2.4: (**a**) Complexity-entropy diagram for the spontaneously oscillating hair bundle in Figure (2.2). For all data sets, "■" and "▲" represent fully sampled and sub-sampled data sets, respectively. Blue and teal colors represent raw hair bundle oscillation data and phase-shuffled surrogate data, respectively. Red represents the time series of a numerical simulation of the normal form equation for the supercritical Hopf bifurcations, driven by noise. Orange represents the corresponding phase-shuffled surrogate data set of this Hopf oscillator. Dark green and light green represent telegraphic noise and the corresponding surrogate data, respectively. "●" corresponds to fractional Brownian motion with Hurst exponent ranging from 0.02 to 0.98. The black curves confine all possible probability distributions. The dashed curve is the half-way point between the upper and lower bounds and serves as an approximate boundary between stochastic and chaotic processes. (**b**) The Kolmogorov entropy of an oscillatory hair bundle subject to a sinusoidal drive ("○"), and transfer entropy from stimulus to hair bundle ("●"). As a control ("○"), transfer entropy from hair bundle to stimulus is also plotted as a function of the stimulus amplitude. Vertical dashed lines delineate approximate regions that correspond to Poincaré maps displaying cloud, ring, and point structures, as illustrated by the schematic diagrams above the graph. Noise floors are indicated by horizontal dashed lines. The noise floor on the K-entropy is estimated by tracking the motion of a passive hair bundle driven by a 10 – 25 pN sinusoidal stimulus. The noise floor on the transfer entropy is estimated based on bundle oscillations in the absence of a stimulus. Uncertainties in K-entropy are estimated by taking the standard deviation of the residuals from the linear fit of Shannon entropy with time. Uncertainties in transfer entropy are estimated from a bootstrapping technique that incorporates the uncertainties in position measurements.

with low-dimensional chaos or noise, and infinite for purely stochastic processes.

To calculate the K-entropy, we divide the reconstructed phase space into hypercubes, and select a starting hypercube to be one that contains many points of the trajectory. We track the trajectories emerging from these points to calculate a time-dependent probability distribution over the hypercubes. The resulting distribution yields the Shannon entropy as a function of time; its time-averaged derivative is defined to be the K-entropy [53, 54, 27]. An embedding dimension of five was chosen for this analysis; nearly identical results were obtained with four or six embedding dimensions. The choice of the number of bins per dimension did not affect the results of this analysis. We used two bins per dimension, a natural choice due to the bimodal distribution in position of the spontaneously oscillating hair bundle.

We observe that the Kolmogorov entropy associated with active bundle motility is reduced by the application of a sinusoidal drive (Figure 2.4b). The majority of the reduction in K-entropy occurs during the quasiperiodic transition from chaos to order, the regime in which the Poincaré maps produce a ring structure. K-entropy plateaus near zero, for forcing amplitudes above $\sim$15 pN. We note that a noiseless system would plateau exactly at zero; the finite value of the plateau is due to noise inherent in the experimental recording.

Detection by an individual hair cell is quantified by calculating the transfer entropy from the stimulus signal to the receiver response [55]. For systems exhibiting large innate oscillations in the absence of stimulus, we propose that transfer entropy is a more appropriate measure of detection than the traditional linear response function, as it avoids yielding a spurious detection of zero-amplitude signals. Further, in contrast to measures such as mutual information, this measure explicitly identifies the direction of information flow. For a continuous signal, calculation of transfer entropy requires partitioning the range of the signal and assigning a state to each discrete bin. The transfer entropy from process J to process I is defined as

$$T_{J\to I} = \sum p(i_{n+1}, i_n^{(k)}, j_n^{(l)}) \log \frac{p(i_{n+1} \mid i_n^{(k)}, j_n^{(l)})}{p(i_{n+1} \mid i_n^{(k)})}, \tag{2.8}$$

where $i_n^{(k)} = (i_n, ..., i_{n-k+1})$ are the k most recent states of process I. Therefore, $p(i_{n+1} \mid i_n^{(k)}, j_n^{(l)})$ is the conditional probability of finding process I in state i_{n+1} at time $n+1$, given that the previous k states of process I were $i_n^{(k)}$ and given that the previous l states of process J were $j_n^{(l)}$. The summation is performed over the length of the time series, as well as over all accessible states of processes I and J. Transfer entropy $T_{J \to I}$ is a measure of how much one's ability to predict the future of process I, given its history, is improved by knowledge of the history of J.

To analyze experimental recordings of hair bundle oscillations, we discretized the signal into two bins, due to the bimodal distribution in position of the hair bundle; similar results were obtained when using three or four bins. The choice of k and l had little effect on our results so we select $k = l = 4$. The transfer entropy from the applied stimulus to the hair bundle rises above zero for signals of $\sim$3 pN. The observed detection threshold is even lower when a stimulus is applied at the resonance frequency of the cell (see Appendix).

2.2.6 Theoretical Model

To capture the chaotic dynamics of an oscillatory hair bundle, we apply a variant of a previously proposed model [24], developed to account for the complex multi-mode hair bundle oscillations. The model was shown to reproduce a number of experimental observations. It captured the sporadic transitions between quiescence and innate oscillation exhibited by hair bundles. Further, it displayed multi-mode phase-locking to the stimulus over a wide range of driving frequencies, in agreement with experimental results. Finally, it reproduced the observed suppression and recovery of oscillation, following strong mechanical forcing. The model consists of three dynamical variables, the minimum dimension capable of supporting a chaotic regime.

The transition between oscillatory and quiescent states is described using the normal form equation of the subcritical Hopf bifurcation (Bautin bifurcation) [29],

$$\frac{dz}{dt} = z(\mu - i\omega_0 + A|z|^2 - B|z|^4) + f_A \cos(w_d t), \tag{2.9}$$

where $z(t)$ describes the dynamic state of the bundle with the real part, $x(t)$, representing the bundle position. f_A, ω_d, and ω_0 denote the driving force, driving frequency, and natural frequency, respectively. The fifth-order term in z is included to capture the subcritical Hopf bifurcation, which was shown to describe well the complex bundle dynamics. $A = B = 10$ and $\omega_0 = 1$, unless otherwise stated.

The control parameter, μ, is associated with the probability of the system being in the oscillatory or the quiescent state. We assume the parameter to be a real-valued dynamic variable, with its rate of change described by

$$\frac{d\mu}{dt} = k_{on} - k_{off}\Theta(x - x_0) + \alpha f_A, \tag{2.10}$$

where k_{on} and k_{off} are rate constants. The Heaviside step function, Θ, serves as an approximation of the Boltzmann distribution related to the opening probability of the ion channels [7]. We introduce here the αf_A term to the original model, to capture the entrainment of the bundle by a strong stimulus and to reproduce the torus breakdown transition from chaos as stimulus amplitude is varied. $\alpha = 0.15$ unless otherwise stated.

We demonstrate that numerical simulations based on this model reproduce well the characteristic features of the experimental results. Sinusoidal stimuli of linearly increasing amplitude elicit a quasiperiodic transition from chaos to order via reverse torus breakdown (see Appendix). This transition is accompanied by a reduction in the Kolmogorov entropy similar to our experimental recordings. We note that higher dimensional models would certainly capture more details of the experimentally measured hair bundle response. However, we aim to find the simplest model that can reproduce the experimental results specific to this study, namely signatures of an underlying chaotic attractor. A simple model has a more tractable parameter space, allowing us to to isolate the impact of chaos on the response of the system.

We next explore the effects of chaoticity on the sensitivity to a weak stimulus. In numerical simulations, chaoticity is most easily quantified by the largest Lyapunov exponent of the system[29]. In the absence of a stimulus, Lyapunov exponents are calculated by tracking the rate of divergence of neighboring trajectories in the 3-dimensional phase space. We vary the parameters of the model, to obtain a broad range of Lyapunov exponents. For each set of parameters, we impose a stimulus signal below, above, and at the natural frequency of the oscillator. For simplicity, we use a square wave stimulus with stochastic variation of the period. We compute the transfer entropy from the imposed stimulus to the hair bundle response, for each of the Lyapunov exponents, and present the results in a scatter plot. For frequencies at or away from the characteristic frequency of the bundle, the model shows enhanced sensitivity to information transfer when poised in the chaotic regime (Figure 2.5).

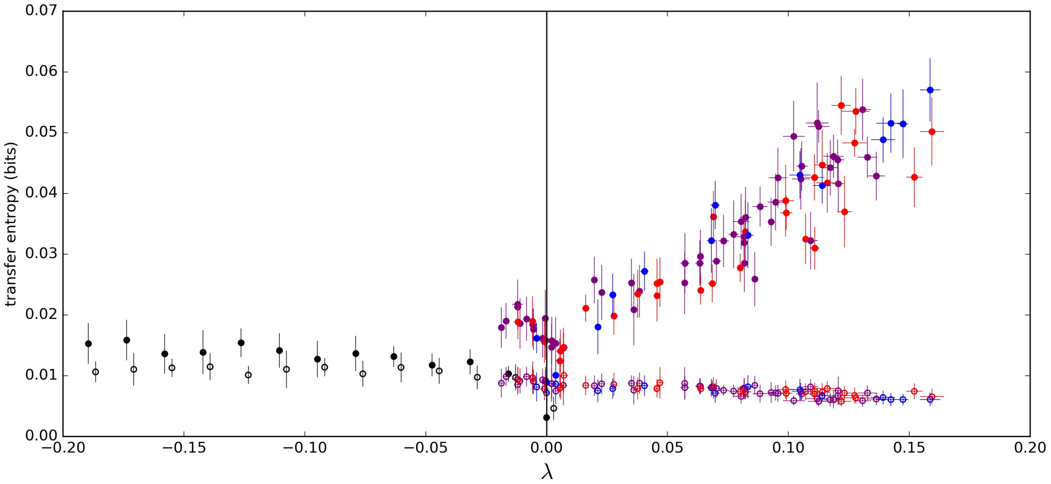

Figure 2.5: Scatter plot of the largest Lyapunov exponent (λ) versus the transfer entropy from a stimulus to hair bundle oscillator, obtained from a numerical simulation. The applied stimulus was a square wave with stochastic variations of the period. The mean of these periods was set to $\frac{1}{2\pi\omega_0}$ (on resonance) with a standard deviation that is 30% of its mean. The amplitude was set to $f_A = 0.3$. This numerical value corresponds to forcing amplitude of approximately 1 pN. “●", “●", and “●" correspond to variations in parameters k_{on} (0.3 – 0.6), k_{off} (1.0 – 2.2), and x_0 (0.2 – 0.7), respectively. “●" represents variations in the cubic parameter, A ($10^{-5} - 0.15$), when the system is poised in the limit cycle regime. In this regime, the Lyapunov exponent of largest magnitude is calculated analytically. As any parameter is varied, all others are held constant ($x_0 = 0.4$, $k_{on} = \frac{5}{12}$, $k_{off} = \frac{7\pi}{12\arccos(0.4)}$, and $A = 10$.) Error bars in transfer entropy are the standard deviation from repeating the calculation on 10 different stimulus forms, each containing $N = 10^5$ data points. Open circles of all colors correspond to calculations of transfer entropy in the reverse direct (bundle to stimulus) and serve as controls.

2.3 Discussion

The auditory system has provided an experimental testing ground for theoretical work on nonlinear dynamics [21, 23], nonequilibrium thermodynamics [56], and condensed matter theory [57]. The fundamental questions on hearing pertain to its sensitivity, frequency selectivity, rapidity of detection, and the role of an active mechanism in shaping the response. Models based on dynamic systems theory have successfully described a number of empirical phenomena. However, the theoretical models have mostly focused on stable dynamics, exploring either the limit cycle regime, or the quiescent regime in the vicinity of a bifurcation.

Our results provide an experimental demonstration that a low-dimensional chaotic attractor arises in the dynamics of active hair bundle motility. Ring-like structures in the Poincaré maps, torus breakdown, positive Kolmogorov entropy, non-integer correlation dimension and the location of the time series in the complexity-entropy plane are all indicators of low-dimensional chaos, not stochastic processes. We estimate that three to six independent variables are needed to correctly characterize the dynamics of the system.

Further, we find that chaos is removed by the application of a signal, with different transitions from chaos to order observed when oscillations are entrained by stimuli below, near, or above the characteristic frequency of the cell. Hair bundles have thus far been viewed as nonlinear mechanical detectors, and the linear response used to characterize their sensitivity. We propose that information theory provides a useful and complementary tool for analyzing the response of a hair cell, which can be viewed as a computational device that serves to extract information about the external acoustic environment. We hence apply an information theoretic approach to quantify the detection of a signal by an individual hair cell. Hair bundles poised in the chaotic regime exhibit measurable increases in transfer entropy even at pN levels of stimulus, indicating that chaotic dynamics of innate motility are consistent with high sensitivity of detection.

Our theoretical model, which includes a feedback equation for the control parameter of the system, describes well the dynamics observed experimentally. When poised in the chaotic regime, the system shows an enhanced sensitivity to weak stimulus. We therefore propose that hair cells of the auditory system harness the presence of chaos to achieve high sensitivity. We further hypothesize that chaotic dynamics may be a ubiquitous feature of nonlinear biological systems, which typically exhibit many degrees of freedom. It is therefore important to understand the impact of chaos on the sensory perception in living systems.

2.4 Experimental Techniques

Experiments were performed *in vitro* on hair cells of the amphibian sacculus, an organ specializing in low-frequency air- and ground-borne vibrations. Sacculi were excised from the inner ears of North American bullfrogs (*Rana catesbeiana*), and mounted in a two-compartment chamber [8]. Spontaneously oscillating hair bundles were accessed after digestion and removal of the overlying otolithic membrane [11]. All protocols for animal care and euthanasia were approved by the UCLA Chancellor's Animal Research Committee in accordance with federal and state regulations. To deliver a stimulus to the hair bundles, we used glass capillaries that had been pulled with a micropipette puller. These elastic probes were treated with a charged polymer that improves adhesion to the hair bundle. Innate oscillations persisted after the attachment of probes with stiffness coefficients of $\sim 100\ \mu$N/m. The piezoelectric actuator was controlled with LabVIEW to apply sinusoidal stimulation of varying amplitudes for selected constant frequencies. Hair bundle motion was recorded with a high-speed camera at frame rates of 500 Hz or 1 kHz. The records were analyzed in MATLAB, using a center-of-pixel-intensity technique to determine the mean bundle position in each frame. Typical noise floors of this technique, combined with stochastic fluctuations of bundle position in the fluid, were 3 – 5 nm. Figure (2.1a) shows representative traces of active bundle motion, subject to mechanical forcing.

2.5 Appendix

2.5.1 Simulated Control Data Sets

We use several simulated data sets as controls (Figure 2.6). Telegraphic noise was simulated by numerically solving the Langevin equation with a quartic potential,

$$\lambda \frac{dx}{dt} = \eta(t) - \frac{dU(x)}{dx}, \tag{2.11}$$

where

$$U(x) = ax^4 + bx^2. \tag{2.12}$$

We use $a = \frac{1}{4}$, $b = -5$, and $\lambda = 1$. For $\eta(t)$, we use Gaussian white noise with a standard deviation of 5.

As another control, we numerically solve the normal form equation for the Hopf bifurcation, up to cubic order,

$$\frac{dz}{dt} = (\mu - i\omega_0 + A|z|^2)z + \eta_z(t), \tag{2.13}$$

with $A = 10$, $\mu = \omega_0 = 1$, and Gaussian white noise added to real and imaginary parts of z ($\eta_z = \eta_x + i\eta_y$), each with standard deviation of 0.1.

As a third control, we use a sine wave and superpose Gaussian white noise (signal-to-noise ratio = 5).

2.5.2 Test for Determinism

To confirm that a deterministic component is present in the spontansouly oscilating hair bundle, we performed the direct test for determinism [36]. This method relies on reconstructing the phase space using delayed coordinates and comparing the direction of local flow throughout the phase

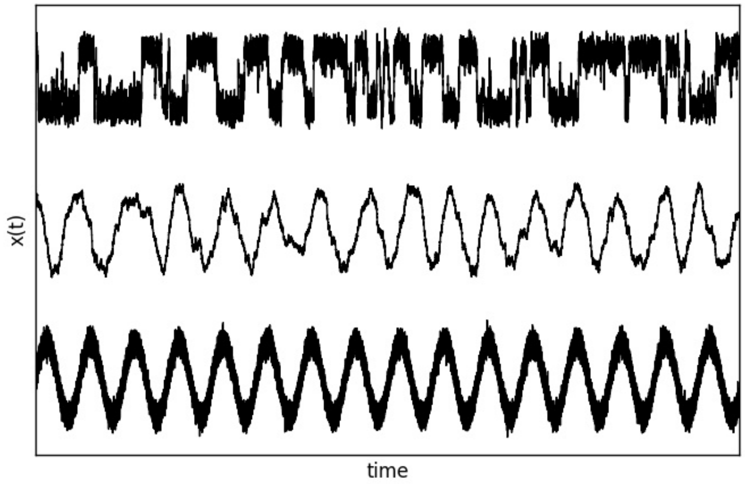

Figure 2.6: Data sets used as controls. Telegraphic noise (top), suprcritical Hopf system (middle), and sine wave with added noise (bottom).

space. We divide the phase space into hypercubes and construct unit vectors from the point at which a trajectory enters a given hypercube to that at which it exits. For a purely stochastic system, the sum of unit vectors associated with a given hypercube decreases as more vectors are added. However, for deterministic systems, these unit vectors generally point in the same direction. As a result, the sum should remain close to unity as vectors are added.

We used 5 embedding dimensions and divided the phase space into 10 bins per dimension. Similar results were obtained for choices of 4 and 6 embedding dimensions and choices of 4, 7, and 12 bins. Using Welch's unequal variances t-test, The raw data is distinguishable from the phase-shuffled surrogate data with p-values ranging from $0.008 - 0.015$ for number of passes $2 - 50$. Welch's t-test is appropriate since the two distributions are of different sample size and variance. Further, we demonstrate that this method is robust when a deterministic signal is contaminated with noise (Figure 2.7).

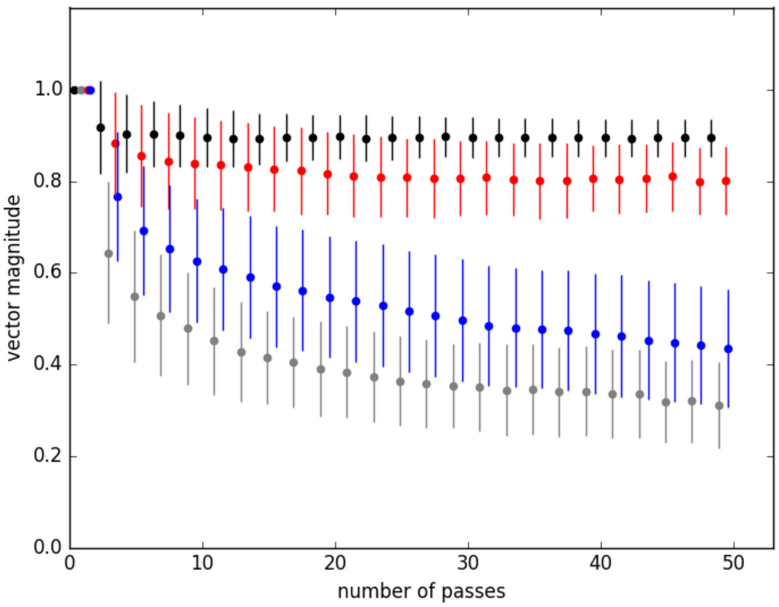

Figure 2.7: Direct test for determinism on a spontaneously oscillating hair bundle. Red and blue points represent the raw data and phase-shuffled surrogate data, respectively ($N = 1.8 \times 10^5$ data points). Black points represent a sine wave with additive white noise (signal-to-noise ratio = 5). Grey points represent telegraphic noise. Points and error bars represent the mean and standard deviation across all occupied hypercubes in the phase space.

2.5.3 False Nearest Neighbor Test

We perform the false nearest neighbor test as another way of estimating the embedding dimension of the hair cell system. This method relies on reconstructing the phase space using delayed coordinates. When the embedding dimension is too low, not all points that lie near each other will do so because of the dynamics. Instead, some may be neighbors because the structure of the attractor has been projected into a lower dimensional space. When the embedding dimension is high enough to fully unfold the attractor, there will be no more false nearest neighbors. However, if the signal is contaminated by stochastic processes, there will always remain some fraction of false nearest neighbors. With experimental data contaminated with noise, we look for a plateau in the fraction of false nearest neighbors as the embedding dimension is increased. Using the method described in [37] on a long recording of spontaneous hair bundle oscillations, we find that the attractor is fully unfolded with six embedding dimensions (Figure 2.8), a result consistent with our previous finding. Use used $R_{tol} = 15$ and $A_{tol} = 2.5$ as the thresholds for identifying false nearest neighbors. However, the optimal embedding did not change upon varying either of these parameters ($R_{tol} = 10$ or 20 and $A_{tol} = 2$ or 3). The embedding dimension was negligibly affected by weak or moderate stimulus. Only during strong stimulus, $\sim$15 pN, was the embedding dimension reduced.

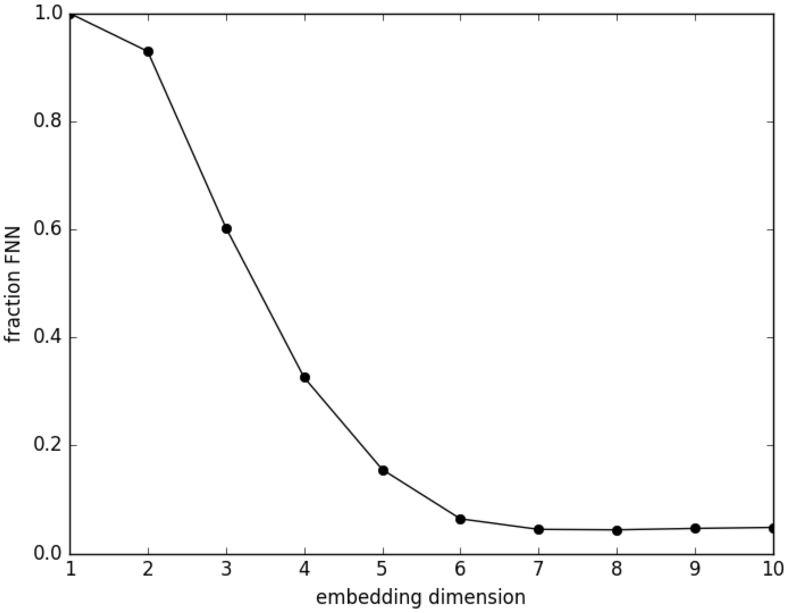

Figure 2.8: False nearest neighbor test performed on a spontaneously oscillating hair bundle recording with $N = 1.8 \times 10^5$ data points.

2.5.4 Stimulus Near the Resonance Frequency

When hair bundles are stimulated near resonance, the Poincaré maps do not exhibit quasiperiodic transitions. Instead, as the forcing amplitude increases, the cloud in the I_n–I_{n+1} plane shrinks in size and collapses onto a point (Figure 2.9). K-entropy decreases with increasing amplitude of the drive, while information transmission increases (Figure 2.10), comparable to the dependence observed with below-resonance stimulus. As expected, the threshold for detecting weak stimulus is lower for the on-resonance case.

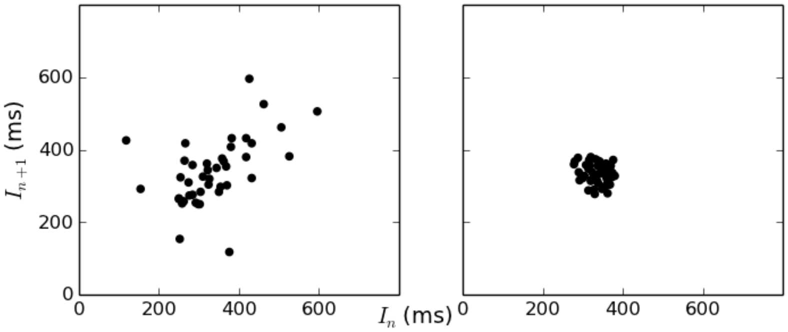

Figure 2.9: Poincaré maps representing spontaneous oscillations of hair bundles (left) and hair bundle response to a sinusoidal stimulus of $\sim$5 pN applied near the resonance frequency (right).

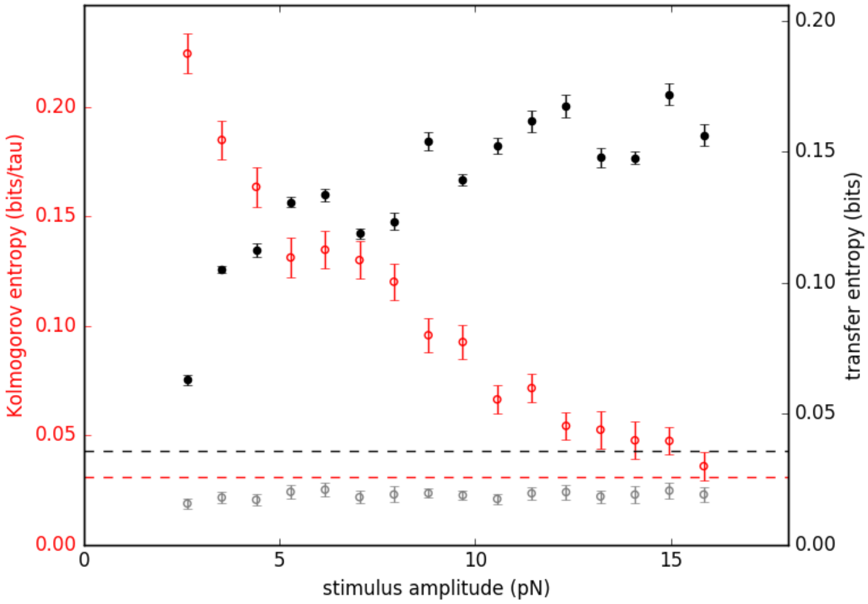

Figure 2.10: The Kolmogorov entropy of an oscillatory hair bundle subject to a sinusoidal drive (red), transfer entropy from the stimulus to the bundle (black-filled), and transfer entropy from bundle to stimulus (black-open) plotted as a function of the stimulus amplitude. Noise floors are indicated by horizontal dashed lines. Stimulus frequency was selected to be near the resonance frequency of the hair bundle.

2.5.5 Stimulus Above the Resonance Frequency

A different type of transition from chaos to order is observed when the stimulus is applied at frequencies above resonance. Rather than displaying a ring, the points on the Poincaré maps cluster into regions corresponding to integer multiples of the resonance frequency, indicative of high-order mode-locking (Figure 2.11). Rather than migrating around the edge (as in the case of a quasiperiodic transition), consecutive points cross over the center. Upon higher amplitudes of the drive, the cluster corresponding to 1:1 mode-locking dominates, and other clusters vanish. K-entropy decreases with increasing amplitude of the drive, while information transmission increases (Figure 2.12), comparable to the dependence observed with below-resonance stimulus. However, K-entropy initially increases for weak forcing. We attribute this initial increase in K-entropy to flicker between 1:1 and 2:1 modes in the phase-locking of the bundle to the stimulus. We note that this flicker corresponds to phase-slips, which have been observed and characterized in prior studies [58]. We have shown that the hair bundle exhibits low-dimensional chaos in the absence of stimulus, however we are unable to identify the route from chaos to order for above-resonance stimulus using Poincaré maps.

2.5.6 Transition to Chaos in the Theoretical Model

A sinusoidal stimulus of linearly increasing amplitude was applied to the theoretical model. With $\alpha > 0$, the model exhibits a quasiperiodic transition from chaos to order as forcing amplitude is increased (Figure 2.13).

2.5.7 Poincaré Maps and Stochastic Processes

Our analysis of experimental data indicate that the quasiperiodic regime observed at moderate stimulus levels corresponds to the torus-breakdown route to chaos. This finding implies that the cloud structure observed at weak stimuli contains an underlying chaotic attractor. Here, we preform numerical simulations on three systems, to obtain corresponding Poincaré and circle maps, and

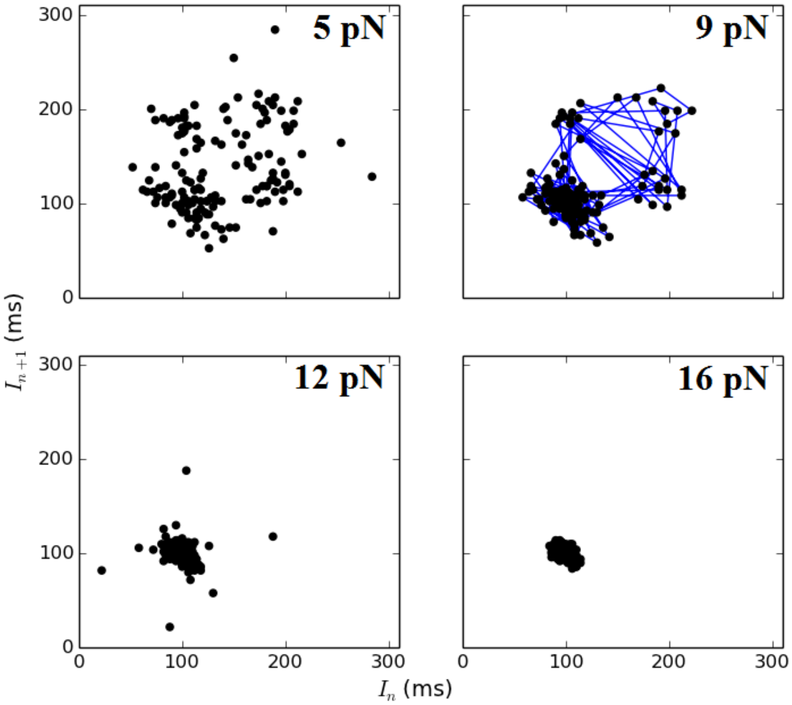

Figure 2.11: Poincaré maps representing oscillations of hair bundles driven by a sinusoidal stimulus above the resonance frequency ($\omega \sim \frac{5}{3}\omega_0$). The four clusters of points indicate a flicker between 1:1 and 1:2 mode-locking. Blue lines connect consecutive points in the series.

verify that different results are obtained for non-chaotic systems with superposed noise.

First, we obtain time traces of telegraphic noise, generated by simulating a particle in a quartic potential driven by stochastic noise and a superposed sinusoidal force. For weak stimuli, the interval Poincaré maps of telegraphic noise form a cloud, and at strong stimuli, the maps collapse onto a point. In the intermediate range stimulus amplitudes, the system does not exhibit a ring-like structure, but rather shows complex mode-locking behavior (Figure 2.14). 1:1, 1:2, and 1:3 mode-locking can be seen in the Poincaré map. Next, we tested whether simulations of the supercritical Hopf oscillator with superposed noise show similar behavior to the experimental records. While the Poincaré maps do exhibit similar quasiperiodic behavior (Figure 2.15), the corresponding circle map forms an invertible function indicative of a non-chaotic system. We obtained Poincaré and

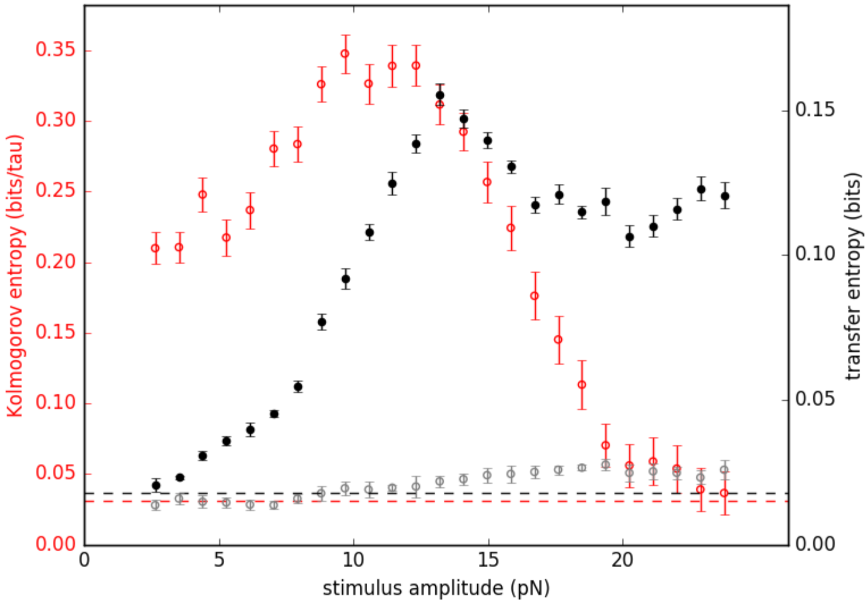

Figure 2.12: The Kolmogorov entropy of an oscillatory hair bundle subject to a sinusoidal drive (red), transfer entropy from the stimulus to the bundle (black-filled), and transfer entropy from bundel to stimulus (black-open) plotted as a function of the stimulus amplitude. Noise floors are indicated by horizontal dashed lines. Stimulus frequency was above the resonance frequency of the hair bundle ($\omega \sim \frac{5}{3}\omega_0$).

circle maps similar to Figure 2.15 for the supercritical Hopf oscillator with noise superposed on the phase variable, or parametric noise superposed on the control parameter μ.

We observed the same regime of quasiperiodicity with a corresponding invertible circle map, for a driven, noisy harmonic oscillator. These simulations demonstrate that this technique is robust in the presence of stochastic processes, as an invertible circle map is not consistent with torus breakdown. Hence, it confirms that the structure in the Poincaré maps of our experimental recordings are a manifestation of a chaotic attractor.

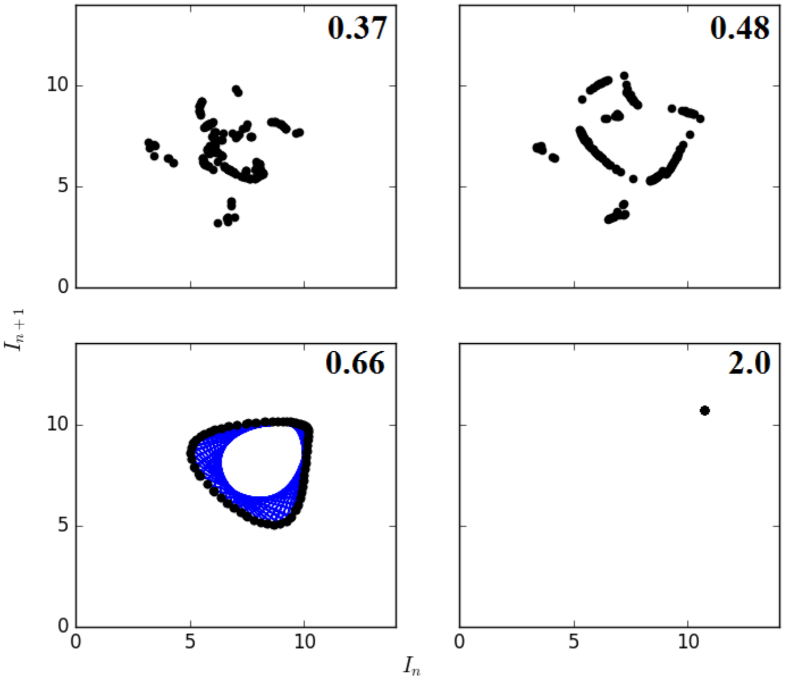

Figure 2.13: (Model) Poincaré maps representing oscillations of hair bundles driven by a sinusoidal stimulus below the resonance frequency ($\omega \sim \frac{2}{3}\omega_0$), for a range of forcing amplitudes, as indicated in the top right corners. Blue lines connect consecutive points in the series. $x_0 = 0.4$, $k_{on} = \frac{5}{12}$, $k_{off} = \frac{7\pi}{12\arccos(0.4)}$,$A = 10$, and $\alpha = 0.15$.

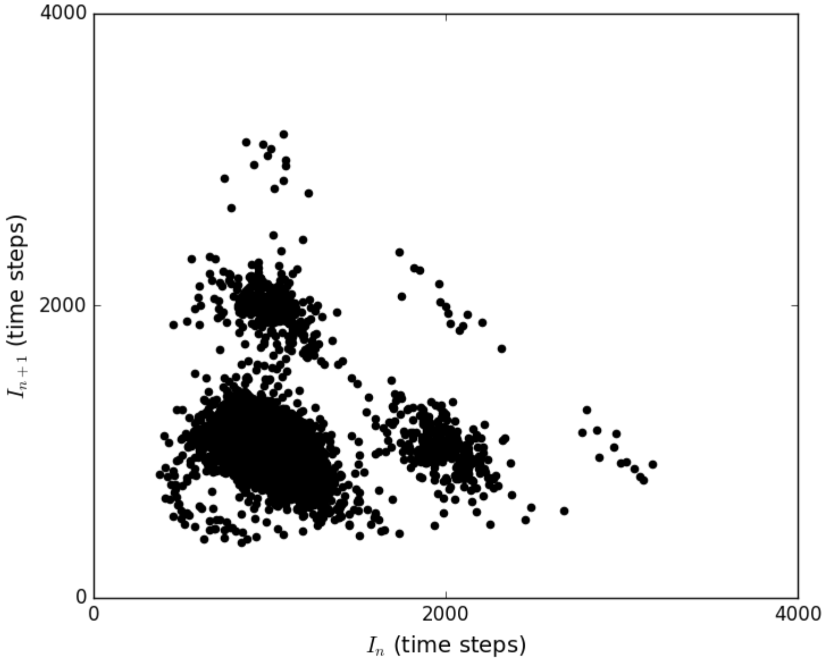

Figure 2.14: Poincaré map representing telegraphic noise generated by simulating a particle in a quartic potential driven by white noise and sinusoidal forcing.

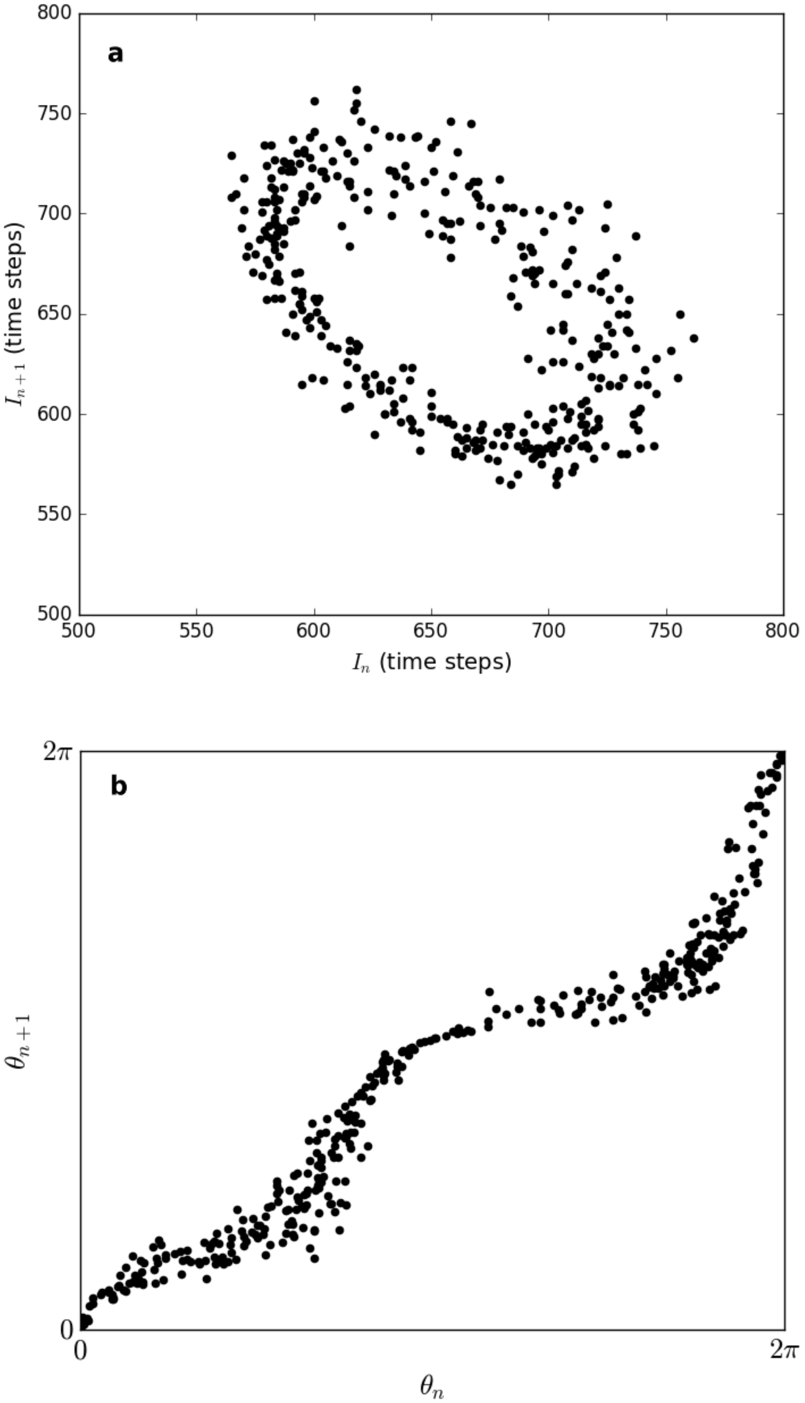

Figure 2.15: (**a**) Poincaré map representing a simulation of the supercritical Hopf system driven by white noise and sinusoidal forcing below the resonance frequency ($\omega \sim \frac{2}{3}\omega_0$). (**b**) Corresponding Circle Map.

CHAPTER 3

Chaos and Signal Detection by Individual Hair Cells

3.1 Introduction

In this chapter, we show that, for a wide range of parameter conditions, additive noise induces chaotic dynamics. We use a simple theoretical model to demonstrate that extreme sensitivity and rapid response time of the chaotic system both occur over a wide parameter range, without the need for a feedback equation. This alternative view could explain how the performance of the hair cells would be robust to noise as well as to changes in parameters, and how it can achieve extreme sensitivity in the oscillatory regime, from which otoacoustic emissions can originate. In the numerical model, we vary the degree of chaos and show that the sensitivity to different stimulus waveforms is enhanced and the response time reduced, as the degree of chaos is increased. We propose to view the hair cell not just as a mechanical resonator, but as an information processor that extracts selective information from its acoustic environment. We then show that the amount of information extracted by the active oscillator from an imposed stimulus waveform is maximized in the weakly chaotic regime. We verify our theoretical predictions by experiments performed on *in vitro* preparations of the bullfrog sacculus. By varying the viscosity and the ionic conditions of the fluid in which the hair bundles are immersed, we modulate the chaoticity of their dynamics, and we measure the sensitivity, information transfer, and temporal response to various imposed signals. We find consistent experimental agreement with all of the theoretical predictions of the model. We therefore propose that the instabilities giving rise to chaotic dynamics enhance the sensitivity and temporal resolution of the auditory and vestibular hair cells.

3.2 Numerical Model

We use the normal form equation for the supercritical Hopf bifurcation with additive Gaussian white noise, $\eta_z(t)$:

$$\frac{dz(t)}{dt} = (\mu + i\omega_0)z(t) - (\alpha + i\beta)|z(t)|^2 z(t) + \eta_z(t), \tag{3.1}$$

where

$$z(t) = x(t) + iy(t), \tag{3.2}$$

$$\eta_z(t) = \eta_x(t) + i\eta_y(t), \tag{3.3}$$

$$\langle \eta_x(t)\eta_x(t')\rangle = \langle \eta_y(t)\eta_y(t')\rangle = 2D\delta(t-t'), \tag{3.4}$$

and

$$\langle \eta_x(t)\eta_y(t')\rangle = 0. \tag{3.5}$$

Here, $x(t)$ represents the bundle position, while $y(t)$ reflects internal parameters of the bundle and is not assigned a specific measurable quantity. μ represents the control parameter of the system, with positive values yielding a limit cycle and negative values resulting in a stable fixed point. The autonomous angular frequency of this system in the absence of noise is $\Omega_0 = \omega_0 - \beta r_0^2$, where $r_0 = \sqrt{\frac{\mu}{\alpha}}$ is the radius of the limit cycle. Thus, ω_0 represents the angular frequency at the Hopf bifurcation ($\mu = 0$). α and β characterize the cubic nonlinearity of the system, while D represents the noise strength. Auditory and vestibular stimuli induce lateral deflections on the hair bundle, so we consider forces in the $\hat{x}$ direction, which coincides with the direction of spontaneous oscillation.

A characteristic feature of chaotic systems is that neighboring solutions to the differential equations diverge exponentially with time: $|\Delta z(t)| \approx e^{\lambda t}|\Delta z(0)|$, where $\Delta z(t)$ is the separation between two neighboring trajectories in phase space, and λ is the Lyapunov exponent [59]. Thus, small perturbations to a chaotic system will have a drastic impact on future dynamics. The Lyapunov exponent characterizes how quickly the perturbations grow and serves as a measure of the degree of chaos. A stable fixed point is characterized by a negative Lyapunov exponent, as neighboring trajectories converge to the same location. A limit cycle has a Lyapunov exponent equal to zero, since a perturbation tangential to the direction of motion neither grows nor shrinks. A positive value of the Lyapunov exponent indicates chaotic dynamics, with larger values corresponding to more irregular behavior and weaker predictability.

In the presence of stochastic processes, the Lyapunov exponent is calculated by measuring the exponential rate of divergence of two neighboring trajectories, subjected to identical realizations of noise (i.e. common noise) [60, 61, 62]. This has been observed in other 2-dimensional systems[63] and is commonly referred to as noise-induced chaos. In Fig. 3.1, we demonstrate that the additive noise to Eq. 3.1 induces chaotic dynamics, as it causes solutions to diverge exponentially. Further, the attractor exhibits a fractal structure, which is ubiquitous to chaotic systems [29]. The simplicity of this model allows us to use an analytic approximation of the Lyapunov exponent, applying Fokker-Planck theory (see Methods):

$$\lambda \approx \frac{|\beta| D}{\mu}. \tag{3.6}$$

Without loss of generality, we set $\alpha = \Omega_0 = 1$, scaling the units of length and time. The remaining three parameters, μ, β, and D are used to modulate the Lyapunov exponent.

The Lyapunov exponent provides the simplest measure of chaos for numerical models. However, the Kolmogorov entropy (K-entropy) constitutes a more appropriate measure of chaoticity for experimental data sets, which inherently contain measurement noise and are more limited in duration than typical numerical simulations [38]. Similar to the Lyapunov exponent, the K-entropy measures the divergence rate of neighboring trajectories [53]. Specifically, K-entropy quantifies the rate at which phase space information is lost due to an expansion of measurement uncertainty. K-entropy is zero for non-chaotic systems, non-zero for chaotic systems, and infinity for white noise. We therefore use the K-entropy as our measure of chaoticity when making direct comparisons between theory and experiment.

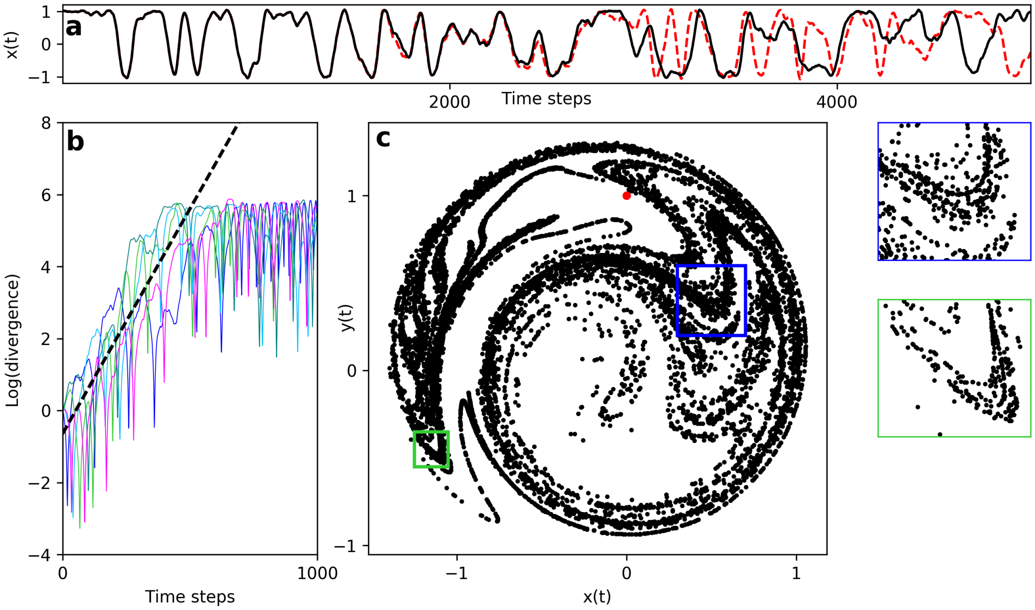

Figure 3.1: (**a**) The divergence of two neighboring solutions to Eq. (3.1). The two time-dependent solutions are depicted with black (solid) and red (dashed) lines. (**b**) The natural logarithm of the average separation of neighboring trajectories. Each of the five colors represents an average of 200 pairs of neighboring trajectories, taken with different initial conditions and realizations of common noise. The dashed line represents the linear fit to all of the data within the first 400 time steps. (**c**) The spreading of trajectories throughout the phase space. 10^4 initial conditions were randomly selected in the same neighborhood (red points). After 500 time steps, these solutions spread across the phase space to reveal the fractal structure of the attractor (black points). Side panels show zoomed-in sections corresponding to the colored squares in the main figure.

3.3 Theoretical Results

We next explore the effects of chaos and noise on the system's sensitivity to a weak stimulus. The oscillator demonstrates higher responsiveness to sinusoidal and square wave stimuli when it is poised in the weakly chaotic regime (Fig. 3.2). We note that the traditional linear response function is not an appropriate measure of sensitivity in the oscillatory regime, as it would yield infinite sensitivity at the natural frequency, in the limit of vanishing stimulus amplitude and noise. Instead, we use the amplitude gain at the frequency of the applied signal as a measure of the system's responsiveness [17, 64]. We define $gain = \frac{|\tilde{x}(\omega_{stim})|}{|\tilde{x}_0(\omega_{stim})|}$, where $\tilde{x}(\omega_{stim})$ and $\tilde{x}_0(\omega_{stim})$ are the Fourier components at the stimulus frequency in the presence and absence of stimulus, respectively. Fig. 3.2 shows sample traces that can be used to calculate the gain. Notice that the weakly chaotic regime is easily entrained to off-resonance stimulus frequencies. We consistently find that the chaotic regime is more sensitive than the stable limit cycle regime. Upon a further increase in the chaoticity of the system, reflected by a higher Lyapunov exponent, the sensitivity deteriorates.

We measure the gain of the system in response to an on-resonance sinusoidal stimulus for a wide range of Lyapunov exponent values and noise strengths (Fig. 3.3a). We find that the system is most responsive in the weakly chaotic regime (low, but nonzero Lyapunov exponent). Importantly, this is true even at high levels of additive noise (signal-to-noise ratio < 1). Further, we see similar results for off-resonance stimuli (see Appendix).

Next, we explore the effects of chaos and noise on the amount of signal information captured by the detector (transfer entropy [55]). In contrast to measures such as mutual information, transfer entropy explicitly identifies the direction of information flow. For continuous stimulus and response signals, calculation of transfer entropy requires discretizing the range of the signals and assigning a state for each bin (see Methods). We therefore use a square wave stimulus with stochastic variation of the period (burst noise or random telegraph noise) [64]. Such stochastic signals constantly produce new information, and the transfer entropy measures how much of this new information is captured by the detector. The square wave intervals are randomly generated from a flat distribution that spans two octaves on either side of the natural frequency ($\frac{1}{4}\Omega_0$ to $4\Omega_0$). We measure the transfer entropy over a wide range of Lyapunov exponent values and noise strengths and find results consistent with the measurements of the gain (Fig. 3.3b). We also show that consistent results are obtained when μ is used to modulate the Lyapunov exponent in place of β (see Appendix). The weakly chaotic regime is optimal for extracting information from the signal. This

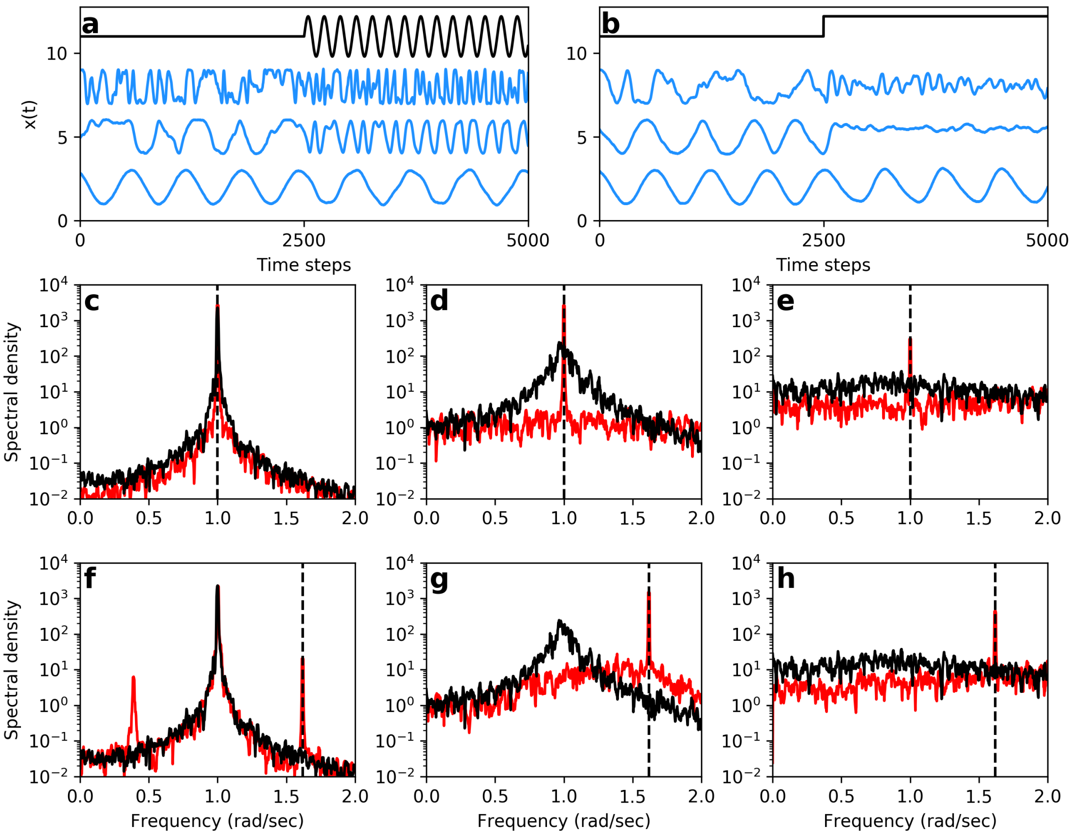

Figure 3.2: (**a-b**) Time-domain responses to (off-resonance) sinusoidal and step stimulus, respectively. The top, black traces show the stimulus waveform. Bottom, middle, and top blue traces represent responses of a system with no chaos, weak chaos, and strong chaos, respectively. The degree of chaos was modulated by varying β and ω_0, while keeping the natural frequency fixed at $\Omega_0 = 1$. (**c-e**) Power spectral density of the response to on-resonance sinusoidal stimulus ($\omega_{stim} = \Omega_0 = 1$, as indicated by the vertical, dashed lines) for systems exhibiting no chaos (c), weak chaos (d), and strong chaos (e). Red and black curves represent the spectral density in the presence and absence of the stimulus, respectively. (**f-h**) Power spectral density of the response to off-resonance sinusoidal stimulus ($\omega_{stim} = \frac{1+\sqrt{5}}{2}\Omega_0$, as indicated by the vertical, dashed lines) for systems exhibiting no chaos (f), weak chaos (g), and strong chaos (h). The stimulus frequency was set to the golden ratio with respect to the natural frequency to avoid mode locking. Red and black curves represent the spectral density in the presence and absence of the stimulus, respectively.

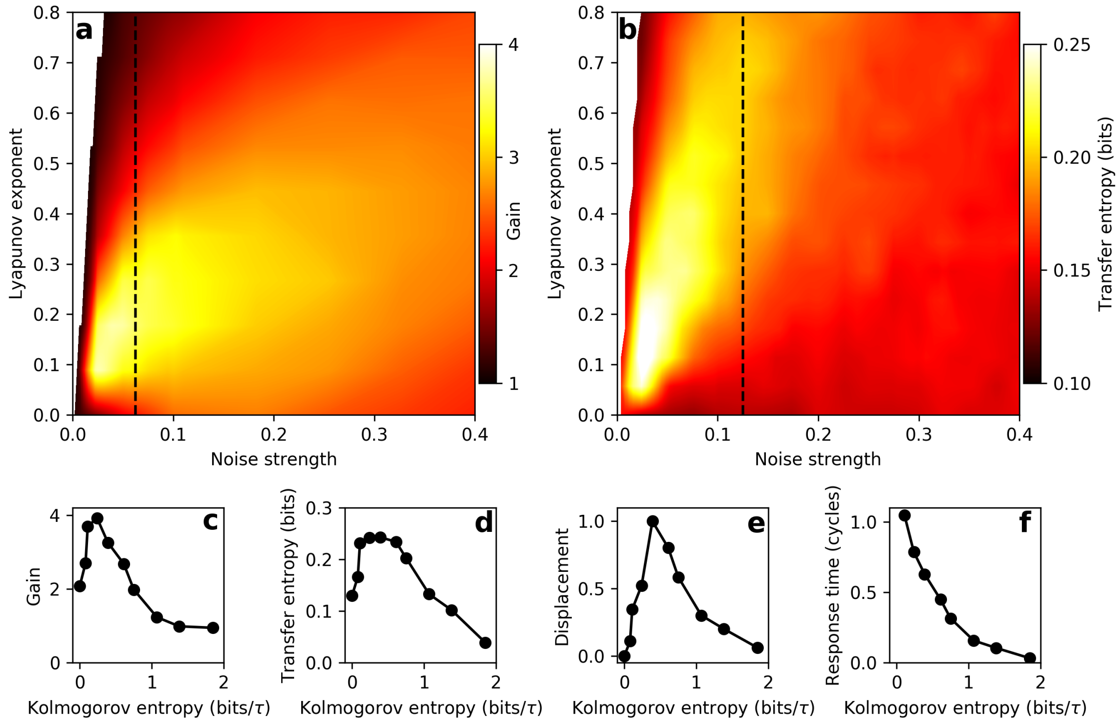

Figure 3.3: (**a**) Phase-locked amplitude gain for on-resonance, sinusoidal stimulus. (**b**) Transfer entropy from burst noise stimulus to response of the Hopf oscillator. For (a-b), β, ω_0, and D, were varied, resulting in a range of Lyapunov exponents. All other parameters were fixed ($\mu = \alpha = \Omega_0 = 1$). Color was generated by linearly interpolating a grid of 21 Lyapunov exponent values and 29 noise strengths. The stimulus amplitude was set to 0.5 for both panels. The vertical dashed lines indicate the points where the signal-to-noise ratio is 1, as defined by the ratio of the signal power to the noise power. (**c**) Phase-locked amplitude gain for on-resonance, sinusoidal stimulus. (**b**) Transfer entropy from burst noise stimulus to response of the Hopf oscillator. (**c**) Mean displacement in response to a step stimulus. (**d**) Response time to the step stimulus, calculated by taking the decay time of an exponential fit to the mean response. For (c-f), the Kolmogorov entropy was modulated by varying β and ω_0. All other parameters were fixed ($\mu = \alpha = \Omega_0 = 1$, $D = 0.05$).

feature persists at high levels of additive Gaussian white noise (signal-to-noise ratio < 1).

As an additional test of the system's response, we also measure the mean displacement induced by a step stimulus. We apply a step stimulus to the system and average over many different initial conditions and realizations of noise. We then compute the difference between the averaged curves before the onset of the step stimulus and after the system settles to the new steady state. Both the transfer entropy and the mean response amplitude show a local maximum as the degree of chaos is varied (Fig. 3.3d-e), consistent with the sensitivity observed in response to sinusoidal stimuli.

Finally, we measure the characteristic time of the exponential rise of the averaged response to the step-function forcing. We use this response time to characterize the temporal resolution of the system. The response time decreases with increasing levels of chaos (Fig. 3.3f). Increasing chaoticity therefore allows the system to exhibit a faster response to an external perturbation.

3.4 Experimental Results

We use two experimental parameters to modulate the degree of chaos exhibited by oscillatory hair cells *in vitro*. The first parameter varied is the calcium concentration of the endolymph solution, which has been shown to affect the dynamics of the adaptive mechanisms within the hair bundle [65]. Varying the calcium concentration alters the spontaneous oscillation profile [9], with higher concentrations resulting in more irregular dynamics (Fig. 3.4a,c). As expected, increasing the calcium concentration increases the degree of chaos (see Appendix). The second experimental parameter we vary is the viscosity of the endolymph solution. It has recently been shown that increasing the viscosity suprisingly increases the regularity of the spontaneous oscillations [66]. Once the viscosity is increased beyond about five times its natural value, the regularity of the spontaneous oscillations then decreases (Fig. 3.4b,d). We vary both of these parameters in our experiments in order to densely sample the parameter space of this chaotic oscillator.

While the variations described above yield visible differences in the regularity of the oscillations, rigorous mathematical tests are required to establish whether the active motility is chaotic or not. One reliable method for determining the presence of chaos in a system is provided by observing the type of transition it undergoes as it phase-locks to an external signal. If the external signal induces a torus-breakdown transition, this feature is an indicator of chaos. We hence constructed Poincaré maps of hair bundle oscillations driven by sinusoidal mechanical perturba-

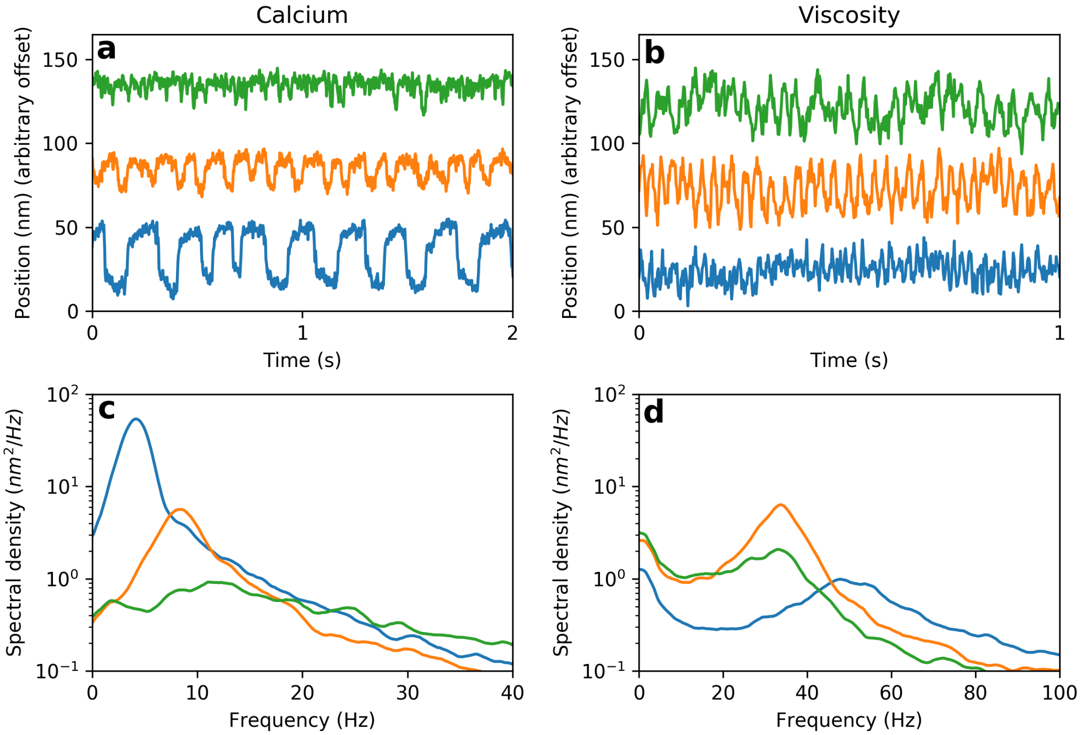

Figure 3.4: (**a**) Spontaneous oscillations of a hair bundle under various calcium concentrations of the endolymph. From bottom to top: 100 μM (low calcium), 250 μM (natural calcium), and 325 μM (high calcium). (**b**) Spontaneous oscillations of a hair bundle with various endolymph viscosities. From bottom to top: 0, 70, and 100 $\frac{mg}{ml}$ of Dextran 500. (**c**) Power spectral density of the traces in (a). (**d**) Power spectral density of the traces in (b).

tions of increasing amplitude [64], following methods developed earlier [47]. We determine the discrete time series, $[I_n]$, where each element reflects the time interval between the steepest rising flanks of consecutive hair bundle oscillations. We then plot the n^{th} versus the $(n+1)^{th}$ point of the series to obtain the Poincaré map (Fig. 3.5a-c). For low-amplitude, off-resonance stimuli, the points comprise a ring structure, revealing a cross-section of the underlying torus, and are indicative of quasiperiodic dynamics. Chaotic dynamics arise when this ring structure loses smoothness [41, 43, 45]. To check for smoothness of a Poincaré map, we determine the series of angles that each point makes with the abscissa and construct a circle map, $\theta_{n+1} = f(\theta_n)$ (Fig. 3.5d-f). When the surface of the torus is smooth, the map f is a monotonically increasing function. When chaos arises, the torus loses smoothness, and the map f loses monotonicity and may cease to be a function at all.

Under the natural conditions of the hair cell, we consistently find that off-resonance stimulus induces the torus-breakdown transition to/from chaos. Likewise, under high-calcium conditions, the circle map shows the absence of smoothness indicative of a chaotic system. However, when the hair cell is immersed in a low-calcium endolymph solution, the torus breakdown transition vanishes, and the circle map becomes a function (Fig. 3.5d). This finding suggests that spontaneous oscillations in low-calcium solution are non-chaotic, consistent with the observation of their regularity, reflected in a higher quality factor ($Q > 3$).

In addition to the Poincaré maps, we quantify the degree of chaos in the active dynamics of hair cells by estimating their Kolmogorov entropy, following techniques previously developed for the analysis of experimental records (see Methods) [38]. We note that this measure is useful for characterization of the degree of chaos in a system, once other methods have confirmed its presence. Any amount of measurement noise imposes a noise floor on the K-entropy, and hence, even the most regular spontaneous oscillations yield a small, positive K-entropy. An independent method must therefore be used to identify the crossover from stable to chaotic dynamics, and thus determine the effective noise floor on K-entropy. The circle maps described above indicate a non-chaotic state under low-calcium conditions, with the corresponding K-entropy that is small and positive, at ~ 0.5 bits/τ. We hence use this value of K-entropy as an experimental estimate of the noise floor.

To obtain different levels of chaos in bundle dynamics, we immersed the preparations in solutions of different combinations of calcium concentration and viscosity. At each experimental condition, we first record the innate oscillations of hair bundles, followed by measurements of their response to sinusoidal stimuli, presented at several fixed frequencies selected to yield both on- and off-resonance responses. Subsequently, we present burst noise, with square waves of various duration, selected from a random distribution (see Methods). Measurements of the response to sinusoidal stimuli allow us to extract the phase-locked amplitude gain as an estimate of the me-

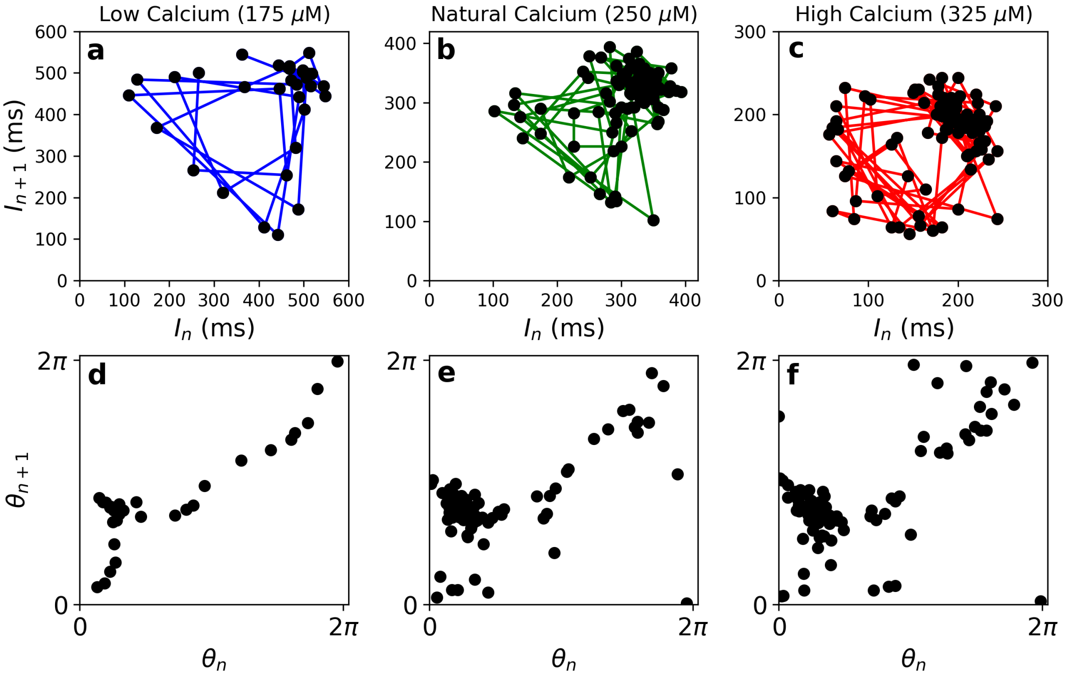

Figure 3.5: (**a-c**) Poincaré maps constructed from the time intervals between the steepest rising flanks of consecutive hair bundle oscillations under low ($175\mu M$), natural ($250\mu M$), and high ($325\mu M$) calcium concentrations of the endolymph, during presentation of off-resonance stimulus. (**d**) Circle map corresponding to the low-calcium conditions. The monotonic function suggests the absence of chaos. (**e-f**) Circle maps corresponding to the natural- and high-calcium conditions, respectively. The absence of a monotonic function indicates the presence of chaos. We use Spearman's rank correlation coefficient to test for monotonicity of the circle maps. Under low-, natural-, and high-calcium conditions, Spearman's coefficient is 0.60 ± 0.01, 0.14 ± 0.01, and 0.30 ± 0.02, respectively. Uncertainties represent 1 standard deviation from a sample of 100 bootstraps.

chanical sensitivity of the system. The burst noise yields the measure of the transfer entropy, as well as that of the mean displacement and response time of the bundle. The same methods are used to analyze the experimental records as those obtained from numerical simulations in the prior section.

Our findings consistently show optimal sensitivity and information gain in the weakly chaotic regime, as shown in Fig. 3.6 and in the Appendix. Upon increasing the degree of chaos, we find that the gain increases by at least 2-fold (even 5-fold for some cells). The information extracted from the burst noise stimulus also increases by more than 2-fold as the level of chaos is increased. Furthermore, increasing chaoticity yields a more rapid response time (Fig. 3.6d and Appendix), indicating a higher temporal resolution. Within the range of experimentally accessible levels of chaos, we see the response time reduce by about 5-fold (3-fold if measured in terms of the natural period of the hair bundle, see Appendix).

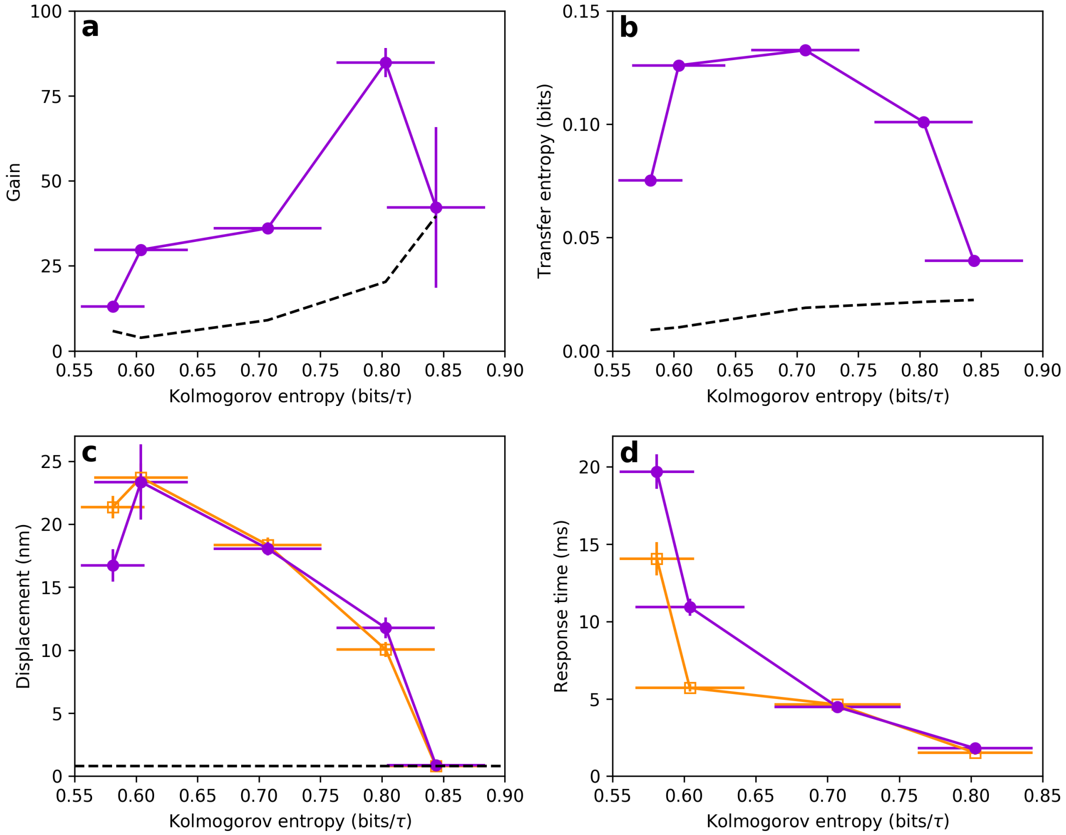

Figure 3.6: (**a**) Phase-locked amplitude gain for 2 pN sinusoidal stimulus, presented at the natural frequency. Data points and error bars on this measure represent the mean and standard deviation from 100 bootstraps. The noise floor (dashed curve) was calculated by treating a segment of the spontaneous oscillation recording as if a stimulus were present and calculating the gain. This curve represents the mean plus one standard deviation from 100 bootstraps. (**b**) Transfer entropy from burst noise stimulus to hair bundle response. Data points and error bars represent the mean and standard deviation obtained from 100 bootstraps. The noise floor (dashed curve) was determined by calculating the transfer entropy in the reverse direction (response to stimulus). This curve represents the mean plus one standard deviation from 100 bootstraps. (**c**) Average displacement induced on the hair bundle from the step stimulus, averaged over ~ 200 square waves. Data points and error bars represent the mean and standard deviation of the response plateau. Orange-open and purple-filled data points represent averages over steps in the positive (channel open) and negative (channel closed) directions, respectively. The noise floor is represented by the dashed line. (**d**) Response time to step stimulus, characterized by fitting the mean response to an exponential and extracting the decay time. Error bars represent the standard deviation of the residual associated with the exponential fit. All measurements were performed on the same cell.

3.5 Discussion

The auditory and vestibular systems have provided a powerful experimental testing ground for concepts in nonlinear dynamics [21, 23], nonequilibrium thermodynamics [56], and condensed matter theory [57]. Some of the long-standing open questions in this field pertain to how hair cells can reliably transform a sound wave into a neural spike train with such sensitivity, frequency selectivity, and temporal resolution. Most theoretical studies of hair cell detection have focused on the stable limit cycle regime or on the interface between a stable limit cycle and a stable fixed point. Using the simplest model of hair cell dynamics, we have identified a chaotic state that has greater sensitivity to both sinusoidal and step-function stimuli than either of these traditional regimes in the presence of noise. Further, we have shown that this chaotic regime extracts more information from its acoustic environment and achieves greater temporal resolution, all while maintaining robustness to additive noise.

Chaos is typically considered a harmful element to dynamical systems. For example, a chaotic heartbeat is an indicator of cardiac fibrillation [26, 27]. Chaos may also be responsible for the anti-reliability of neurons [61, 67]. However, in this chapter, we have demonstrated that chaos is beneficial to sensory detection by hair cells. The dynamic state of a chaotic system depends sensitively on its initial conditions, and hence a small perturbation can result in a drastic change in the subsequent dynamics. We speculate that evolution has exploited this feature of chaos to enable hair cells to achieve sensitivity to displacements in the Å regime. Furthermore, auditory detection relies on high temporal resolution, in order to enable accurate spatial localization of a sound. Our results, obtained both theoretically and experimentally, indicate that a chaotic system exhibits faster response times than one poised in the stable regime. This is again consistent with the general nature of chaotic systems, which show exponential divergence of trajectories in response to a perturbation. We propose that this regime provides an attractive alternative to proximity to the Hopf bifurcation, which achieves high sensitivity, but at the price of critical slowing down.

As most biological systems are nonlinear and contain many degrees of freedom, chaos is likely to be a ubiquitous feature of their dynamics. We speculate that many other systems in biology, beyond those currently known, may exhibit chaotic dynamics. In particular, sensory systems that are responsible for detection of external signals may have evolved to harness the power of these instabilities. In this chapter, we explored the effects of chaos on the sensitivity of an individual hair cell, and demonstrated that it enhances its responsiveness.

3.6 Methods

3.6.1 Analytic Approximation of the Lyapunov Exponent

We use a similar approach to a previous Lyapunov exponent approximation [61]. Simulations show that the divergence of neighboring trajectories occurs predominantly in the $\hat{\theta}$ direction. In the noiseless case, the $\hat{r}$ direction is stable, while the $\hat{\theta}$ direction is only marginally stable. Therefore, we seek an approximation of the diverging perturbation in $\hat{\theta}$. We look for an equation of the form $\frac{d\langle\Delta\theta\rangle}{dt} = \lambda\langle\Delta\theta\rangle$, where λ is the Lyapunov exponent. Making the change of variables $z(t) = r(t)e^{i\theta(t)}$, Eq. (3.1) becomes

$$\frac{dr}{dt} = \mu r - \alpha r^3 + \eta_x(t)\cos\theta + \eta_y(t)\sin\theta \tag{3.7}$$

and

$$\frac{d\theta}{dt} = \omega_0 - \beta r^2 + \frac{1}{r}(\eta_y(t)\cos\theta - \eta_x(t)\sin\theta), \tag{3.8}$$

where a nonzero β yields nonisochronic dynamics [68]. Now we express these two differential equations in terms of a small difference between two neighboring solutions $(r_1(t), \theta_1(t))$ and $(r_2(t), \theta_2(t))$. We define $\Delta r = r_2 - r_1$ and $\Delta\theta = \theta_2 - \theta_1$. Making this substitution yields

$$\dot{\Delta r} = \mu\Delta r - \alpha((r_1 + \Delta r)^3 - r_1^3) + 2\sin(\frac{\Delta\theta}{2})\eta_1(t), \tag{3.9}$$

where we have defined new noise terms:

$$\eta_1(t) = \cos(\frac{\theta_1+\theta_2}{2})\eta_y(t) - \sin(\frac{\theta_1+\theta_2}{2})\eta_x(t) \tag{3.10}$$

and

$$\eta_2(t) = \cos(\frac{\theta_1+\theta_2}{2})\eta_x(t) + \sin(\frac{\theta_1+\theta_2}{2})\eta_y(t), \tag{3.11}$$

which also have the properties $\langle\eta_1(t)\eta_1(t')\rangle = \langle\eta_2(t)\eta_2(t')\rangle = 2D\delta(t-t')$ and $\langle\eta_1(t)\eta_2(t')\rangle = 0$.

Since the Lyapunov exponent is defined only in the limit of infinitesimal deviations, we let $\frac{\Delta r}{r_1} << 1$, $\frac{\Delta r}{r_2} << 1$, and $\Delta\theta << 1$. Keeping only the the first-order terms, Eq. (3.9) becomes

$$\dot{\Delta r} \approx \mu\Delta r - 3\alpha r_1^2\Delta r + \Delta\theta\eta_1(t). \tag{3.12}$$

As the system spends the most time at the stable radius, we start one of the two solutions at this radius, $r_1 = r_0 = \sqrt{\frac{\mu}{\alpha}}$, and allow the second solution to be a perturbation from this radius, $r_2 = r_0 + \Delta r$. Making this substitution, Eq. (3.12) simplifies further:

$$\dot{\Delta r} \approx -2\mu\Delta r + \Delta\theta\eta_1(t). \tag{3.13}$$

Notice that the dynamics are stable to perturbations in r. However, as deviations in θ grow, so does the effective noise term, $\Delta\theta\eta_1(t)$, and trajectories will tend to spread farther away from the noiseless limit cycle radius. We now use Fokker-Planck theory to find the probability distribution, $P(\Delta r)$, of this stable potential. Inserting the drift and diffusion terms into the Fokker-Plank equation, we get

$$\frac{\partial P}{\partial t} = -\frac{\partial}{\partial\Delta r}(-2\mu\Delta r P) + D(\frac{\partial}{\partial\Delta r})^2((\Delta\theta)^2 P). \tag{3.14}$$

We seek the steady-state solution, $\frac{\partial P}{\partial t} = 0$.

$$2\mu\Delta r P + D\frac{\partial}{\partial\Delta r}((\Delta\theta)^2 P) = constant = 0. \tag{3.15}$$

The constant must be zero in order for $P(\Delta r = \infty) = 0$.

$$2\mu \Delta r P + D(\Delta\theta)^2 \frac{\partial P}{\partial \Delta r} + 2D(\Delta\theta) P \frac{\partial \Delta\theta}{\partial \Delta r} = 0. \tag{3.16}$$

We will assume that $P(\Delta\theta)$ reaches steady state quickly due to the stability of the limit cycle. If the dynamics in r can quickly stabilize upon variation in θ, we can ignore the third term and easily find the probability distribution;

$$\frac{\partial P}{\partial \Delta r} = -\frac{2\mu \Delta r}{D(\Delta\theta)^2} P \tag{3.17}$$

$$P(\Delta r) = C e^{-\frac{\mu \Delta r^2}{D(\Delta\theta)^2}}, \tag{3.18}$$

where $C = \sqrt{\frac{\mu}{\pi D}} \frac{1}{\Delta\theta}$ is a normalization constant. As expected, this distribution spreads out as we increase the noise strength or the angular deviation, $\Delta\theta$. We now treat the $\dot{\theta}$ equation:

$$\begin{aligned} \dot{\theta}_2 - \dot{\theta}_1 = -\beta(r_2^2 - r_1^2) + \eta_y(t)(\frac{\cos\theta_2}{r_2} - \frac{\cos\theta_1}{r_1}) \\ -\eta_x(t)(\frac{\sin\theta_2}{r_2} - \frac{\sin\theta_1}{r_1}). \end{aligned} \tag{3.19}$$

Lyapunov exponents are calculated by averaging divergences rates over all of the phase space or, equivalently, over all time. We therefore take the time average of Eq. (3.19) and only two terms survive:

$$\langle \dot{\Delta\theta} \rangle = -2r_1\beta \langle \Delta r \rangle - \beta \langle (\Delta r)^2 \rangle. \tag{3.20}$$

We evaluate these average values using $P(\Delta r)$:

$$\begin{aligned} \langle \dot{\Delta\theta} \rangle = -2r_1\beta \int_{-\infty}^{\infty} \Delta r P(\Delta r) d\Delta r \\ -\beta \int_{-\infty}^{\infty} (\Delta r)^2 P(\Delta r) d\Delta r \end{aligned} \tag{3.21}$$

$$\langle \dot{\Delta\theta} \rangle = -\beta \sqrt{\frac{\mu}{\pi D}} \frac{1}{\langle \Delta\theta \rangle} \int_{-\infty}^{\infty} (\Delta r)^2 e^{-\frac{\mu \Delta r^2}{D(\Delta\theta)^2}} d\Delta r \tag{3.22}$$

$$\langle \dot{\Delta\theta} \rangle = \frac{d}{dt} \langle \Delta\theta \rangle = \frac{-\beta D \langle \Delta\theta \rangle^2}{2\mu} \tag{3.23}$$

This equation has a semi-stable fixed point at $\langle \Delta\theta \rangle = 0$. In the presence of noise, this point is unstable. Linearizing near the fixed point, we find that the solution diverges exponentially with Lyapunov exponent,

$$\lambda = \frac{|\beta| D}{\mu}. \tag{3.24}$$

Using numerical simulations, we verify the validity of this approximation (see Appendix).

3.6.2 Transfer Entropy

The transfer entropy[55] from process J to process I is defined as

$$T_{J \to I} = \sum p(i_{n+1}, i_n^{(k)}, j_n^{(l)}) \log \frac{p(i_{n+1} \mid i_n^{(k)}, j_n^{(l)})}{p(i_{n+1} \mid i_n^{(k)})}, \tag{3.25}$$

where $i_n^{(k)} = (i_n, ..., i_{n-k+1})$ are the k most recent states of process I. Therefore, $p(i_{n+1} \mid i_n^{(k)}, j_n^{(l)})$ is the conditional probability of finding process I in state i_{n+1} at time $n+1$, given that the previous k states of process I were $i_n^{(k)}$ and given that the previous l states of process J were $j_n^{(l)}$. The summation is performed over the length of the time series, as well as over all accessible states of processes I and J. Given the history of process I, the transfer entropy $T_{J \to I}$ is a measure of how much one's ability to predict the future of process I is improved when one gains knowledge of the history of process J. If these processes are completely unrelated, then $T_{J \to I} = 0$. We discretize the recordings of hair bundle position into two bins, a natural choice due to the bimodal distribution in position of the hair bundle. Likewise, the bimodal burst noise stimulus is characterized by two states. The choice of k and l has little effect on our results, so we select $k = l = 5$.

3.6.3 Biological Preparation

Experiments were performed *in vitro* on hair cells of the American bullfrog (*Rana catesbeiana*) sacculus, an organ responsible for low-frequency air-borne and ground-borne vibrations. Sacculi were excised from the inner ear of the animal, and mounted in a two-compartment chamber with artificial perilymph and endolymph solutions [8]. Hair bundles were accessed after digestion and removal of the overlying otolithic membrane [11]. All protocols for animal care and euthanasia were approved by the UCLA Chancellor's Animal Research Committee in accordance with federal and state regulations.

3.6.4 Mechanical Stimulus

To deliver a stimulus to the hair bundles, we used glass capillaries that had been melted and stretched with a micropipette puller. These elastic probes were calibrated by observing their Brownian motion with a high-speed camera and applying the fluctuation dissipation theorem. Typical stiffness and drag coefficients of these probes were 50 – 150 $\mu N/m$ and 100 – 200 nNs/m, respectively. These elastic probes were treated with a charged polymer that improves adhesion to the hair bundle. Innate oscillations persisted after the attachment of a probe. The position of the probe base was controlled with a piezoelectric actuator. Stimulus waveforms were delivered to the actuator using LabVIEW.

3.6.5 Data Collection

Hair bundle motion was recorded with a high-speed camera at framerates of 500 Hz or 1 kHz. The records were analyzed in MATLAB, using a center-of-pixel-intensity technique to determine the position of the center of the hair bundle in each frame. Typical noise floors of this technique, combined with stochastic fluctuations of bundle position in the fluid, were 3 – 5 nm.

3.6.6 Stimulus Waveforms

Experiments were carried out as follows. First, we obtained a 60 second recording of the spontaneous oscillation, immediately followed by sinusoidal stimuli applied at several frequencies (20 stimulus cycles for each frequency). Then, the hair bundle was stimulated with burst noise (random telegraph noise), which was generated by randomly selecting time intervals between rising and falling flanks of the square wave. The intervals were selected such that the frequencies of the square waves ranged from 3 to 50 Hz, all with equal probability. This distribution spans the full frequency range of typical spontaneously oscillating hair bundles in the American Bullfrog sacculus [9] and is comparable to the 4-octave range of stimulus in our simulations. The wide range and flat probability distribution ensured that a change in sensitivity could not be due to a simple shift in the natural frequency of spontaneous oscillations. This stimulus lasted 20 seconds and included 300-400 full square waves. After this initial recording, the experimental parameters (calcium concentration and viscosity of the endolymph) were varied, and identical stimulus protocols were delivered again. Recordings were obtained under several different variations of calcium concentration and/or viscosity, so as to elicit different degrees of chaos from the same hair cell.

3.6.7 Data Analysis

The Kolmogorov entropy was calculated from the 60 second recording segment with no stimulus. We scaled these measurements to the time scale of each recording, τ, which was taken to be the time for the autocorrelation function of the spontaneous oscillations to cross zero. This ensured that a change in K-entropy was indeed a change in the predictability of the system and not simply a shift in the natural frequency. A consequence of this scaling was that it rendered the noise floor on K-entropy (~ 0.5 bits/τ) large with respect to the measurements ($0.5 - 1.3$ bits/τ). The response to sinusoidal stimulus and the spontaneous oscillations were used to calculate the gain. The response to the burst noise was used to calculate the transfer entropy, the mean displacement, and the response time, using the same techniques as described in the Theoretical Results. Bootstrap data sets were generated by adding fluctuations to the original data set based on the uncertainty in measuring hair bundle position. The position measurement uncertainty was quantified by recording a stationary object with the high-speed camera. To generate a bootstrap data set, each measurement of position in the original data set was given a random perturbation of magnitude based on the statistics of the fluctuations in position of the stationary object.

3.7 Appendix

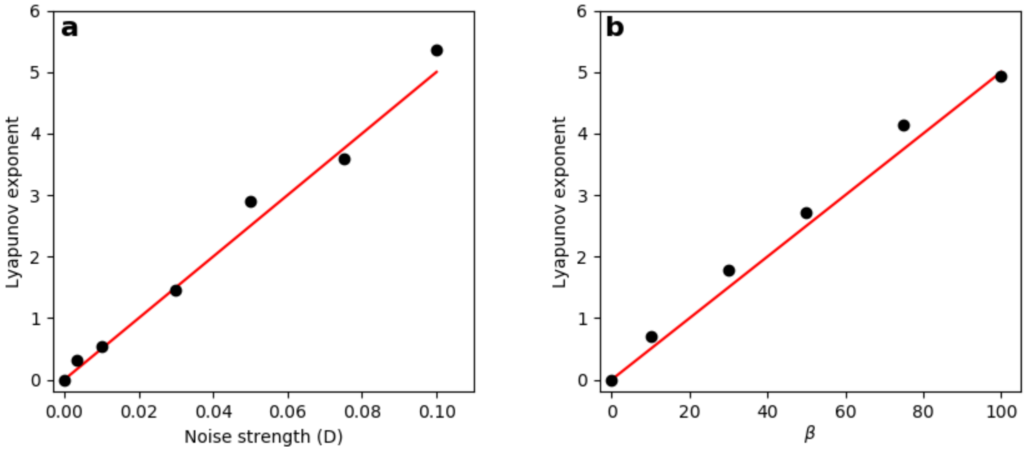

Figure 3.7: Comparison of the analytic calculation of the Lyapunov exponent (red line) to the numerical calculation (black points). (**a**) The noise strength is varied, while all other parameters are fixed ($\mu = \alpha = \Omega_0 = 1$, $\beta = 50$). (**b**) β is varied, while all other parameters are fixed ($\mu = \alpha = \Omega_0 = 1$, $D = 0.05$)

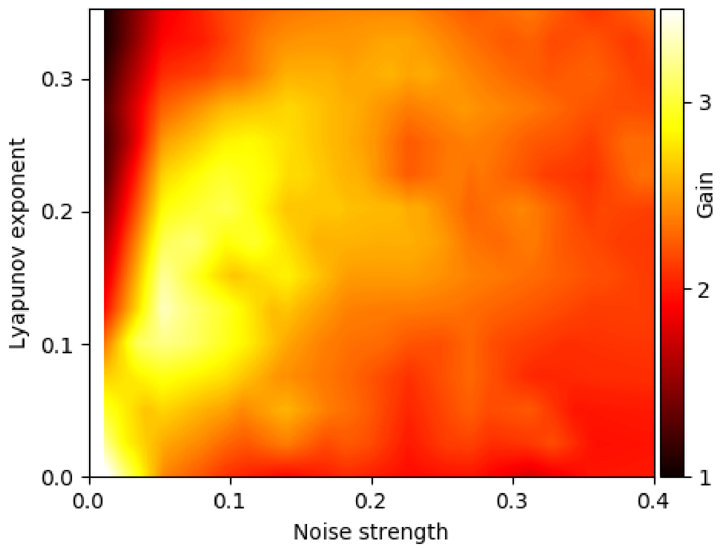

Figure 3.8: Phase-locked amplitude gain for above-resonance ($\omega_{stim} = 1.05\Omega_0$), sinusoidal stimulus as the noise strength and Lyapunov exponent are varied. Color was generated by linearly interpolating a grid of 10 Lyapunov exponent values and 10 noise strengths.

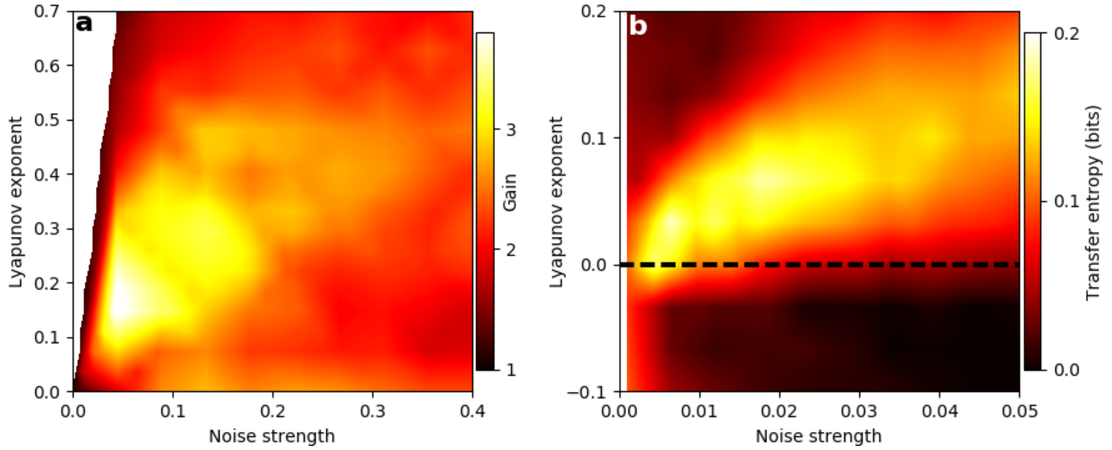

Figure 3.9: (**a**) Phase-locked amplitude gain for on-resonance, sinusoidal stimulus as the noise strength and Lyapunov exponent are varied. Color was generated by linearly interpolating a grid of 10 Lyapunov exponent values and 10 noise strengths. (**b**) Transfer entropy from burst noise stimulus to response of the Hopf oscillator as noise strength and Lyapunov exponent are varied. In the $\lambda < 0$ regime, the system is quiescent, and the Lyapunov exponent characterizes the stability of this fixed point. Color was generated by linearly interpolating a grid of 10 Lyapunov exponent values and 10 noise strengths. For both panels, the Lyapunov exponent was modulated by varying μ.

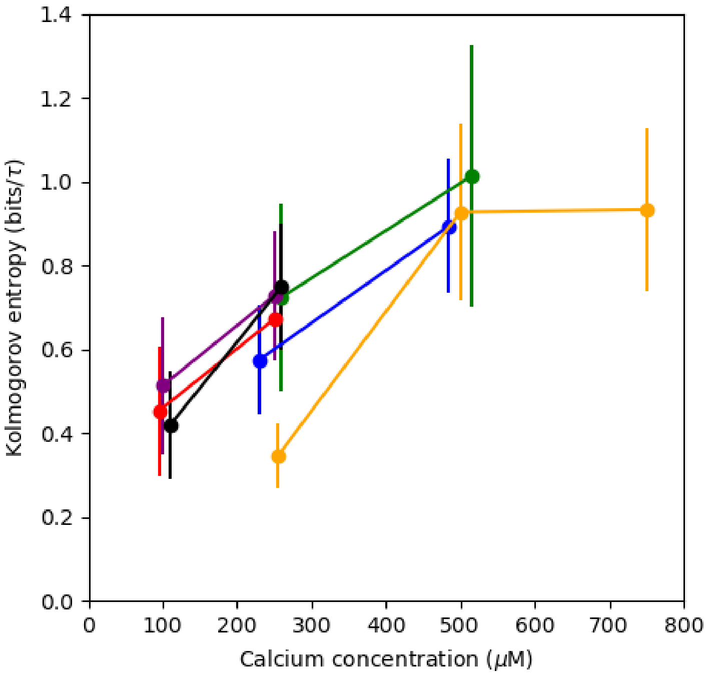

Figure 3.10: The dependence of Kolmogorov entropy on the endolymph calcium concentration. Each of the six colors corresponds to a different cell.

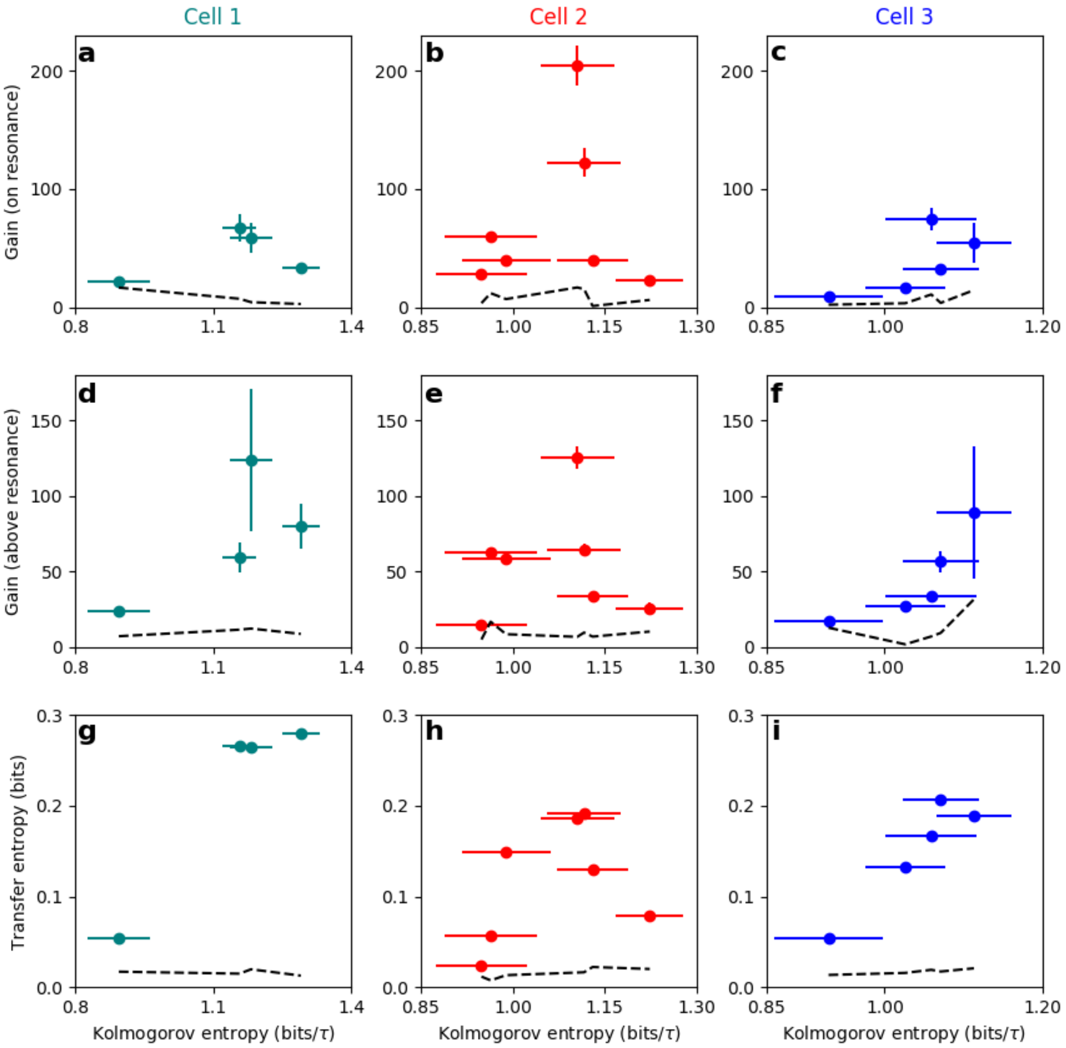

Figure 3.11: Phase-locked amplitude gain for 2 pN sinusoidal stimulus at the natural frequency (**a-c**) and above the natural frequency (**d-f**) for three additional cells. Data points and error bars on the gain represent the mean and standard deviation from 100 bootstraps. The noise floor (dashed curve) was calculated by treating a segment of the spontaneous oscillation recording as if a stimulus were present and calculating the gain. This curve represents the mean plus one standard deviation from 100 bootstraps. (**g-i**) Transfer entropy from burst noise stimulus to response. Data points and error bars represent the mean and standard deviation obtained from 100 bootstraps. The noise floor (dashed curve) was determined by calculating the transfer entropy in the reverse direction (response to stimulus). This curve represents the mean plus one standard deviation from 100 bootstraps.

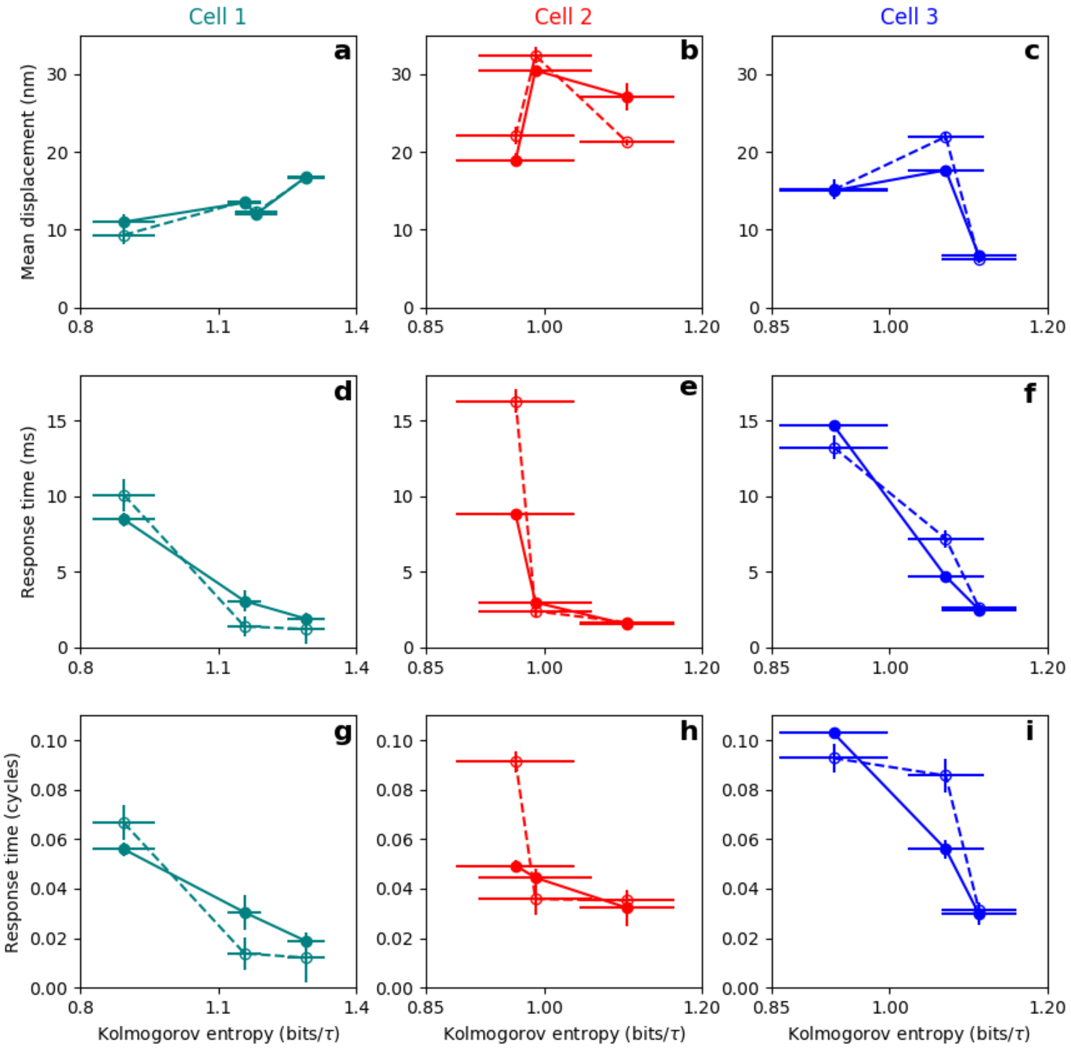

Figure 3.12: (**a-c**) Average displacement induced on the hair bundle from the step stimulus, averaged over ~ 200 square waves. Data points and error bars represent the mean and standard deviation of the response plateau. (**d-f**) Response time to step stimulus, characterized by fitting the mean response to an exponential and taking the decay time. Error bars represent the standard deviation of the residual associated with the exponential fit. (**g-i**) Response times from (d-f) scaled to the natural periods of oscillation for each recording. For all panels, open-dashed and closed-solid data points represent averages over steps in the positive (channel open) and negative (channel closed) directions, respectively.

CHAPTER 4

Nonisochronicity, Sensitivity, and Temporal Resolution

4.1 Introduction

In this chapter, we provide a theoretical treatment of the beneficial role of chaos in signal detection by the hair cells. We focus on noise-induced chaos, as biological sensory systems operate in thermal environments. The normal form equation for the Hopf bifurcation has been used to model many dynamical systems [69]. It was shown to capture a number of experimentally observed phenomena exhibited by the inner ear, including the sensitivity and frequency selectivity of hearing [21, 22]. Furthermore, it provides us with the simplest model that reproduces the main characteristics of hair bundle dynamics. We consider here the nonisochronous Hopf oscillator, for which the angular frequency depends on the radius [70]. By varying the parameters of the system, we modulate the degree of nonisochronicity, and thus the level of chaos that would be observed in the presence of noise [71]. We calculate the sensitivity to a constant-force stimulus analytically and find the nonisochronous system to be both more sensitive and faster to respond than the isochronous one.

Experiments performed on live hair cells have shown that the bundles exhibit a non-monotonic response to large, step-function stimuli, which resembles the ringing of an underdamped oscillator [8, 72]. This so-called "twitch" is observed only in living, active cells and is believed to be a manifestation of an internal active process, as a passive hair bundle exhibits an overdamped response. The phenomenon may play an important role in hearing, as it provides a possible mechanism by which the hair cell can amplify an incoming signal. In this chapter, we show that the Hopf oscillator can reproduce the twitch when the stimulus induces a saddle-node on invariant circle (SNIC) bifurcation resulting in a spiral-sink fixed point. Further, we find the parameter conditions that allow such behavior, providing us with a very simple model for this biological phenomenon.

Lastly, we explore the routes to chaos in the system, by finding the exact analytic expressions for the stroboscopic maps in the presence of a periodic delta-function stimulus. Using these maps, we find a period-doubling cascade to chaos upon increasing the forcing strength when the system is nonisochronous. Further, we find the same route to chaos upon increasing the degree of nonisochronicity, while keeping the forcing strength constant.

4.2 Theoretical Model

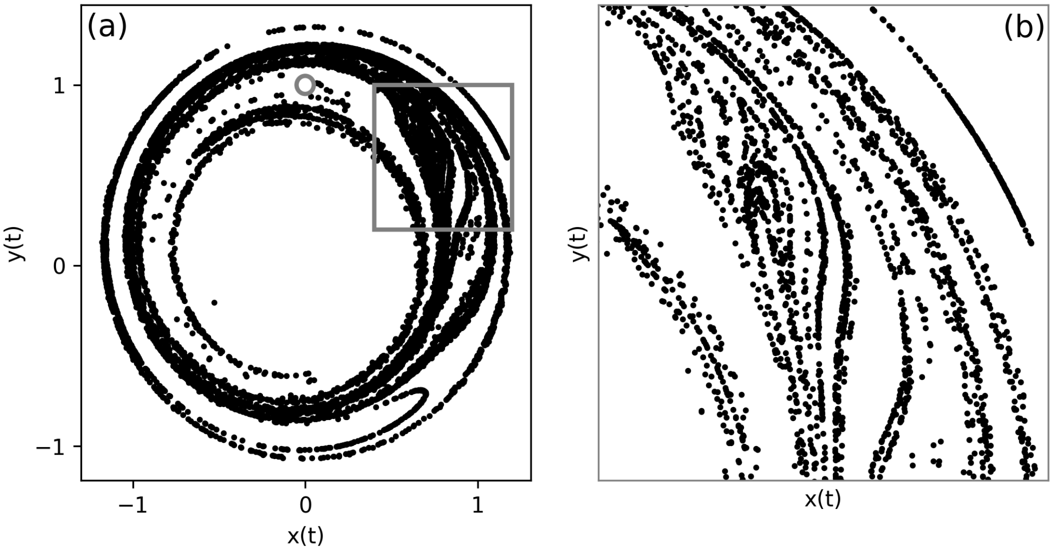

Figure 4.1: (a) The fractal structure of the Hopf oscillator with common noise: 10^4 slightly different initial conditions (confined to the grey circle) were evolved by 500 time steps under the same realizations of stochastic forces to produce the black points. (b) A zoomed-in version of the region in the grey box. $\mu = \alpha = \Omega_0 = 1$, $\beta = 100$, $D = 0.05$, where D is the noise strength and $\Omega_0 = \omega_0 - \frac{\beta\mu}{\alpha}$ is the natural frequency.

We use the normal-form equation for the Hopf bifurcation, including terms up to cubic order, and introduce additive forcing:

$$\frac{dz}{dt} = (\mu + i\omega_0)z - (\alpha + i\beta)|z|^2 z + F_z(t), \tag{4.1}$$

where $z(t) = x(t) + iy(t)$ and $F_z(t) = F_x(t) + iF_y(t)$. Here, $x(t)$ represents the bundle position, while $y(t)$ reflects internal parameters of the bundle and is not assigned a specific measurable quantity. μ is a constant that represents the control parameter. ω_0 characterizes the natural frequency when $\beta = 0$. α and β are constants that characterize the cubic nonlinearity of the system. Chaotic dynamics arise when this system is driven by Gaussian white noise: $F_z(t) = \eta_x(t) + i\eta_y(t)$, where $\langle \eta_x(t)\eta_x(t')\rangle = \langle \eta_y(t)\eta_y(t')\rangle = 2D\delta(t-t')$, and $\langle \eta_x(t)\eta_y(t')\rangle = 0$. In Fig. 4.1, each trajectory is given the same realization of noise, regardless of its position in phase space (common noise) [73]. We previously demonstrated that, under these conditions, the Lyapunov exponent can be approximated as [71]

$$\lambda \approx \frac{D|\beta|}{\mu}. \tag{4.2}$$

When $\beta \neq 0$, the oscillator is nonisochronous: the frequency is dependent on the amplitude of oscillations. We previously demonstrated that nonisochronous systems exhibit noise-induced chaos [71]. For simplicity, we study this instability in a noiseless system, while noting that in the presence of noise, the degree of chaos would be proportional to $|\beta|$.

Auditory and vestibular stimuli induce lateral deflections on the hair bundle, so we consider forces in the $\hat{x}$ direction, which coincides with the direction of autonomous oscillation. In polar coordinates, the model takes the form:

$$\frac{dr}{dt} = \mu r - \alpha r^3 + F_x(t)\cos\theta \tag{4.3}$$

$$\frac{d\theta}{dt} = \omega_0 - \beta r^2 - F_x(t)\frac{\sin\theta}{r}. \tag{4.4}$$

We observe that, in the absence of forcing, there is a stable limit cycle of radius $r_0 = \sqrt{\frac{\mu}{\alpha}}$ for

$\mu > 0$. Further, there is a nullcline in the phase at radius $r_{nc} = \sqrt{\frac{\omega_0}{\beta}}$. If the force causes the stable limit cycle to approach this radius, the angular frequency slows down, and the system approaches a SNIC bifurcation. We show that the forcing can perturb the shape of the limit cycle, causing an intersection between the stable limit cycle and r_{nc}. This SNIC bifurcation causes a pair of fixed points (one stable, one unstable) to appear on the limit cycle (see Appendix). When the system is poised in close proximity to this bifurcation, noise can most easily induce a chaotic response, and the system is very sensitive to external signals.

4.3 Response to a Constant-Force Stimulus

We consider forcing of the form $F_x(t) = f_0\Theta(t-t_0)$, where Θ is the Heaviside step function, and look at the response of a system in the oscillatory regime ($\mu > 0$). We assume that the forcing is weak compared to the stability of the limit cycle ($\frac{f_0}{\mu r_0} << 1$). We can therefore assume that the forcing acts as a small perturbation on the shape of the limit cycle and ignore the transient in r at the onset of the forcing. Looking for solutions near the limit cycle, we let $r(t) = r_0 + \delta r(t)$, where $r_0 = \sqrt{\frac{\mu}{\alpha}}$ is the limit cycle radius in the absence of forcing. Inserting this approximation into Eq. (4.3) and keeping only terms that are linear in δr yields

$$\frac{d}{dt}\delta r = -2\mu\delta r + f_0\Theta(t-t_0)\cos\theta, \tag{4.5}$$

which has a steady-state solution $\delta r = \frac{f_0\cos\theta}{2\mu}$ for $t > t_0$. Therefore, the first order perturbation to the shape of the limit cycle is given by:

$$r(t) = r_0 + \frac{f_0\cos\theta(t)}{2\mu}. \tag{4.6}$$

Inserting this solution into Eq. (4.4) and keeping only the first-order forcing terms, we find that

$$\frac{d\theta}{dt} = \Omega_0 - \frac{f_0\sin\theta}{r_0} - \frac{\beta r_0 f_0\cos\theta}{\mu}. \tag{4.7}$$

For clarity, we have defined $\Omega_0 = \omega_0 - \beta r_0^2$ to be the natural frequency. We integrate the equation to solve for $\theta(t)$:

$$\int_{t_0}^{t} dt' = \int_{\theta_0}^{\theta} \frac{d\theta'}{\Omega_0 - \frac{f_0 \sin\theta'}{r_0} - \frac{\beta r_0 f_0 \cos\theta'}{\mu}}, \tag{4.8}$$

where θ_0 is the phase of the oscillator at the onset of the step. Evaluating the integral yields

$$-\frac{1}{2}\gamma(t-t_0) = \tanh^{-1}(Q(\theta)) - \tanh^{-1}(Q(\theta_0)), \tag{4.9}$$

where

$$\gamma = \sqrt{\left(\frac{f_0}{r_0}\right)^2 + \left(\frac{\beta r_0 f_0}{\mu}\right)^2 - \Omega_0^2} \tag{4.10}$$

and

$$Q(\theta) = \frac{(\Omega_0 + \frac{\beta r_0 f_0}{\mu})\tan(\frac{\theta}{2}) - \frac{f_0}{r_0}}{\gamma}. \tag{4.11}$$

Inverting Eq. (4.9) yields

$$\theta(t) = 2\tan^{-1}\left(\frac{\gamma \tanh\Big(-\frac{1}{2}\gamma(t-t_0) + \tanh^{-1}(Q(\theta_0))\Big) + \frac{f_0}{r_0}}{\Omega_0 + \frac{\beta r_0 f_0}{\mu}}\right). \tag{4.12}$$

Using the identity $\tanh^{-1}(x) = \frac{1}{2}\log(1+x) - \frac{1}{2}\log(1-x)$, we can also write Eq. (4.9) in exponential form:

$$e^{-\gamma(t-t_0)} = \frac{(1+Q(\theta))(1-Q(\theta_0))}{(1-Q(\theta))(1+Q(\theta_0))}. \tag{4.13}$$

4.3.1 Response Amplitude

We use the mean displacement in x to characterize the response amplitude:

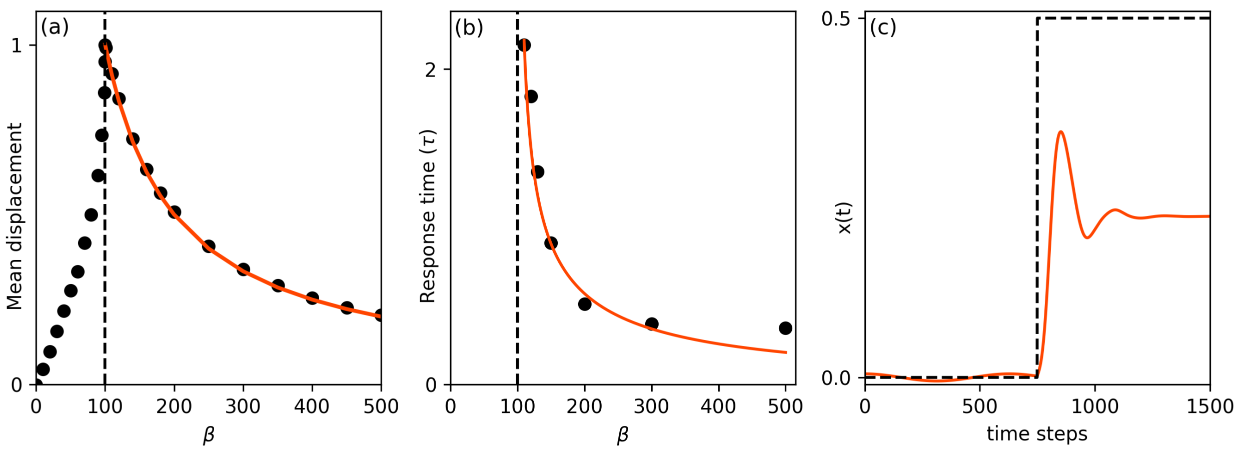

Figure 4.2: (a) Mean displacement of the Hopf oscillator in response to a constant-force stimulus found semi-analytically (black points) and fully analytically (solid curve). (b) Response time of the oscillator characterized by the exponential decay time in response to a step force. Black points represent the values found from numerical simulations, and the solid curve represents the analytic approximation. For (a-b), $\mu = \alpha = \Omega_0 = 1$ and $f_0 = 0.01$. The dashed line indicates the point where the forcing is able to induce a SNIC bifurcation. (c) An example of the twitch, a non-monotonic response (solid) to a step force (dashed), for $\mu = \alpha = \Omega_0 = 1$, $\beta = 50$, and $f_0 = 0.1$. The response curve represents the average over 200 different initial conditions, evenly separated in phase.

$$\langle \Delta x(t) \rangle = \langle r(t) \cos\theta(t) \rangle_{stim} - \langle r(t) \cos\theta(t) \rangle_0, \tag{4.14}$$

where the first and second terms on the right side are time averages in the presence and absence of the stimulus, respectively. The second term yields zero. Inserting Eq. (4.6), we obtain

$$\langle \Delta x(t) \rangle = r_0 \langle \cos\theta(t) \rangle_{stim} + \frac{f_0}{2\mu} \langle \cos^2\theta(t) \rangle_{stim}, \tag{4.15}$$

which can be solved semi-analytically by inserting Eq. (4.12) and taking the time average over a long time series (Fig. 4.2).

Depending on the choice of parameters, γ is either purely real or purely imaginary. Eq. (4.13) indicates that the solutions are oscillatory for imaginary γ and decay exponentially to a fixed point for real γ. In the latter case, we can find the mean displacement analytically. This fixed point corresponds to the intersection between the perturbed limit cycle, $r(t) = r_0 + \frac{f_0 \cos\theta}{2\mu}$, and the angular nullcline $r_{nc} = \sqrt{\frac{\omega_0}{\beta}}$. We set these two radii equal to each other and find that

$$\cos\theta = \frac{2\mu}{f_0}\left(\sqrt{\frac{\omega_0}{\beta}} - r_0\right). \tag{4.16}$$

We insert this solution into Eq. (4.15) and substitute in the natural frequency, $\Omega_0 = \omega_0 - \beta r_0^2$, to obtain:

$$\langle \Delta x(t) \rangle = \frac{2\mu r_0}{f_0}\left(\sqrt{\frac{\Omega_0}{\beta} + r_0^2} - r_0\right) + \frac{2\mu}{f_0}\left(\sqrt{\frac{\Omega_0}{\beta} + r_0^2} - r_0\right)^2. \tag{4.17}$$

This analytic curve is plotted in Fig. 4.2. Note that at a fixed natural frequency Ω_0 and in the limit of large β, the radius of the angular nullcline r_{nc} approaches the limit cycle radius. With these two circles close together, any small perturbation to the limit cycle can cause an intersection, resulting in a stable fixed point.

4.3.2 Temporal Resolution

We characterize the temporal resolution of the system by calculating the response time (decay time) to a step stimulus. Our results are limited to real γ, as this regime shows an exponential decay to a stable fixed point upon the application of a stimulus. For imaginary γ, the system would continue to oscillate in the presence of a step stimulus. We perform a Taylor series expansion of the right side of Eq. (4.13) in the vicinity of the stable fixed point (see Appendix):

$$\theta(t) \approx \frac{1 - Q(\theta_c)^2}{2Q'(\theta_c)}\left(e^{-\gamma(t-t_0)} - 1\right) + \theta_0, \tag{4.18}$$

where θ_c is the angle of the stable fixed point. The decay time of this solution is

$$\tau_{res} = \frac{1}{\gamma} = \frac{1}{\sqrt{(\frac{f_0}{r_0})^2 + (\frac{\beta r_0 f_0}{\mu})^2 - \Omega_0^2}}. \tag{4.19}$$

We fit exponential functions to the numerical simulations of the response and compare the values to the analytic form of τ_{res} in Fig. 4.2.

4.3.3 Non-monotonic response

In the regime of large β and/or strong forcing, the averaged response curve does not resemble an exponential decay. Rather, the response is non-monotonic and resembles the observed phenomenon known in hair bundle mechanics as "the twitch" [8, 72] (Fig. 4.2). In our simple model, the non-monotonic behavior is a result of a spiral sink forming after the step force induces a SNIC bifurcation. The trajectories spiraling to the fixed point give rise to the ringing behavior in $x(t)$. In this section, we find the conditions necessary for the Hopf oscillator to produce this phenomenon. We find the fixed point (R_c, θ_c) using Eqs. (4.3) and (4.4):

$$0 = \mu R_c - \alpha R_c^3 + f_0 \cos\theta_c \tag{4.20}$$

$$0 = \omega_0 - \beta R_c^2 - f_0 \frac{\sin\theta_c}{R_c}. \tag{4.21}$$

The Jacobian at the fixed point takes the form:

$$J = \begin{pmatrix} \mu - 3\alpha R_c^2 & -f_0 \sin\theta_c \\ -2\beta R_c + f_0 \frac{\sin\theta_c}{R_c^2} & -f_0 \frac{\cos\theta_c}{R_c} \end{pmatrix} \tag{4.22}$$

which can also be written as

$$J = \begin{pmatrix} \mu - 3\alpha R_c^2 & \beta R_c^3 - \omega_0 R_c \\ \frac{\omega_0}{R_c} - 3\beta R_c & \mu - \alpha R_c^2 \end{pmatrix} \tag{4.23}$$

by using Eqs. (4.20) and (4.21) to eliminate θ_c. A spiral sink is present if and only if the trace of J is less than zero, the determinant of J is greater than zero, and $4\det(J) - Tr(J)^2 > 0$ [29]. Since we are considering the limit cycle regime, we have $\mu > 0$. We will also use the condition that $R_c \geq r_0 = \sqrt{\frac{\mu}{\alpha}}$. Since this effect is most pronounced when β is large, we will assume that the second term in Eq. (4.4) is larger in magnitude than the first ($|\beta r_0^2| > |\omega_0|$). With these assumptions, the first two conditions are always satisfied:

$$Tr(J) = 2\mu - 4\alpha R_c^2 \leq 2\mu - 4\alpha r_0^2 = -2\mu < 0 \tag{4.24}$$

and

$$\begin{aligned} \det(J) &= \mu^2\left(3\left(\frac{R_c}{r_0}\right)^4 - 4\left(\frac{R_c}{r_0}\right)^2 + 1\right) \\ &+\omega_0^2\left(3\left(\frac{\beta R_c^2}{\omega_0}\right)^2 - 4\left(\frac{\beta R_c^2}{\omega_0}\right) + 1\right) > 0, \end{aligned} \tag{4.25}$$

since $\frac{R_c}{r_0} \geq 1$ and $\frac{\beta R_c^2}{\omega_0} \geq \frac{\beta r_0^2}{\omega_0} > 1$. The third and final condition is satisfied when

$$\beta > \frac{2\omega_0 + \sqrt{3\mu^2 + \omega_0^2}}{3r_0^2} \tag{4.26}$$

and ($|\beta| > \frac{|\alpha|}{\sqrt{3}}$) (see Appendix). Thus, we have found the conditions on the parameters of the Hopf oscillator such that it can reproduce the experimentally observed twitch.

4.4 Response to a Short-Pulse Stimulus

We now find the response amplitude to a brief, weak force of amplitude f_0 and duration T:

$$F_x(t) = f_0\Big(\Theta(t) - \Theta(t-T)\Big). \tag{4.27}$$

The solution during the force step was already found in Eqs. (4.6) and (4.12), provided that the initial conditions at the onset of the pulse are on the stable limit cycle. We use these equations to find the displacement induced in $x(t)$. The mean displacement is obtained by computing the

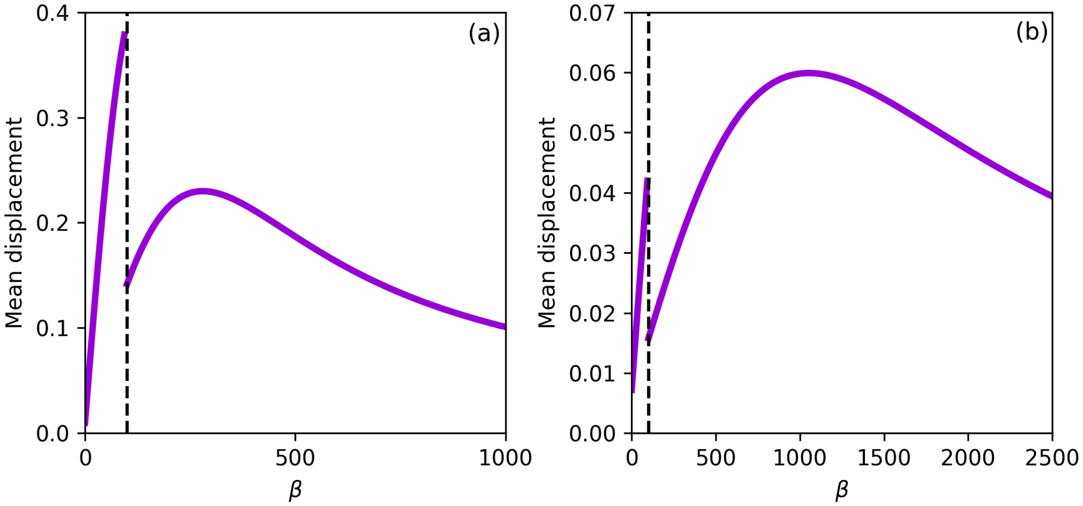

Figure 4.3: Mean displacement of the Hopf oscillator in response to a brief, constant-force stimulus. (a) and (b) represent the responses to a pulse of duration $\frac{1}{4}$ and $\frac{1}{16}$ of the natural period of oscillation, respectively. $\mu = \alpha = \Omega_0 = 1$, $f_0 = 0.01$, and the vertical dashed line represents the value of β at which the forcing is able to induce a SNIC bifurcation.

average of $(x(T) - x(0))$ over many different initial conditions. The mean displacement is used to quantify the responsiveness of the system.

In Fig. 4.3, we show that there is a local maximum in responsiveness at the SNIC bifurcation, as in the steady-state case. However, we observe an additional local maximum as β increases beyond the bifurcation point. Increasing β in this regime increases the speed at which the trajectories move across the circle to the fixed point. This increase is beneficial for the responsiveness of the system. However, the increase in β also moves the fixed point in the $-\hat{x}$ direction, thereby reducing the mean displacement in x (see Appendix). The competition between these two effects results in a local maximum. The location of this maximum is dependent on the pulse duration, which determines the time needed for the trajectories to reach the fixed point, starting from the initial conditions.

4.5 Effects of a Spike Train

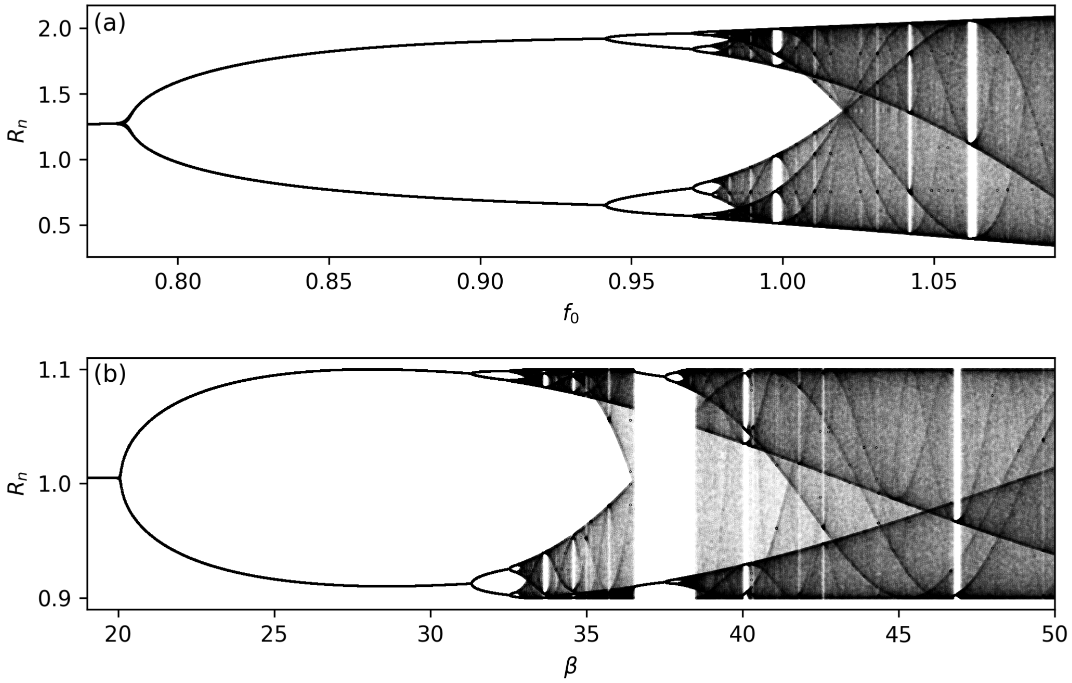

Figure 4.4: Bifurcation diagrams generated from the radial stroboscopic map at each impulse of the spike train. The interval between spikes was set to be the natural period of oscillations ($\tau = \frac{2\pi}{\Omega_0}$, $\mu = \alpha = \Omega_0 = 1$). (a) $\beta = 3$, while f_0 is varied. (b) $f_0 = 0.1$, while β is varied.

We now find the response to periodic, delta-function forcing. We construct the stroboscopic Poincaré maps analytically [74] and observe the transition to chaos. First, we find the analytic solution in the absence of forcing by integrating Eqs. (4.3) and (4.4) with $F_x(t) = 0$. The first can be solved using partial fraction decomposition:

$$\int_{t_i}^{t} dt' = \int_{r_i}^{r} \frac{dr'}{\mu r' - \alpha r'^3} = \int_{r_i}^{r} \Big(\frac{1}{\mu r'} - \frac{\alpha r'}{\mu(\alpha r'^2 - \mu)}\Big) dr', \tag{4.28}$$

which yields

$$r_{so}(t, r_i) = \sqrt{\frac{\mu}{\alpha - (\alpha - \frac{\mu}{r_i^2}) e^{-2\mu t}}}, \tag{4.29}$$

where we have set the initial time t_i to zero, and r_i is the radius at this time. We insert this solution into Eq. (4.4):

$$\frac{d\theta}{dt} = \omega_0 - \frac{\beta\mu}{\alpha - (\alpha - \frac{\mu}{r_i^2})e^{-2\mu t}}. \tag{4.30}$$

Integrating this equation yields

$$\theta_{so}(t, r_i, \theta_i) = \theta_i + \omega_0 t + \frac{\beta}{2\alpha} \log\left(\frac{\mu}{\alpha r_i^2(e^{2\mu t} - 1) + \mu}\right), \tag{4.31}$$

where θ_i is the phase at $t = 0$. We now include the spike-train stimulus:

$$F_x(t) = f_0 \sum_{n=1}^{n=\infty} \delta(t - n\tau). \tag{4.32}$$

The first impulse occurs at time $t = \tau$. Before this time ($t = \tau - \varepsilon$), the solution is simply $r(\tau - \varepsilon) = r_{so}(\tau - \varepsilon, r_i)$ and $\theta(\tau - \varepsilon) = \theta_{so}(\tau - \varepsilon, r_i, \theta_i)$. Projecting $F_x(\tau)$ onto polar coordinates, we find the solution at the time of the first impulse to be:

$$r(t = \tau) = R_1 = r_{so}(\tau, r_i) + f_0 \cos\left(\theta_{so}(\tau, r_i, \theta_i)\right) \tag{4.33}$$

$$\theta(t = \tau) = \Theta_1 = \theta_{so}(\tau, r_i, \theta_i) - \frac{f_0 \sin\left(\theta_{so}(\tau, r_i, \theta_i)\right)}{r_{so}(\tau, r_i)}. \tag{4.34}$$

The solution between the first and second impulses ($t = \tau + \varepsilon$) takes the form:

$$r(\tau + \varepsilon) = r_{so}(\varepsilon, R_1) \tag{4.35}$$

$$\theta(\tau + \varepsilon) = \theta_{so}(\varepsilon, R_1, \Theta_1), \tag{4.36}$$

where we treat the coordinates at the previous impulse as the initial conditions and reset the time. We now construct the stroboscopic Poincaré maps using this recursive method. We find the radius and phase at every spike, $R_n = r(t = n\tau)$ and $\Theta_n = \theta(t = n\tau)$, to be:

$$R_{n+1} = r_{so}(\tau, R_n) + f_0 \cos\big(\theta_{so}(\tau, R_n, \Theta_n)\big) \tag{4.37}$$

$$\Theta_{n+1} = \theta_{so}(\tau, R_n, \Theta_n) - \frac{f_0 \sin\big(\theta_{so}(\tau, R_n, \Theta_n)\big)}{r_{so}(\tau, R_n)}. \tag{4.38}$$

These stroboscopic maps are valid for both the oscillatory and quiescent regimes. We have made no assumptions on the choice of parameters or the strength of the forcing. Upon increasing either f_0 or β, we observe a period-doubling cascade to chaos (Fig. 4.4).

4.6 Discussion

In the last chapter, we demonstrated that nonisochronicity results in noise-induced chaos for even very weak levels of noise and any nonzero β. In this chapter, we demonstrated analytically that nonisochronicity is responsible for enhanced responsiveness to weak force steps, with the most responsive system being poised near the SNIC bifurcation. Further, we demonstrated that detection of a single constant-force pulse is highly rapid in a nonisochronous system. By varying β in the Hopf oscillator equation, we control the degree of nonisochronicity and study its impact on response characteristics. We show that the oscillator can detect very short pulses for a wide range of β, with the ideal value depending on the duration of the pulse. We also showed that the speed of the response, as measured by the exponential decay time to the constant force, increases with increasing β.

Although we considered the noiseless system in this work, upon including even a small amount of noise, β can be directly mapped onto the Lyapunov exponent. We previously demonstrated enhancement of sensitivity and temporal resolution with numerical models, where we varied the Lyapunov exponent directly [71]. The results of this numerical study are consistent with that of the present work. Nonisochronicity in a noiseless system hence directly correlates with the degree of chaos in the presence of noise.

Numerical models of hair cell dynamics typically require many variables to reproduce the experimentally observed twitch. Here, we demonstrated that this 2-dimensional model can capture the main features of this effect. This has, thus far, been the simplest model of hair cell dynamics able to produce this behavior. We have shown that the twitch can be explained through bifurcation theory: the stimulus yields a SNIC bifurcation with one of the fixed points being a spiral sink. Further, we found the parameter conditions required to see the effect.

Finally, we found the exact analytic expressions for the stroboscopic Poincaré maps in r and θ, when the oscillator is subjected to periodic, impulsive forcing. These maps are valid for any parameter regime and any degree of forcing. Using these stroboscopic maps, we observe a period-doubling cascade to chaos upon increasing either the forcing strength or β. The nature of this stimulus resembles that of efferent activity. In hair cell dynamics, efferent activity is believed to be the biological feedback responsible for modulating the sensitivity of the detector and may serve as a protective mechanism in preventing damage caused by acoustic trauma [75]. In this chapter, we demonstrated that an efferent-like stimulus can induce or modulate the degree of chaos, thus affecting the sensitivity of the system. Future work entails measuring the change in chaoticity and sensitivity caused by efferent activity.

Chaos is often considered an unfavorable element in dynamical systems, as it limits their predictability and regularity. However, chaos is likely present in a number of real-world systems, as they contain many degrees of freedom and exhibit nonlinearities. Here, we have shown analytically that the instabilities that give rise to chaotic dynamics are also responsible for enhanced sensitivity and temporal resolution in the Hopf oscillator, suggesting a beneficial role of chaos in the auditory and vestibular systems. We propose that chaos may play a role in signal detection in other noisy biological systems where timing and sensitivity are essential.

4.7 Appendix

4.7.1 SNIC Bifurcation

A saddle-node on invariant circle (SNIC) bifurcation occurs in this system when the stable limit cycle intersects with the angular nullcline. This gives rise to a fixed point at each of the two intersections, one of which is stable, while the other is unstable.

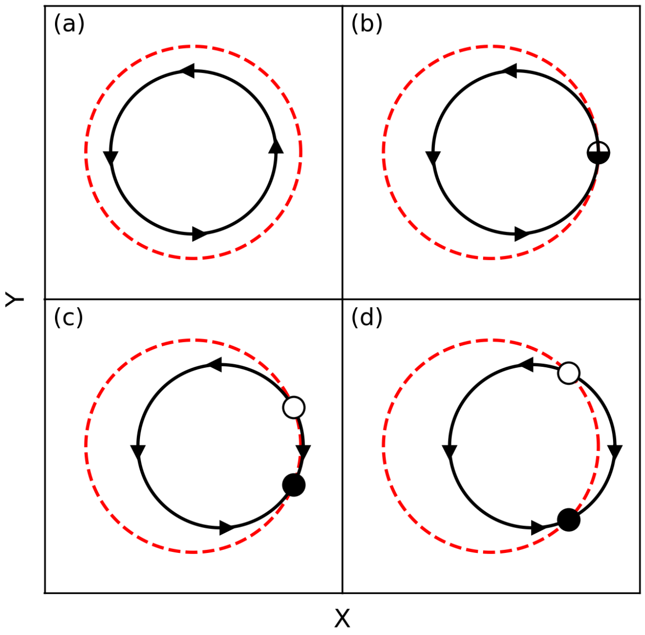

Figure 4.5: Illustration of the SNIC bifurcation. The solid and dashed curves represent the stable limit cycle and angular nullcline, respectively. Filled and empty points represent attracting and repelling fixed points, respectively. (a) Phase space diagram with no forcing. (b) A constant force in the $\hat{x}$ direction pushes the limit cycle into the angular nullcline, producing a semi-stable fixed point. (c) Upon increasing the force, the semi-stable fixed point splits into an attracting and a repelling fixed point. (d) Stronger forcing causes these two points to separate further.

4.7.2 Response Time

We perform a Taylor series expansion of the right side of Eq. (4.13) around θ_c, the angle of the stable fixed point. Keeping only first-order terms $(Q(\theta) \approx Q(\theta_c) + Q'(\theta_c)(\theta - \theta_c))$ yields

$$\begin{aligned} e^{-\gamma(t-t_0)} \approx & \frac{(1+Q(\theta_c)+Q'(\theta_c)(\theta-\theta_c))}{(1-Q(\theta_c)-Q'(\theta_c)(\theta-\theta_c))} \\ & \times \frac{(1-Q(\theta_c)-Q'(\theta_c)(\theta_0-\theta_c))}{(1+Q(\theta_c)+Q'(\theta_c)(\theta_0-\theta_c))}. \end{aligned} \tag{4.39}$$

Expanding and keeping only linear terms in $(\theta - \theta_c)$ and $(\theta_0 - \theta_c)$ results in

$$e^{-\gamma(t-t_0)} \approx 1 + \frac{2Q'(\theta_c)}{1-Q(\theta_c)^2}(\theta - \theta_0) \tag{4.40}$$

or

$$\theta(t) \approx \frac{1-Q(\theta_c)^2}{2Q'(\theta_c)}\left(e^{-\gamma(t-t_0)} - 1\right) + \theta_0. \tag{4.41}$$

This solution has response time

$$\tau_{res} = \frac{1}{\gamma} = \frac{1}{\sqrt{(\frac{f_0}{r_0})^2 + (\frac{\beta r_0 f_0}{\mu})^2 - \Omega_0^2}}. \tag{4.42}$$

4.7.3 Parameter Conditions for the Twitch

The third condition required for a spiral sink is $4\det(J) - Tr(J)^2 > 0$, yielding

$$\begin{aligned} & 4\mu^2\left(3\left(\frac{R_c}{r_0}\right)^4 - 4\left(\frac{R_c}{r_0}\right)^2 + 1\right) \\ & +4\omega_0^2\left(3\left(\frac{\beta R_c^2}{\omega_0}\right)^2 - 4\left(\frac{\beta R_c^2}{\omega_0}\right) + 1\right) \\ & -4\mu^2\left(4\left(\frac{R_c}{r_0}\right)^4 - 4\left(\frac{R_c}{r_0}\right)^2 + 1\right) > 0, \end{aligned} \tag{4.43}$$

which simplifies to

$$\omega_0^2\left(3\left(\frac{\beta R_c^2}{\omega_0}\right)^2-4\left(\frac{\beta R_c^2}{\omega_0}\right)+1\right)-\frac{\mu^2 R_c^4}{r_0^4}>0. \tag{4.44}$$

We can rewrite this condition as

$$(3\beta^2 r_0^4-\mu^2)\left(\frac{R_c}{r_0}\right)^4-4\beta\omega_0 r_0^2\left(\frac{R_c}{r_0}\right)^2+\omega_0^2>0, \tag{4.45}$$

which is always satisfied if the leading order term is greater than zero ($|\beta|>\frac{|\alpha|}{\sqrt{3}}$) and

$$3\beta^2 r_0^4-\mu^2-4\beta\omega_0 r_0^2+\omega_0^2>0, \tag{4.46}$$

since $\frac{R_c}{r_0}\geq 1$. Solving for β yields

$$\beta>\frac{2\omega_0+\sqrt{3\mu^2+\omega_0^2}}{3r_0^2}. \tag{4.47}$$

CHAPTER 5

Synchronization in Coupled Hair-Cell Networks

5.1 Introduction

In this chapter, we extend this study to systems of coupled active oscillators, which provides a model for the behavior of a full auditory or vestibular end organ. Specifically, we show that the chaotic regime causes Hopf oscillators to avoid amplitude death and instead synchronize with each other, despite large dispersion in the characteristic frequencies. We show that this synchronization is stable, as it persists for large system sizes, providing a plausible model for biological systems. Neither the amplitude nor the coherence of the spontaneous motion is compromised upon increasing the number of oscillators in the network. We test these theoretical predictions by experimental studies performed on *in vitro* preparations of excised epithelia, in which hair bundles were coupled using artificial membranes. We find consistent results in our experimental studies and theoretical predictions. Therefore, we propose that chaotic dynamics enhance the synchronization of oscillating hair bundles, causing the system to avoid the amplitude death state and instead produce spontaneous motion that could aid in signal detection, as well as result in the production of SOAEs.

Using the numerical model of this coupled system, we also demonstrate that this chaos-induced synchronization results in enhanced sensitivity and frequency selectivity to weak, external signals without compromising the speed of the response. This mechanism provides an attractive alternative to the dynamical regime in the immediate vicinity of the Hopf bifurcation, where the system sacrifices temporal resolution due to critical slowing down.

5.2 Numerical Model of Coupled Hair Bundle Dynamics

The dynamics of the j^{th} oscillator in the system are governed by the normal form equation for the supercritical Hopf bifurcation:

$$\frac{dz_j(t)}{dt} = (\mu + i\omega_j)z_j(t) - (\alpha + i\beta_j)|z_j(t)|^2 z_j(t) + k\Big(S(t) - x_j(t)\Big) + F_j(t), \tag{5.1}$$

where

$$z_j(t) = x_j(t) + iy_j(t). \tag{5.2}$$

Here, $x_j(t)$ represents the bundle position, while $y_j(t)$ reflects internal parameters of the bundle and is not assigned a specific measurable quantity. However, the existence of this hidden variable is essential to reproduce the experimentally observed dynamics. μ represents the control parameter of the oscillators, which determines the proximity to the Hopf bifurcation. The natural frequency at this bifurcation point is given by ω_j. For an individual, uncoupled oscillator, the limit-cycle radius is given by $r_0 = \sqrt{\frac{\mu}{\alpha}}$, and the limit-cycle frequency at finite radius is $\Omega_j = \omega_j - \beta_j r_0^2$. $F_j(t)$ represents a real-valued external forcing on the j^{th} oscillator.

All oscillators are coupled to the overlying artificial membrane with coupling stiffness, k. The position of the membrane, $S(t)$, is governed by the differential equation,

$$m\frac{d^2S(t)}{dt^2} + \lambda\frac{dS(t)}{dt} = \sum_{j=1}^{N} k\Big(x_j(t) - S(t)\Big), \tag{5.3}$$

where m and λ represent the mass and drag of the artificial membrane, respectively.

α and β_j characterize the nonlinear term of the system. In most prior studies, β_j was set to zero, rendering the oscillators isochronous. For such a system, the frequency is independent of the amplitude of oscillation. However, when $\beta_j \neq 0$, the system is nonisochronous, and the instantaneous frequency depends on the amplitude of the oscillations. This results in more complex behavior and causes the additive noise to induce chaotic dynamics in the individual oscillators [71].

Hair bundle dynamics occur at a Reynolds number much below one [76]. This allows us to ignore the inertial forces of the artificial membrane ($m = 0$). Since the drag of the membrane is fairly small in comparison to the drag of the hair bundles (see Appendix), we choose $\lambda = 0.1$. We set $\mu = \alpha = 1$, poising the system in the oscillatory regime. We use a significant coupling stiffness of $k = 2$, which can lead to synchronization of the oscillators. We vary β_j, Ω_j, and ω_j throughout this study and define the limit-cycle frequencies of the slowest and fastest oscillators in a system of N oscillators to be Ω_1 and Ω_N, respectively. The other oscillators have limit-cycle frequencies uniformly spaced between Ω_1 and Ω_N. All numerical simulations were performed using the fourth-order Runge-Kutta method with time steps of 10^{-3} unless otherwise stated.

5.3 Methods

5.3.1 Biological Preparation

Experiments were performed *in vitro* on hair cells of the American bullfrog (*Rana catesbeiana*) sacculus, an organ responsible for detecting low-frequency air-borne and ground-borne vibrations. Sacculi were excised from the inner ear of the animal, and mounted in a two-compartment chamber with artificial perilymph and endolymph solutions [8]. Hair bundles were accessed after digestion and removal of the overlying otolithic membrane [11]. All protocols for animal care and euthanasia were approved by the UCLA Chancellor's Animal Research Committee in accordance with federal and state regulations.

5.3.2 Artificial Membranes

Mica powder was added to a vial of artificial endolymph solution. This solution was thoroughly mixed and then filtered through several steel mesh gratings. These gratings served as band-pass filters to separate the mica flakes into several desired sizes. This process was expedited by using vacuum suction to pull the solution through the grating. The solution containing the artificial membranes was pipetted into the artificial endolymph solution, above the biological preparation. Many of the membranes would land in the desired orientation and adhere to hair bundles underneath. These hair bundles could then be imaged through the transparent artificial membranes.

5.3.3 Data Collection

Hair bundle motion was recorded with a high-speed camera at frame rates between 250 and 1000 frames per second. The records were analyzed in MATLAB using a center-of-pixel-intensity technique to determine the position of the center of the hair bundle in each frame. The motion was tracked along the direction of increasing stereovilli height. Typical noise floors of this technique, combined with stochastic fluctuations of the bundle position in the fluid, were 3–5 nm.

5.3.4 Cross-Correlation Coefficient

We characterize synchronization between spontaneously oscillating hair bundles using the cross-correlation coefficient

$$C\big(x_1(t), x_2(t)\big) = \frac{\langle \tilde{x}_1(t)\tilde{x}_2(t)\rangle}{\sigma_1 \sigma_2}, \tag{5.4}$$

where $\tilde{x}_1(t) = x_1(t) - \langle x_1(t)\rangle$ and $\tilde{x}_2(t) = x_2(t) - \langle x_2(t)\rangle$ represent the time traces of the motion, σ_1 and σ_2 represent their respective standard deviations, and the angled brackets denote the time average. $C = 1$ indicates perfectly correlated motion, while $C \approx 0$ is indicative of completely uncorrelated motion. We find the noise floor on this measure by calculating C between 1225 unique pairs of uncoupled hair bundles. The histogram of these cross-correlation coefficients has a standard deviation of approximately 0.02, with no points exceeding 0.1 (Fig. 5.6). To consider a pair of hair bundles to be coupled, we define our threshold to be $C \geq 0.1$, which is five standard deviations above the mean.

5.3.5 Correlation Time

We measure the coherence of the spontaneous oscillations, which can be characterized by integrating the squared autocorrelation function to compute the correlation time [77],

$$T_c\big(x(t)\big) = \int_0^\infty \left(\frac{\langle \tilde{x}(t)\tilde{x}(t+t')\rangle}{\sigma^2} \right)^2 dt'. \tag{5.5}$$

Due to the finite length of the experimental recordings, we truncate the integration at two mean periods of the spontaneous oscillations. We choose this duration, as the oscillations in the autocorrelation function have typically decayed after two full periods, and further integration would introduce unnecessary noise into the measure. Further, we scale this measure to the correlation time of a sine wave:

$$\tau_{cor} = \frac{T_c\big(x(t)\big)}{T_c\big(\sin(t)\big)}. \tag{5.6}$$

Therefore, perfectly sinusoidal motion yields $\tau_{cor} = 1$, while white Gaussian noise yields $\tau_{cor} \approx 0$.

5.4 Theoretical Results

A nonisochronous system can modify its oscillation frequency by adjusting its amplitude, thus allowing it to easily entrain to off-resonant frequencies. As a result, two coupled oscillators with large frequency dispersion can synchronize. Further, if the degree of nonisochronicity of the oscillators differs in correspondence with the dispersion of characteristic frequencies, synchronization can be greatly enhanced in systems of many oscillators. In Fig. 5.1c-e, we illustrate this effect by plotting the instantaneous angular frequency of uncoupled oscillators,

$$\frac{d\theta_j}{dt} = \omega_j - \beta_j r_j^2, \tag{5.7}$$

as a function of the radius of the oscillations, r_j. We plot these curves for four oscillators with fre-

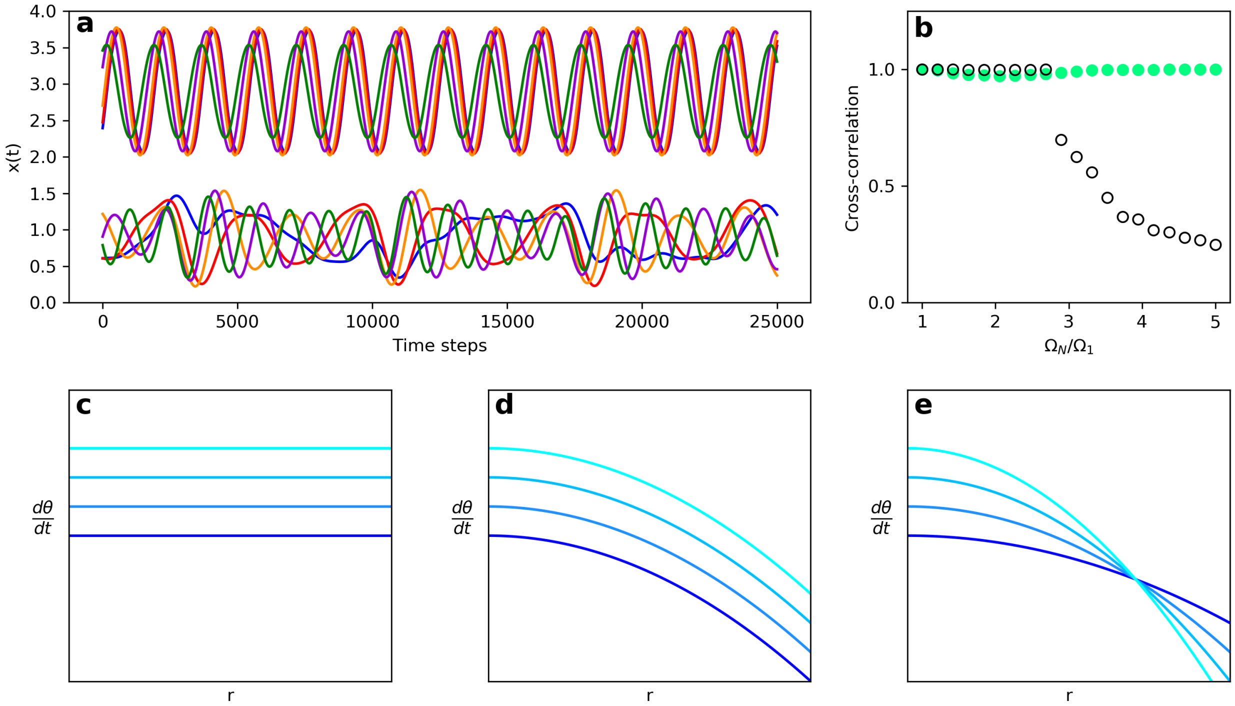

Figure 5.1: (**a**) Time traces of five coupled isochronous oscillators (bottom) and five coupled nonisochronous oscillators with β_j linearly spaced from 0 to 6 (top). (**b**) Average cross-correlation coefficient (Eq. 5.4) between all pairs of oscillators as a function of the frequency dispersion. This system consists of five oscillators in the isochronous (black-open) and nonisochronous (green-filled) cases. (**c-e**) Illustrations of the instantaneous frequencies (Eq. 5.7) of four oscillators as a function of the oscillation amplitude for the isochronous, nonisochronous with identical β_j, and nonisochronous with dispersion in β_j systems, respectively.

quency dispersion and show that the curves intersect when we include dispersion in β_j. Oscillators tend to meet at or near the intersection points, with synchronization enhanced even if the curves do not all intersect at the same point. We perform simulations of the numerical model and compare the isochronous case ($\beta_j = 0$) to the nonisochronous case, where β_j varies linearly between 0 and β_{max}, in accordance with ω_j. We set $\Omega_1 = 1$ and $\Omega_N = 2\sqrt{5} \approx 4.47$, choosing the values to be the similar to the frequency dispersion observed in the experiments. Sample traces of these simulations are plotted in Fig. 5.1a. We simultaneously modify β_j and ω_j to adjust the level of nonisochronicity, while keeping the limit-cycle frequencies, Ω_j, fixed.

We assess the stability of the synchronized state of five coupled Hopf oscillators by measuring

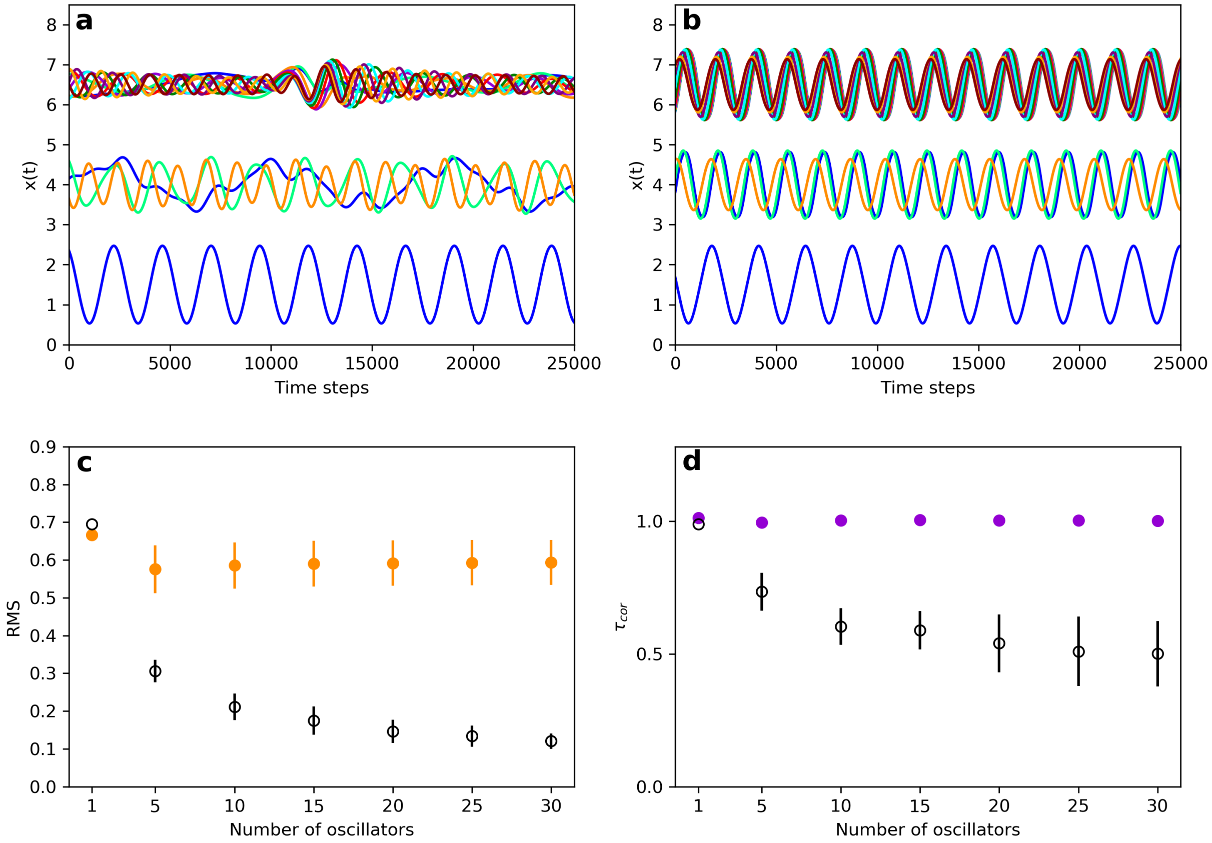

Figure 5.2: (**a-b**) Time traces of coupled oscillators for the isochronous and nonisochronous ($\beta_{max} = 6$) systems, respectively. The bottom, middle, and top sets of traces correspond to system sizes of $N = 1$, 3, and 10, respectively. (**c**) Root mean square (RMS) amplitude of the autonomous oscillations for a range of system sizes for the isochronous (black-open) and nonisochronous (orange-filled) cases. (**d**) Normalized correlation time (Eq. 5.6) for the isochronous (black-open) and nonisochronous (purple-filled) systems.

the average cross-correlation coefficient (Eq. 5.4) between all pairs of oscillators as a function of the frequency dispersion. In the isochronous case, synchronization becomes unstable for large frequency dispersion, pushing the system into the incoherent state. Upon an increase in the coupling strength, the isochronous system transitions into the amplitude death regime, and the system becomes quiescent. However, in the nonisochronous system, the synchronized state persists even with 5-fold frequency dispersion (Fig. 5.1b). Further, for the nonisochronous system, the stability of the synchronized state preserves the amplitude (root mean square) and coherence (Eq. 5.6) of the oscillators, rendering these measures independent of the system size (Fig. 5.2). This is in contrast to the isochronous system, for which the oscillation amplitude and coherence fall off with increasing network size.

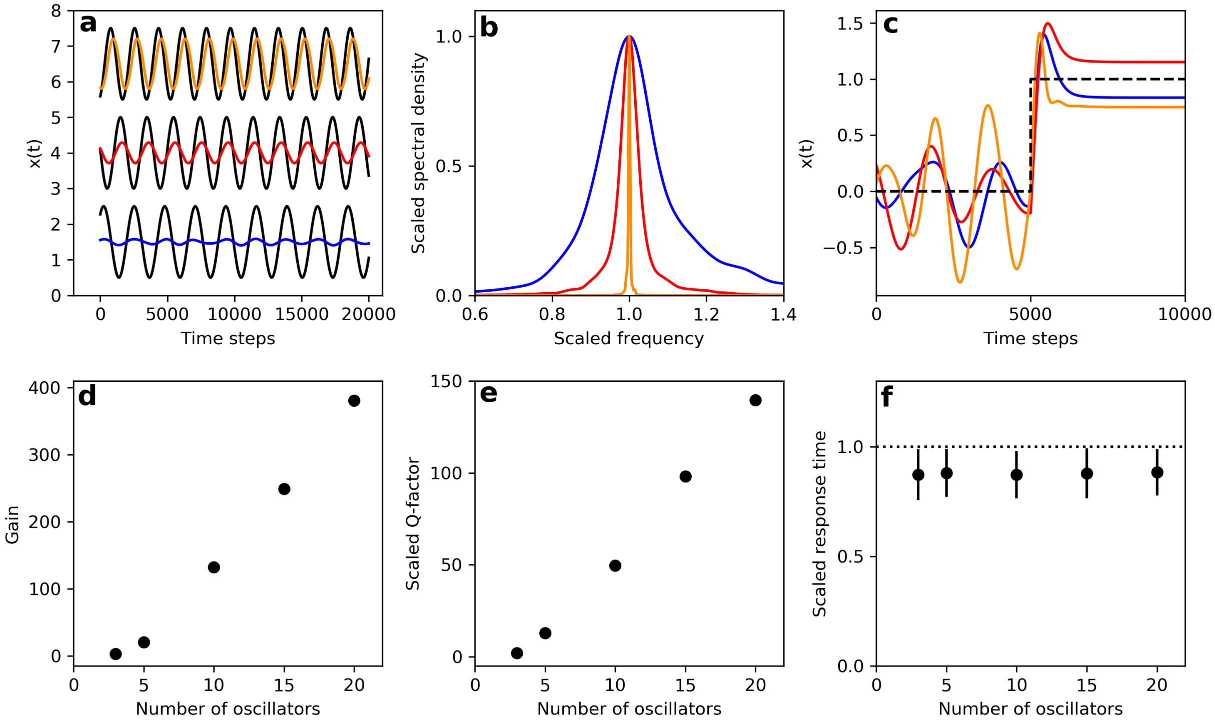

Figure 5.3: (**a**) Average response of the system to weak sinusoidal stimulus, illustrated by the black curves. The stimulus frequency was set to the median limit-cycle frequency of the network, $F(t) = 0.05\sin(\Omega_{\frac{N+1}{2}} t)$. The responses (blue, red, and orange curves) represent the average over all oscillators, over 20 presentations of the stimulus, each with random initial conditions. Bottom, middle, and top traces correspond to $\beta_{max} = 0$, 2, and 6, respectively. (**b**) Spectral curves in response to low-level white-noise stimulus. The curves get increasingly narrow for increasing β_{max}. (**c**) Average oscillator response to a step stimulus, as indicated by the black-dashed curve. Middle, top, and bottom plateau curves correspond to $\beta_{max} = 0$, 2, and 6, respectively. For (a-c), the system size was $N = 10$, and the blue, red, and orange curves represent $\beta_{max} = 0$, 2, and 6, respectively. (**d**) Spectral value of the nonisochronous ($\beta_{max} = 6$) system at the resonance frequency in response to weak white-noise stimulus, scaled to the corresponding spectral response of the isochronous system. (**e**) Quality factor of the system with $\beta_{max} = 6$ in response to weak white-noise stimulus, scaled to the quality factor of the isochronous system. (**f**) Response time of the nonisochronous ($\beta_{max} = 6$) system to a step stimulus, scaled to the response time of the isochronous system. Points and error bars represent the mean and the standard deviation over 100 presentations of the stimulus, each with random initial conditions.

We next determine the effects of nonisochronicity on the system's ability to detect weak signals.

We apply a weak Gaussian white noise stimulus, $F_j(t) = \eta_j(t)$, to each of the bundles. The noise terms of the oscillators are independent, with correlation function, $\langle \eta_j(t)\eta_j(t') \rangle = 2D\delta(t-t')$. We use a noise strength of $D = 0.01$ and integrate the stochastic differential equations using the second-order Runge-Kutta method. We then calculate the power spectrum of the response of the oscillator, $x_{(N+1)/2}$, which displays the median natural frequency. This method assumes the noise strength to be small enough to warrant consideration of only the linear response of the system.

The nonisochronous system exhibits much higher sensitivity and simultaneously provides a more narrow band-pass filter on the white-noise stimulus in comparison to the isochronous system (Fig. 5.3a-b). We quantify the increase in sensitivity by finding the maximum value in the power spectrum and normalizing it by the maximum value of the power spectrum of the isochronous system. This measure of gain indicates the factor by which nonisochronicity enhances the sensitivity of the system (Fig. 5.3d). Likewise, we calculate the quality factor of these peaks and normalize them by the quality factor of the isochronous system (Fig. 5.3e). We find that these measures of sensitivity and frequency selectivity increase with system size, consistent with prior theoretical studies [78]. For a system of 20 oscillators, the synchronization induced by nonisochronicity leads to a sensitivity increase of over 300-fold and a frequency selectivity increase of over 100-fold.

Lastly, we show that this large enhancement in the sensitivity and frequency selectivity of response does not come at the cost of reduced temporal resolution, in contrast with close proximity to a Hopf bifurcation. We provide an abrupt step-function stimulus to the system and average the responses of all of the oscillators. We then calculate the time it takes for the averaged response to settle to a constant value. As the plateau value fluctuates, we calculate the time required to settle within five standard deviations of the mean plateau value. We use this method to characterize the response time or temporal resolution of the system. We scale the response time of the nonisochronous system to that of the isochronous system and show that nonisochronicity not only does not degrade the temporal resolution, but in fact slightly enhances the rapidity of the response. Further, the speed of the system is independent of the system size (Fig. 5.3c, f).

5.5 Experimental Results

To experimentally test our theoretical predictions, we created hybrid systems, in which groups of biological hair cells were artificially coupled by mica flakes of various sizes (see Methods). The mica membranes were introduced into the solutions bathing the top surface of the biological epithelia, and allowed to adhere to the underlying hair bundles, thus providing coupling. As the thin sheets of mica are transparent, they allow for precise imaging of the motion of the underlying hair bundles (Fig. 5.4a-c). Hair bundles often exhibited synchronization, despite dispersion in their natural frequencies as large as 5-fold (Fig. 5.4d-g) [79], consistent with our theoretical predictions for nonisochronous oscillators. After recording the motion of the coupled hair bundles, the artificial membranes were removed through fluid exchange. This process did not result in any measurable damage of the preparation and the hair bundles continued to display robust spontaneous oscillations in all experiments.

We compare the amplitude (root mean square) of the hair bundles' spontaneous oscillations across different sizes of artificial membranes, and hence, different sizes of coupled networks (Fig. 5.5a, c). Due to the variation in heights of neighboring hair bundles, not every bundle under the membrane makes contact with it or becomes coupled. Therefore, we define a network by considering only those hair bundles that have motion correlated to another bundle in the network. We use a cross-correlation (Eq. 5.4) threshold of 0.1 to ensure that every bundle in the network is coupled. As an additional test, we repeat the calculation for a higher cross-correlation threshold of 0.5, ensuring that all of the oscillators in the network are fully synchronized (Fig. 5.7a). Figs. 5.4-5.5 show representative traces of fully synchronized hair bundles. For both choices of cross-correlation threshold, we consistently observe that the amplitude of the coupled motion is not reduced with increasing number of hair bundles. This finding is consistent with the behavior of nonisochronous oscillators and contrasts that of the isochronous system. In the isochronous case, coupling 10 oscillators together results in an amplitude reduction of more than 3-fold as compared to the individual, uncoupled oscillators (Fig. 5.2c). However, in the nonisochronous case, the

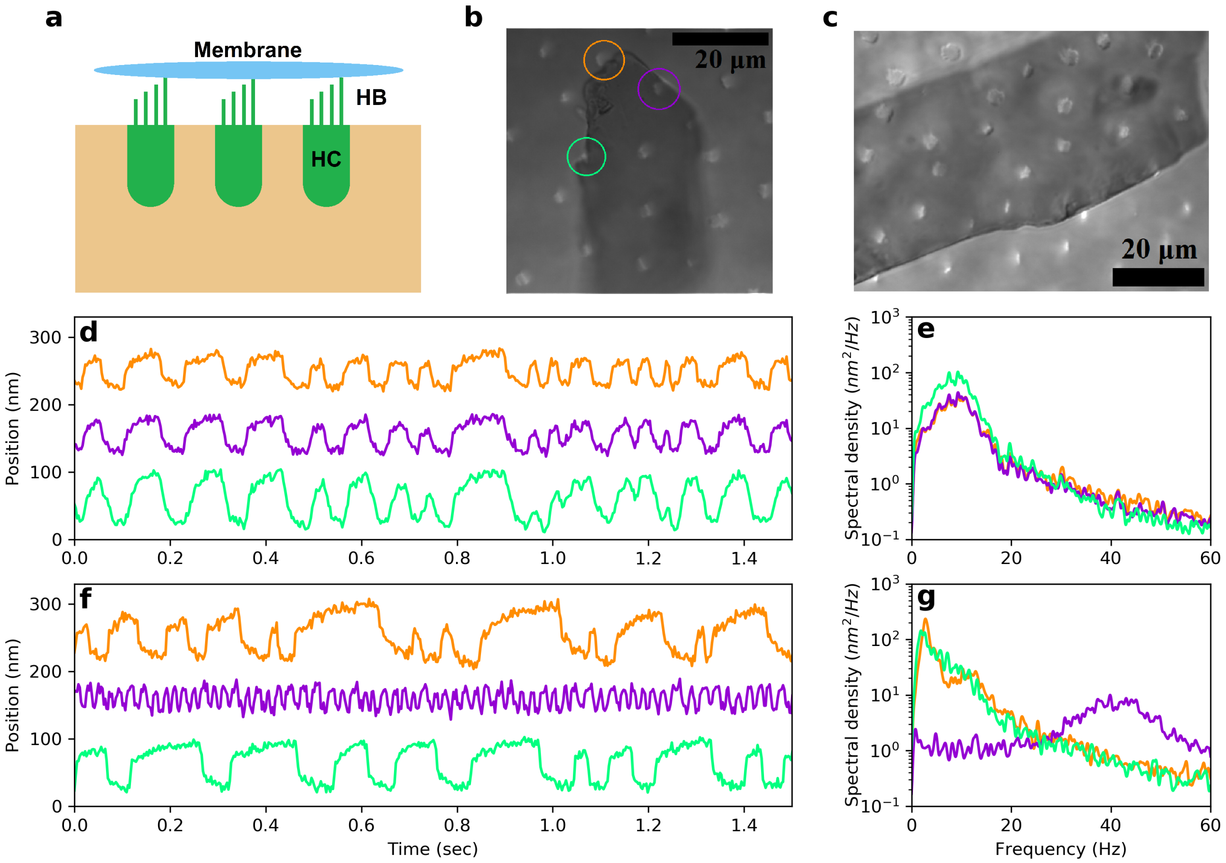

Figure 5.4: (**a**) Illustration of the experimental system from a side view, displaying the hair cells (HC), hair bundles (HB), and an artificial membrane. (**b-c**) Top-down images of biological preparations. The hair bundles appear as white dots, and the shadow cast by the transparent artificial membrane can be seen in the center of the images. (**d-e**) Time traces and power spectra of 3 spontaneously oscillating hair bundles coupled by an artificial membrane. These bundles are circled in (b) with colors corresponding to their time traces. The top, middle, and bottom traces correspond to the topmost, leftmost, and bottommost circles in (b). (**f-g**) Time traces and power spectra of the 3 hair bundles in (d-e) after removal of the artificial membrane.

amplitude remains constant across all system sizes.

We also compare the coherence (Eq. 5.6) of hair bundle oscillations across network sizes of all coupled oscillators (Fig. 5.5b, d) and of just those displaying synchronization (Fig. 5.7b). Consistent with the theoretical predictions for coupled nonisochronous oscillators, the coherence does not fall off upon increasing the number of oscillators in the network. In contrast, the coherence of the isochronous system reduces by nearly 2-fold for a system of 10 oscillators as compared to

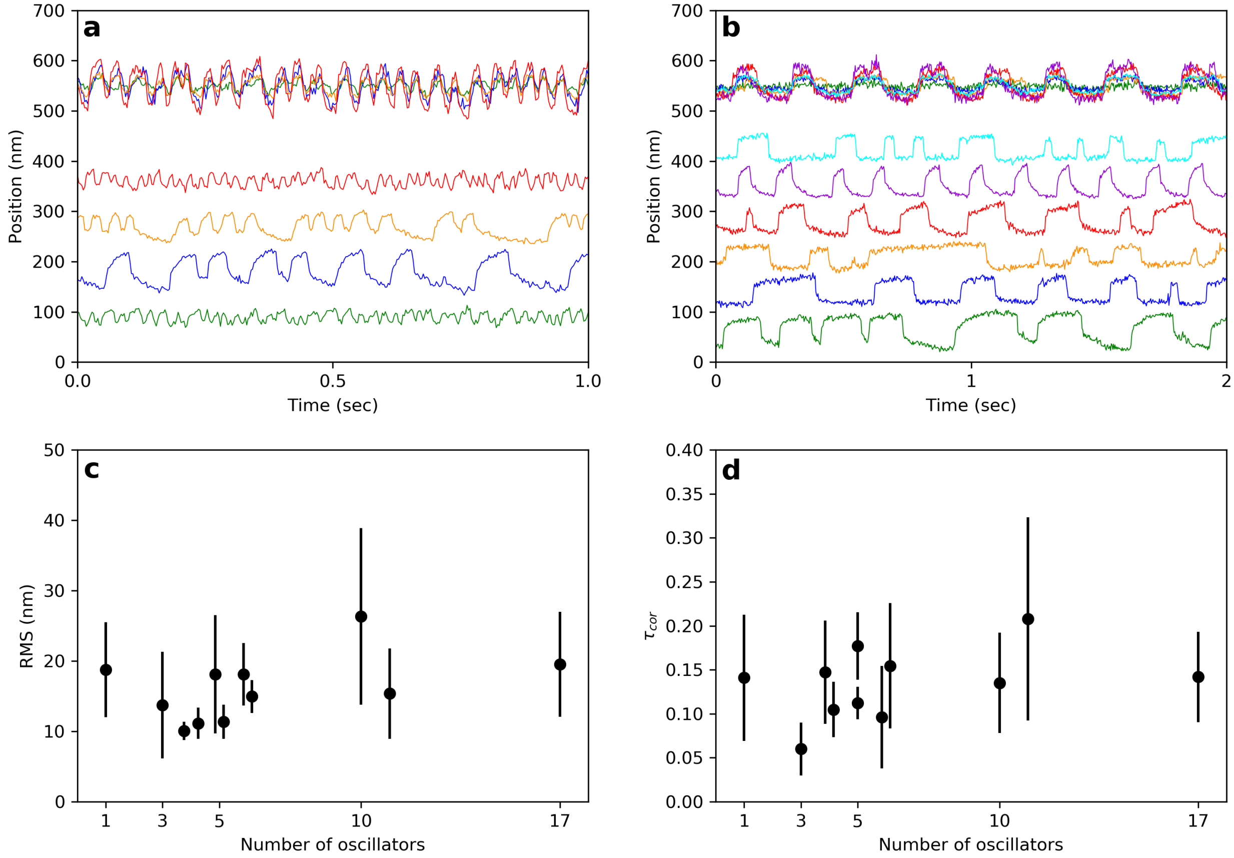

Figure 5.5: (**a-b**) Overlaid traces of coupled hair bundles (top) for system sizes of $N = 4$ and $N = 6$, respectively. Below the overlaid traces are the traces of the individual hair bundles obtained in the absence of coupling. (**c-d**) RMS amplitude and the normalized correlation time of spontaneous oscillations of coupled hair bundles, obtained for various system sizes. Each hair bundle had a cross-correlation coefficient of at least 0.1 with other bundles in the network. For both panels, points and error bars represent, respectively, the mean and the standard deviation of the coupled oscillators in the system. For systems with $N > 1$, each data point represents a separate group of coupled hair bundles. The points and error bars at $N = 1$ represent the collective mean and standard deviation across all 10 groups of hair bundles in the absence of coupling. These 10 groups of hair bundles were obtained from four sacculi from four different frogs.

the individual, uncoupled oscillators.

5.6 Discussion

Auditory and vestibular systems have provided an experimental testing ground for concepts in nonequilibrium thermodynamics [56], condensed matter theory [57], and nonlinear dynamics [21]. How active hair cells exhibit notable performance as signal detectors, displaying sensitivity of response, frequency selectivity, and high temporal resolution, all within a noisy fluid environment, is a long-standing open question in this area of study. Further, auditory organs tend to contain overlying structures that impose a strong degree of coupling between individual hair cells, which in turn exhibit dispersion of the characteristic frequencies. It has not been established which role the presence of both strong coupling and significant frequency dispersion play in achieving the detection characteristics, or how the system avoids amplitude death to form clusters of synchronized oscillators necessary for generating SOAEs.

Simulations of our numerical model of coupled hair bundles indicate that the nonisochronicity of the oscillators, which results in chaotic dynamics, is responsible for this robust synchronization. The synchronization yields great enhancement of the system's sensitivity and frequency selectivity to weak external signals. Unlike proximity to the Hopf bifurcation, this enhancement does not come at the cost of reduced temporal resolution. Further, this synchronization persists for large numbers of oscillators and despite large frequency dispersion. Neither the amplitude nor the coherence of the oscillations are reduced upon increasing the number of oscillators. These results are consistent with the remarkable signal-detection attributes of the auditory system and the experimental observations of sharp spectral peaks in the SOAE recordings.

The results from our experimental recordings of coupled hair bundles are consistent with those of the numerical model. By coupling various numbers of hair cells with artificial membranes, we find that hair bundles with differences in characteristic frequencies as large as 5-fold still routinely synchronize. Further, the amplitude and coherence of the spontaneous oscillations are both independent of the number of hair bundles in the network. These results can be reproduced by the numerical model only when the oscillators are chaotic ($\beta_j \neq 0$). This suggests that the instabilities that give rise to chaotic dynamics of the individual hair bundles enhance the synchronization and the signal detection of the coupled system.

The coupling strength of the networks of hair bundles in our experiments is likely strong, as it results in synchronization between bundles with vastly different characteristic frequencies. However, frequency dispersion, coupling strength, and topology of the coupling vary greatly across species and sensory organs [6]. The mammalian cochlea, for example, has a tonotopic organization of the hair cells and has a compliant overlying connecting structure, leading to smaller domains of coupling [80]. Therefore, cochlear hair cells would likely not synchronize over a frequency range as large as that observed in our experiments. However, our numerical model suggests that the benefits of synchronization grow rapidly with the number of oscillators (Fig. 5.3d-e). Hence, even if synchronization is limited to small groups of hair bundles, and over narrow ranges of characteristic frequencies, we expect the improvement in signal detection to be substantial.

Stochastic noise often limits signal detection. However, it has been shown that noise can also enhance the ability of sensory systems, including hair cells, to detect weak signals, through a phenomenon called stochastic resonance [81]. Similarly, low-dimensional chaos is often considered a harmful element in dynamical systems and something to be avoided. For example, a chaotic heartbeat is an indicator of cardiac fibrillation [26]. However, it has also been established that chaotic oscillators can easily synchronize with each other or entrain to an external signal [82, 62], as instabilities that give rise to chaotic dynamics can make the oscillators more adaptable to modifications in their autonomous motion. Since biological systems tend to have many degrees of freedom and contain nonlinearities, chaos may be a ubiquitous element in their dynamics. We speculate that chaos may be important in other biological systems where timing, sensitivity, and synchronization are desired, especially sensory systems responsible for detection of external signals.

5.7 Appendix

5.7.1 Approximation of Artificial Membrane Drag

We approximate the artificial membranes as infinitely thin circular disks. Due to the low Reynolds number of hair bundle dynamics, we assume the system obeys Stokes' law. The Stokes' drag of an infinitely thin circular disk moving edgewise through an infinite fluid is given by

$$\lambda_s = \frac{16\eta d}{3}, \tag{5.8}$$

where η is the dynamic viscosity of the fluid and d is the diameter of the disk [83]. We use the viscosity of water, $\eta \approx 10^{-3}$ Pa·s, and our approximate experimental range of membrane diameters (20-50 μm). The diameters of the membranes are significantly larger than their thicknesses ($<$ 1 μm), so we consider the infinitely-thin disk to be a reasonable approximation. Further, the boundary of the fluid is $\approx$ 1 cm away from the structures of interest, much farther than the length scale of the membranes, so the assumption of an infinite fluid is reasonable.

We, therefore, approximate the drag coefficients of the artificial membranes to be $\lambda_s \approx$ 100-250 nN·s·m^{-1}. We compare this value to the drag coefficient of individual free-standing hair bundles. It has previously been shown that most of the drag contribution of hair bundles comes from the channel-gating friction [84]. The lower bound on the total drag coefficient of an individual free-standing hair bundle was estimated to be $\lambda_0 = 425 \pm 70$ nN·s·m^{-1}. Therefore, in or numerical simulations, we use a small value for the membrane drag ($\lambda = 0.1$), as it contributes only minimally to the drag of the entire coupled system.

5.7.2 Cross-Correlation Coefficient Noise Floor

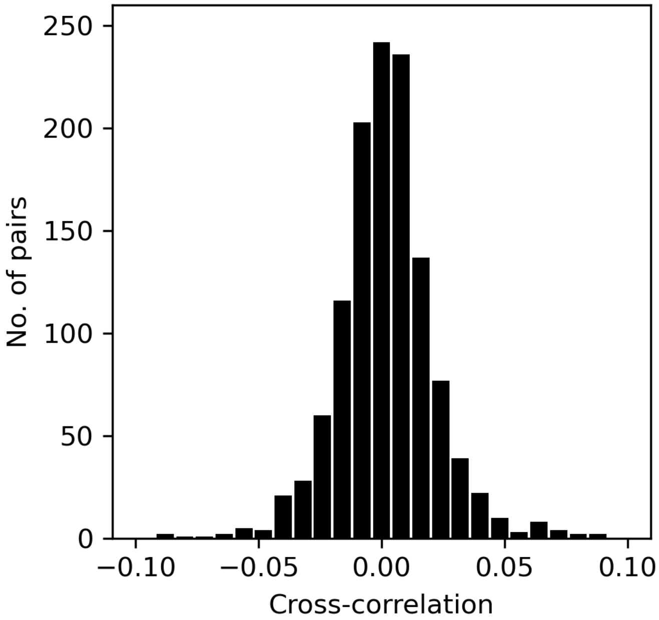

Figure 5.6: Histogram of the cross-correlation coefficients between pairs of uncoupled, spontaneously oscillating hair bundles (1225 unique pairs). The standard deviation of this distribution is < 0.02 and no points exceed 0.1.

5.7.3 Amplitude and Coherence of Synchronized Hair Bundles

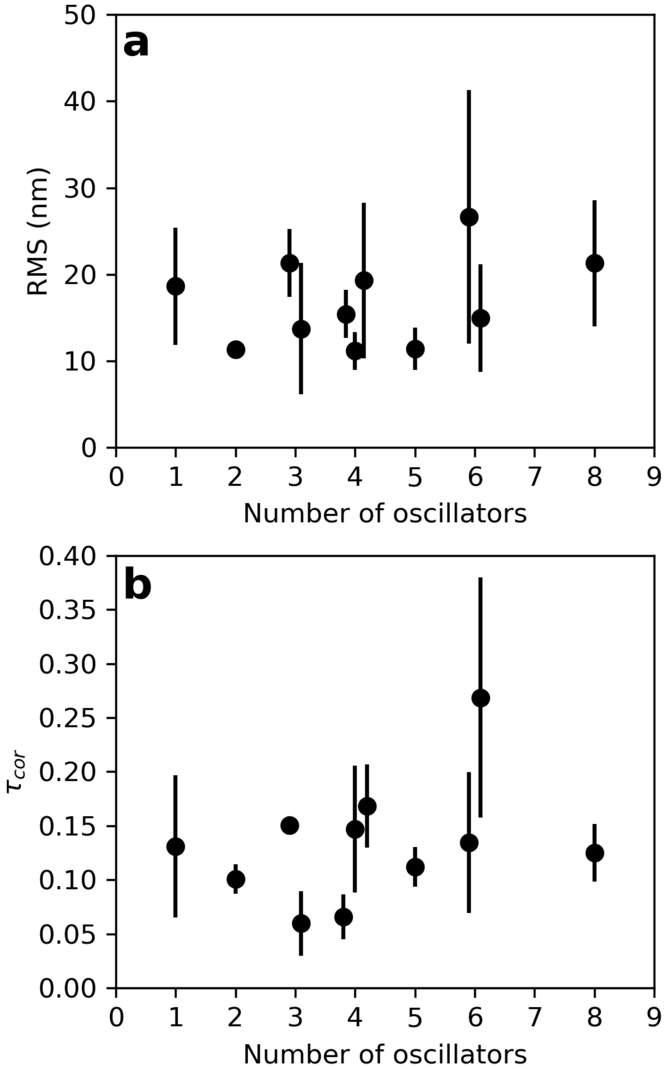

Figure 5.7: (**a-b**) RMS amplitude and normalized correlation time of spontaneous oscillations of coupled hair bundles, obtained for various system sizes. Each hair bundle had a cross-correlation coefficient of at least 0.5 with other bundles in the network in order to ensure the network is synchronized. For both panels, points and error bars represent, respectively, the mean and the standard deviation of the coupled oscillators in the system. For systems with $N > 1$, each data point represents a separate group of coupled hair bundles. The points and error bars at $N = 1$ represent the collective mean and standard deviation across all 10 groups of hair bundles in the absence of coupling.

CHAPTER 6

Chimera States and Frequency Clustering in Coupled Hair-Cell Networks

6.1 Introduction

Partial synchronization has been observed in biological systems such as the abnormal electrical oscillations in cardiac myocytes [85], and electrocorticography recordings preceding epileptic seizures [86, 87]. In these examples, partial synchronization is an undesirable state. However, our experiments and simulations suggest that the inner ear may rely on partial synchronization in order to optimize its ability to detect weak signals.

In this chapter, we identify two additional dynamical states that can occur in networks of coupled hair bundles and explore their potential role in the detection capabilities of the auditory system. The first is the chimera state, defined as a system in which a subset of the coupled oscillators shows mutual synchronization, while the rest oscillate incoherently [88]. Previously it had been believed that identical oscillators, coupled through a mean field, could occupy only two dynamical states: full synchronization or incoherence. This assumption was disproven by the observation of chimeras, first seen in numerical simulations of identical oscillators [89, 90]. As the presence of chimera states depends strongly on the initial conditions of the dynamical system, it was believed that they were too unstable to be observed in an experimental system. However, a decade after their discovery in numerical simulations, chimera states were observed in coupled chemical oscillators [91] and in coupled-map lattices [92]. Chimera states were also shown to arise from heterogeneity in the parameters of the coupled oscillators [88]. As hair cells inherently possess heterogeneity in their size, structure, and time scales of ion-channel dynamics, systems of coupled hair bundles can support chimera states. We here demonstrate signatures of chimeras in experimental recordings obtained from hybrid preparations, in which artificial coupling structures are interfaced with live hair cells. We further explore their potential role in signal detection, with theoretical models that simulate hair bundle dynamics.

The second dynamical phenomenon explored in this study is the occurrence of cluster states, another form of partial synchronization in a coupled system, in which each oscillator synchronizes with one of several clusters. We identify states of frequency clustering in our *in vitro* experiments, lending support to the theory that SOAEs may be generated by frequency clustering of actively oscillating hair bundles. Both types of partial synchronization, chimeras and cluster states, can be reproduced by our simple numerical model of hair cell dynamics, with the introduction of heterogeneity in the set of parameters.

Lastly, we use our numerical model to test its sensitivity to external signals, when the system resides in different dynamical regimes. The system is most frequency selective when poised in the regime of strong coupling, where all oscillators synchronize. However, consistent with a previous numerical study [93], we find that the sensitivity of the system is maximized in the regime of intermediate coupling strength, near the onset of synchronization, in which chimera and cluster states are likely to arise. As hair cells have been shown to utilize a number of adaptive mechanisms, we therefore speculate that the coupled systems within auditory and vestibular end organs may poise themselves at the onset of synchronization in order to optimize their sensitivity to weak, external signals.

6.2 Chimera and Cluster states *in vitro*

We explore the occurrence of partial synchronization in experimental systems of coupled hair cells. To introduce artificial coupling, we use mica flakes and attach them to the tops of groups of hair-cell bundles, following our previously developed methods [94]. The artificial membranes

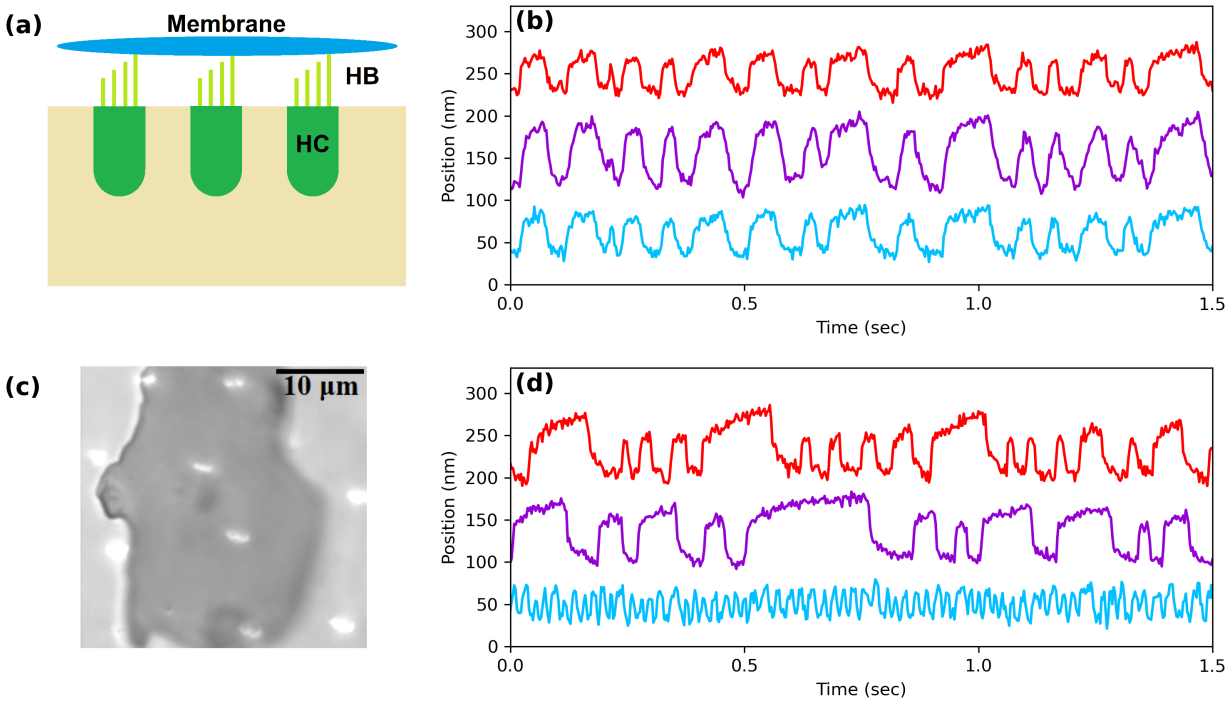

Figure 6.1: (a) Illustration of the experimental system from a side view, displaying the hair cells (HC), hair bundles (HB), and an artificial membrane. (b) Time traces of three spontaneously oscillating hair bundles coupled by an artificial membrane. (c) Top-down images of a biological preparation. The hair bundles appear as white ovals, and the shadow cast by the transparent artificial membrane can be seen in the center of the image. (d) Time traces of the three hair bundles in (b) after removal of the artificial membrane.

are dispersed atop the bundles by introducing them into the endolymph solution, which bathes the apical surface of the sensory epithelium. The mica membranes are thin and transparent, allowing for precise imaging and tracking of the motion of the underlying hair bundles. Further, the mica flakes only minimally modify the mass and drag of the system, allowing us to explore the dynamics of a wide range of system sizes.

As mentioned previously, the bullfrog sacculus is not tonotopically organized, and adjacent hair bundles exhibit up to tenfold differences in their frequencies of spontaneous oscillation. Despite this large frequency dispersion, we find that groups of neighboring hair bundles routinely synchronize upon coupling by the artificial membranes (Fig. 6.1). We characterize the degree of synchronization by calculating the cross-correlation coefficient (Eq. 5.4) between each pair of hair bundles in the system.

Due to the differences in heights of the stereovilli, not every hair bundle within a group makes contact with the artificial membrane above it. Therefore, we define a threshold to determine which hair bundles are coupled to a network of others. To find this threshold, we first calculate the cross-correlation coefficient between many unique pairs of uncoupled hair bundles, with no artificial membranes in the vicinity. The distribution of cross-correlation coefficients is centered around 0 and has a standard deviation ≈ 0.02 (Fig. 5.6). We then set the threshold to be 0.1, more than five standard deviations above the mean and hence unlikely to occur by chance without coupling.

In addition to fully synchronized states, we also observe cases of partial synchronization. We use several techniques to characterize these states. First, we generate space-time plots, where the traces of all the oscillators in the coupled system are plotted as a function of time and the amplitude is represented by color, providing a visual observation of synchronization between the oscillators (Figs. 6.2a, 6.3a). Next, we view the power spectra of the oscillators to confirm that the dominant peaks align at a common frequency for the synchronized portion of the chimera states (Fig. 6.2b) and that multiple common peaks are present for the oscillators of the cluster states (Fig. 6.3b). Finally, we plot the correlation matrices of all of the traces within the coupled systems, in order to give another visual representation of the partial synchronization states. Chimera states contain one group of oscillators with large cross-correlation coefficients between each pair, while all other cross-correlation coefficients are low (Fig. 6.2c). In contrast, cluster states contain multiple groups, where oscillators within a group are strongly correlated with each other but not with those outside of the group (Fig. 6.3c).

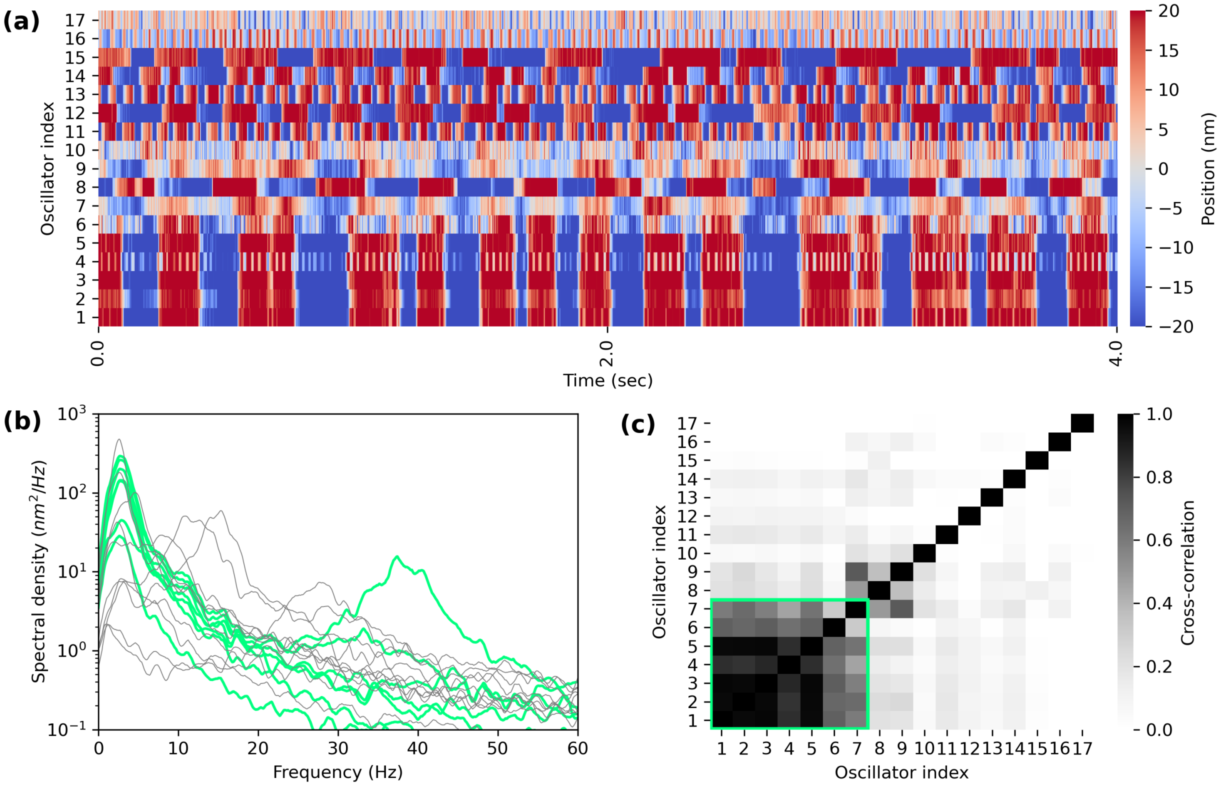

Figure 6.2: (a) Space-time plot of 17 spontaneously oscillating hair bundles coupled with an artificial membrane, exhibiting a chimera state. Oscillators 1-7 are synchronized while the others oscillate incoherently. (b) Power spectra of the 17 coupled oscillators. The 7 synchronized hair bundles are plotting with thick, green curves. (c) Correlation matrix of the coupled hair bundles. The synchronized oscillators are highlighted in the green box.

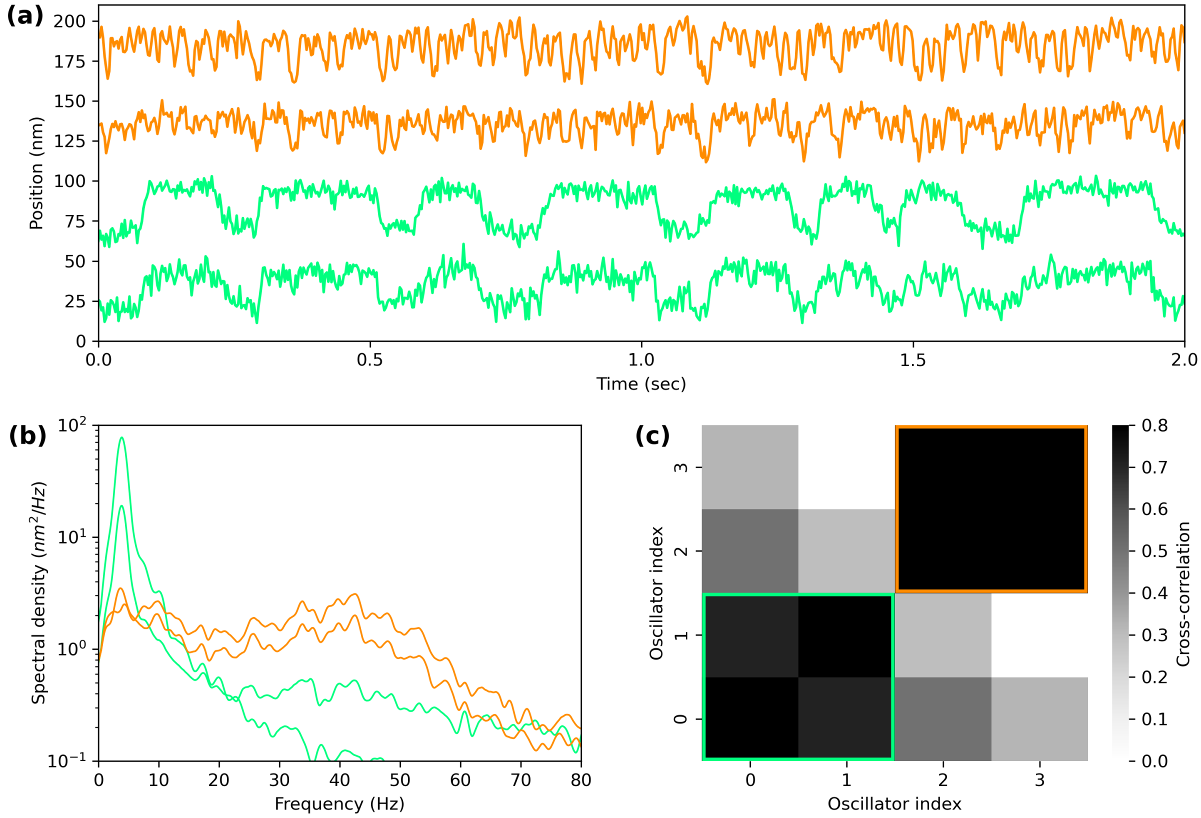

Figure 6.3: (a) Time traces of four spontaneously oscillating hair bundles coupled with an artificial membrane, exhibiting frequency clustering. Orange (top two) and green (bottom two) traces correspond to the high and low frequency clusters, respectively. (b) Power spectra of the four coupled oscillators, plotting in colors corresponding to the traces in (a). (c) Correlation matrix of the coupled hair bundles. The synchronized oscillators are highlighted in colors corresponding to the colors of their traces.

6.3 Numerical Model of coupled hair cells

The dynamics of the j^{th} oscillator in the coupled system are described using the complex variable, $z_j(t) = x_j(t) + iy_j(t)$, and are assumed to be governed by the normal form equation for the supercritical Hopf bifurcation,

$$\begin{aligned} \frac{dz_j}{dt} = (\mu + i\omega_j)z_j - (1 + i\beta_j)|z_j|^2 z_j + k_j(\bar{z} - z_j) \\ + \eta_j(t) + F(t). \end{aligned} \tag{6.1}$$

This simple model reproduces many of the experimentally observed phenomena of hair-cell dynamics, such as the autonomous oscillations and the compressive nonlinear response to external signals [21, 22]. The real part of $z_j(t)$ represents the hair bundle position, while the imaginary part reflects internal parameters of the cell and is not assigned a specific, measurable quantity. μ controls the proximity to the Hopf bifurcation, and ω_j represents the natural frequency at this bifurcation ($\mu = 0$) in the absence of coupling. β_j characterizes the degree of nonlinearity and controls the level of nonisochronicity of the oscillator [68, 95]. In the absence of coupling, and for $\mu > 0$, the system exhibits limit cycle oscillations at radius $\sqrt{\mu}$ and frequency $\Omega_j = \omega_j - \beta_j\mu$. We set the frequency dispersion in our model to approximate that of our experimental data. The limit cycle frequencies are hence uniformly spaced from $\Omega_1 = 1$ to $\Omega_N = 2\sqrt{5} \approx 4.47$. We select an irrational number to avoid spurious mode-locking between oscillators. We set the control parameter to be $\mu = 1$ throughout the study, poising the system deep into the oscillatory regime.

The system is subject to external real-valued forcing, $F(t)$, representing acoustic stimulus or linear acceleration, both of which elicit deflection of the hair bundles in the sacculus. Each oscillator is subject to independent, additive white Gaussian noise, $\eta_j(t)$, with independent real and imaginary parts: $\langle Re(\eta_j(t))Re(\eta_j(t'))\rangle = \langle Im(\eta_j(t))Im(\eta_j(t'))\rangle = 2D\delta(t - t')$, where D is the noise strength of the system.

The dynamics of this system occur at low Reynolds number [76], and we have previously shown that the drag of the artificial membranes is small in comparison to that of the entire coupled system [94]. Further, the mica flakes exhibit little compliance, as we observe coupling and synchronization between pairs of hair bundles with large spacial separation. For these reasons, we have chosen to model the system with mean-field coupling, where each oscillator is weighted by its degree of attachment to the artificial membrane, k_j. The weighted mean field then takes the form,

$$\bar{z} = \frac{1}{N} \sum_{j=1}^{N} k_j z_j, \tag{6.2}$$

where N is the number of oscillators in the system.

6.4 Chimera and Cluster States in the numerical simulations of hair cell dynamics

To explore the dynamic states that can occur in the system of coupled hair cells, we perform numerical simulations based on the theoretical model described above. We vary parameters over a physiologically plausible range, to reproduce the dynamical states observed in the experimental system and determine their potential mechanisms. As mentioned earlier, chimera states can arise from heterogeneity of the model parameters. In the biological system, it is unlikely that the level of attachment to the membrane is identical for all oscillators; hence, we randomly select each k_j value from a uniform distribution spanning 0.2–3.0. This heterogeneity tends to produce the chimera state in our simulations, as only some of the oscillators synchronize, while others oscillate incoherently (Fig. 6.4).

Next, we explore the effects of introducing dispersion into the selection of the β_j parameters, which control the degree of nonisochronicity in individual oscillators. We have previously shown that this parameter, which renders the oscillation frequency of an oscillator dependent on its oscillation amplitude, can lead to chaotic dynamics in the presence of noise [71]. Further, we demonstrated that it can enhance synchronization in a system of coupled nonlinear oscillators, as

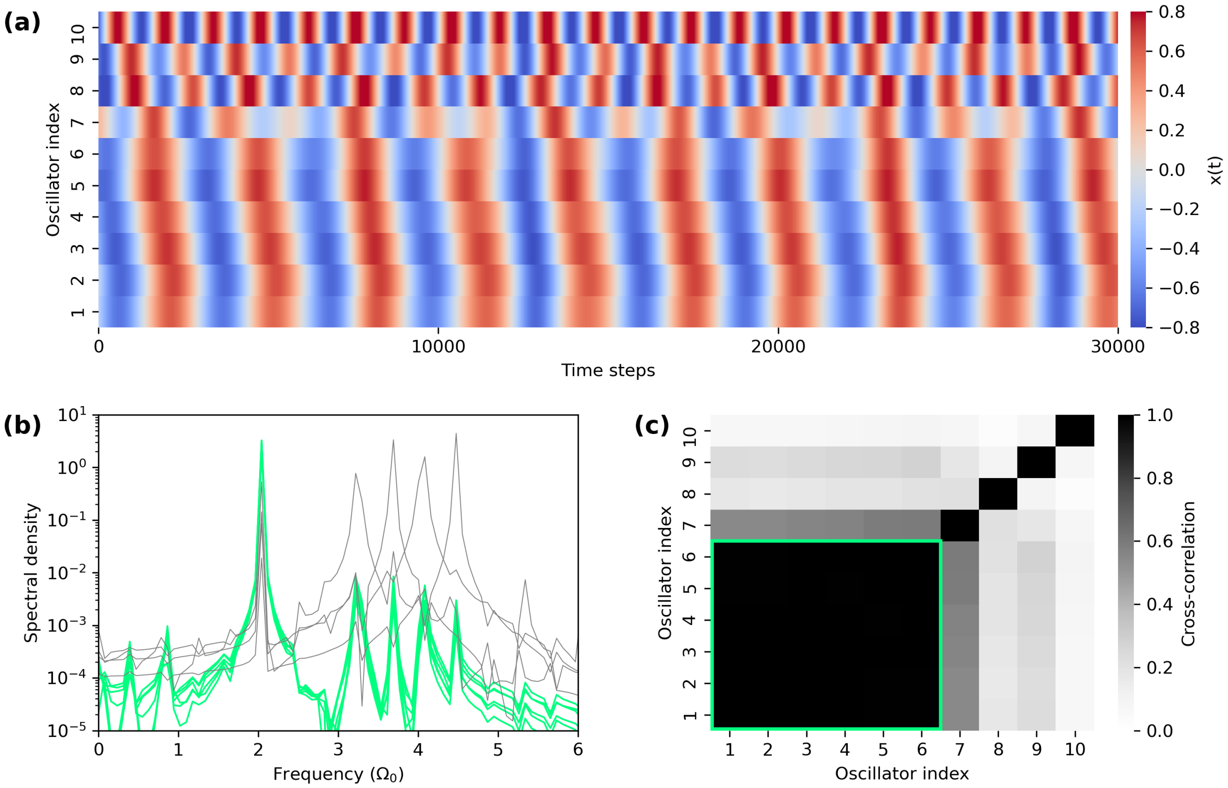

Figure 6.4: (a) Space-time plot of the numerical model exhibiting a chimera state. Oscillators 1-6 synchronize while the others oscillate incoherently. (b) Power spectra of the 10 oscillators, with the synchronized ones plotted with thick, green curves. (c) Correlation matrix of the system. The synchronized oscillators are highlighted in the green box. For all panels, the k_j values were selected from a uniform distribution spanning 0.2–3.0. The simulations were carried out with time steps of $dt = 0.001$, $\beta_j = 0$, and no noise or external forcing.

it allows for a greater shifts in the innate frequencies of oscillation [94]. Here we show that random dispersion in this parameter can also result in multiple frequency clusters (Fig. 6.5). We find that the system forms a 2-cluster state, where oscillators with positive and negative β_j values form separate clusters. The clustering results from coupling, which tends to restrict the dynamics to a smaller region of phase space, thus reducing the amplitude. Since the sign of β_j determines whether an oscillator's frequency increases or decreases with amplitude reduction, two distinct frequencies emerge, forming stable clusters.

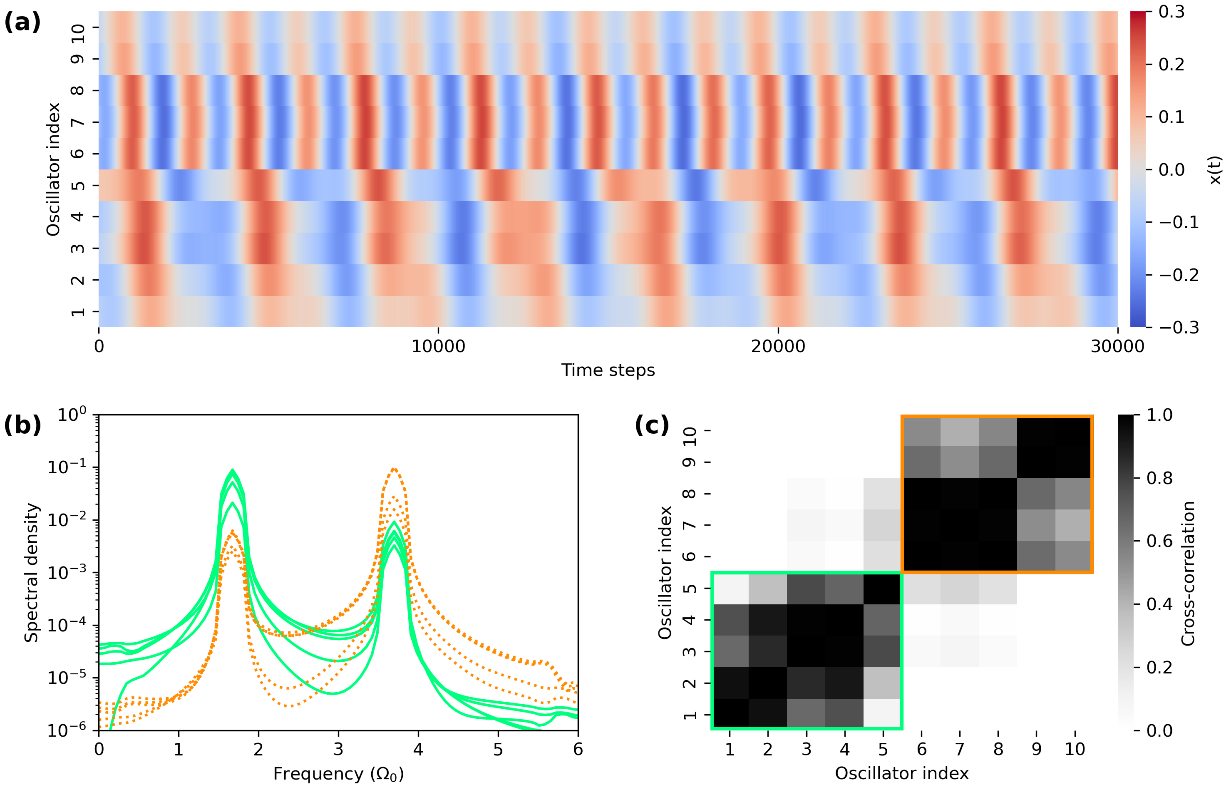

Figure 6.5: (a) Space-time plot of the numerical model exhibiting frequency clustering. (b) Power spectra of the 10 oscillators, with five oscillators in each of the two clusters, as indicated by the solid-green (low frequency) and dotted-orange (high frequency) curves. (c) Correlation matrix of the system. The two clusters are highlighted with colors corresponding to that of their spectral density curves. Simulations were performed with no noise or external forcing, and with time steps of $dt = 0.001$. The coupling strengths were all equal, $k_j = k = 1.5$, and the β_j values were selected from uniform distributions spanning -1–0 for the first five oscillators and 0–1 for the last five oscillators.

6.5 Optimization of Signal Detection

To achieve reliable signal detection, a group of coupled detectors may utilize synchronization. The inherent noise of each component is thus averaged out, and the signal-to-noise ratio (SNR) increases with increasing number of detectors [78]. The drawback to complete synchronization is that the system is then sensitive to only a small range of frequencies surrounding the characteristic frequency. Therefore, total synchronization would be an unfavorable state for the groups of coupled hair cells in the auditory systems, as they are responsible for detecting frequencies that span several octaves. We therefore propose that these systems may utilize a low degree of synchronization in order to improve the SNR without compromising the frequency range of detection.

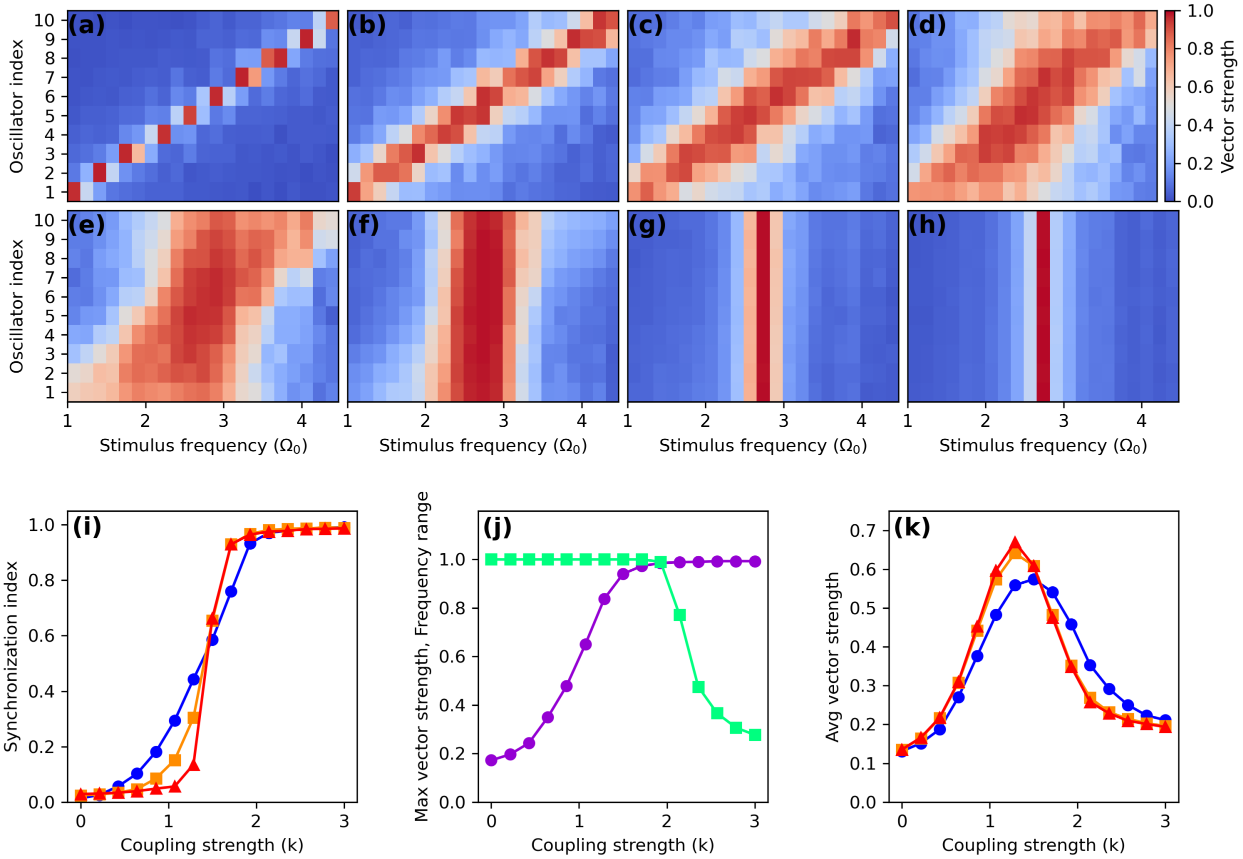

Figure 6.6: (a-h) Sensitivity maps of the numerical model in response to a sinusoidal stimulus with amplitude $f_0 = 0.2$ and noise strength $D = 0.01$ for coupling strengths $k_j = k = 0$, 0.75, 1, 1.25, 1.5, 2, 3, and 5, respectively. (i) Synchronization index as a function of the coupling strength, showing the transition to coherence. (j) Trade-off between the oscillator-average vector strength at the most sensitive stimulus frequency (purple circles) and the fraction of stimulus frequencies for which an oscillator responds with a vector strength of at least 0.2 (green squares). (k) Vector strength averaged across all oscillators and all stimulus frequencies. For (i) and (k), blue circles, orange squares, and red triangles represent system sizes of 10, 100, and 1000 coupled oscillators, respectively.

To visualize this inherent trade-off as a function of the coupling strength, we construct maps that display the sensitivity of every oscillator to a wide range of stimulus frequencies (Fig. 6.6a-h).

We characterize the degree of phase locking, by calculating the vector strength,

$$v_{ij} = \sqrt{\langle \sin(\phi_i - \phi_j) \rangle^2 + \langle \cos(\phi_i - \phi_j) \rangle^2}, \tag{6.3}$$

where ϕ_i and ϕ_j are the phases of two time series and the angle brackets denote the time average. To quantify the sensitivity, we calculate the vector strength between the stimulus waveform and the response of an oscillator.

To characterize the degree of synchronization within the coupled system we calculate the average vector strength between all pairs of oscillators in the absence of stimulus. This synchronization index is 1 for perfectly synchronized oscillators and approximately 0 for incoherent motion. We see that the transition to synchronization occurs at a coupling strength around $k_j = k = 1.5$ and becomes more abrupt for larger system sizes (Fig. 6.6i).

The sensitivity maps show the strongest response at intermediate levels of coupling strength, near the onset of synchronization. If the coupling is too weak, the dynamics are incoherent, and the oscillators are more susceptible to noise. However, if the coupling is too strong, the system is limited to detecting only a small range of frequencies. To see this trade-off more explicitly, we average the vector strengths over all oscillators and take the maximum across all stimulus frequencies (maximum oscillator-average vector strength). We plot this measure as a function of coupling strength, along with the fraction of stimulus frequencies in which at least one oscillator has a vector strength above 0.2 (Fig. 6.6j). This trade-off between maximum vector strength and frequency range of detection produces a peak in the average vector strength across all stimulus frequencies and detectors (Fig. 6.6k). These results suggest that a coupled system responsible for detecting a wide range of frequencies will achieve optimal performance when poised at the onset of synchronization.

Vestibular end organs display varying degrees of coupling between hair cells, likely involving the response of multiple oscillators to achieve reliable signal detection. The bullfrog sacculus is innervated in a way that supports this assumption, with afferent fibers synapsing onto multiple hair cells [19]. Secondly, to achieve reliable detection, the system should be sensitive to different frequencies, as the airborne and ground-borne vibrations of interest contain energy distributed across a range of low frequencies. We therefore propose that the sacculus is poised at the onset of synchronization in order to optimize signal detection.

6.6 Discussion

The auditory and vestibular systems have provided a testing ground for concepts from bifurcation theory and nonlinear dynamics [21, 23, 62, 96]. These sensory systems serve different purposes but all rely on hair cells to perform detection of sound, vibration, or acceleration. Active hair cells of these sensory systems have displayed Hopf bifurcations, saddle-node on an invariant circle (SNIC) bifurcations [97], and the quasiperiodic transition to chaos [64]. The dynamics of hair cells have been described by limit cycles, stable fixed points, chaotic attractors, and amplitude-death states. How these dynamical states shape the response of the full system to external signals remains an open question.

As these sensory systems impose different requirements on the sensitivity, frequency selectivity, temporal resolution, and dynamic range of detection, the various organs may have developed different dynamical regimes in which to reside, in order to achieve the signal detection properties of interest. Individual hair cells that comprise these systems have been shown to be versatile, displaying different response characteristics under different mechanical loads or other perturbations [98]. For example, while the bullfrog sacculus is not a frequency-selective organ, when hair cells within it are subject to appropriate experimental manipulation, they were shown to be capable of frequency-selective detection expected for auditory organs. Hence, we expect that differences in the detection properties of the sensory organs lie not only in different properties of individual cells, but also in the coupling conditions and emergent dynamical states of the full system. It is therefore important to understand the different dynamical states that these coupled oscillators can exhibit, in order to understand the full range of signal detection properties that the sensory systems can display.

In the present work, we observe two dynamical states that, to the best of our knowledge, have not been previously observed in auditory or vestibular systems. We measure the response of active hair bundles, coupled together with artificial membranes of different sizes, and obtain experimental observations of chimera states and cluster states. Both of these dynamical states can be reproduced with a simple numerical model with the inclusion of heterogeneity of the parameters.

One of the signatures of the active process in the inner ear takes the form of otoacoustic emissions, which have been used as a probe of the auditory nonlinearities and internal dynamics *in vivo*. The mechanism of their generation by the auditory system is, however, not yet fully established. Our experimental data supports the theory that they arise from frequencies clustering of coupled active oscillators within the inner ear, as we observe frequency clustering *in vitro* in small groups of mechanically coupled hair bundles.

Both the cluster states and chimera states are forms of partial synchronization and arise at intermediate levels of coupling strength, near the onset of total synchronization. We find that the numerical model achieves the greatest sensitivity to external stimulus when poised in this regime. It exhibits a balance in the inherent trade-off between the frequency range of signal detection and the number of oscillators that phase lock to the external signals. Therefore, we propose that these partial synchronization states may occur *in vivo* in systems of coupled hair bundles, if these systems are poised in the optimal regime for signal detection.

REFERENCES

[1] A. J. Hudspeth. Integrating the active process of hair cells with cochlear function. *Nat. Rev. Neurosci.*, 15:600, 2014.

[2] B. Leshowitz. Measurement of the two-click threshold. *J. Acoustical Soc. of America*, 49:462, 1971.

[3] T. Reichenbach and A. J. Hudspeth. The physics of hearing: fluid mechanics and the active process of the inner ear. *Rep. Prog. Phys.*, 77(7):076601, 2014.

[4] M. LeMasurier and P. G. Gillespie. Hair-cell mechanotransduction and cochlear amplification. *Neuron*, 48(3):403, 2005.

[5] M. A. Vollrath, K. Y. Kwan, and D. P. Corey. The micromachinery of mechanotransduction in hair cells. *Annu. Rev. Neurosci.*, 30:339, 2007.

[6] D. Ó Maoiléidigh and A. J. Ricci. A bundle of mechanisms: Inner-ear hair-cell mechanotransduction. *Trends Neurosci.*, 42(3):221, 2019.

[7] A. J. Hudspeth. Making an effort to listen: mechanical amplification in the ear. *Neuron*, 59(4):530, 2008.

[8] M. E. Benser, R. E. Marquis, and A. J. Hudspeth. Rapid, active hair bundle movements in hair cells from the bullfrog's sacculus. *J. Neurosci.*, 16(18):5629, 1996.

[9] P. Martin, D. Bozovic, Y. Choe, and A. J. Hudspeth. Spontaneous oscillation by hair bundles of the bullfrog's sacculus. *J. Neurosci.*, 23(11):4533, 2003.

[10] A. C. Crawford and R. Fettiplace. The mechanical properties of ciliary bundles of turtle cochlear hair cells. *J. Physiol.*, 364(1):359, 1985.

[11] P. Martin, A. J. Hudspeth, and F. Jülicher. Comparison of a hair bundle's spontaneous oscillations with its response to mechanical stimulation reveals the underlying active process. *Proc. Natl. Acad. Sci. U.S.A.*, 98(25):14380, 2001.

[12] P. Martin and A. J. Hudspeth. Active hair-bundle movements can amplify a hair cell's response to oscillatory mechanical stimuli. *Proc. Natl. Acad. Sci. U.S.A.*, 96(25):14306, 1999.

[13] D. T. Kemp. Evidence of mechanical nonlinearity and frequency selective wave amplification in the cochlea. *Arch. Oto-Rhino-Laryngol.*, 224(1–2):37, 1979.

[14] C. A. Shera. Mechanisms of mammalian otoacoustic emission and their implications for the clinical utility of otoacoustic emissions. *Ear Hear.*, 25(2):86, 2004.

[15] C. Bergevin, G. A. Manley, and C. Köppl. Salient features of otoacoustic emissions are common across tetrapod groups and suggest shared properties of generation mechanisms. *Proc. Natl. Acad. Sci. U.S.A.*, 112(11):3362, 2015.

[16] Y. Roongthumskul, D. Ó Maoiléidigh, and A. J. Hudspeth. Bilateral spontaneous otoacoustic emissions show coupling between active oscillators in the two ears. *Biophys. J.*, 116(10):2023, 2019.

[17] A. Vilfan and T. Duke. Frequency clustering in spontaneous otoacoustic emissions from a lizard's ear. *Biophys. J.*, 95(10):4622, 2008.

[18] F. Fruth, F. Jülicher, and B. Lindner. An active oscillator model describes the statistics of spontaneous otoacoustic emissions. *Biophys. J.*, 107(4):815, 2014.

[19] M. S. Smotherman and P. M. Narins. Hair cells, hearing and hopping: A field guide to hair cell physiology in the frog. *J. Exp. Biol.*, 203(15):2237, 2000.

[20] P. M. Narins and E. R. Lewis. The vertebrate ear as an exquisite seismic sensor. *J. Acoust. Soc. Am.*, 76(5):1384, 1984.

[21] V. M. Eguiluz, M. Ospeck, Y. Choe, A. J. Hudspeth, and M. O. Magnasco. Essential nonlinearities in hearing. *Phys. Rev. Lett.*, 84(22):5232, 2000.

[22] A. Kern and R. Stoop. Essential role of couplings between hearing nonlinearities. *Phys. Rev. Lett.*, 91(12):128101, 2003.

[23] S. Camalet, T. Duke, F. Jülicher, and J. Prost. Auditory sensitivity provided by self-tuned critical oscillations of hair cells. *Proc. Natl. Acad. Sci. U.S.A.*, 97(7):3183, 2000.

[24] R. Shlomovitz et al. Low frequency entrainment of oscillatory bursts in hair cells. *Biophys. J.*, 104:1661, 2013.

[25] A. R. Milewski, D. Ó Maoiléidigh, J. D. Salvi, and A. J. Hudspeth. Homeostatic enhancement of sensory transduction. *Proc. Natl. Acad. Sci. U.S.A.*, 114:E6794, 2017.

[26] A. Garfinkel et al. Quasiperiodicity and chaos in cardiac fibrillation. *J. Clin. Inv.*, 99(2):305, 1997.

[27] Y. H. Kim et al. Spatiotemporal complexity of ventricular fibrillation revealed by tissue mass reduction in isolated swine right ventricle. further evidence for the quasiperiodic route to chaos hypothesis. *Amer. Soc. Clin. Inv.*, 100(10):2486, 1997.

[28] E. N. Lorenz. Deterministic nonperiodic flow. *J. of the Atmos. Sci.*, 20(2):130, 1963.

[29] S. H. Strogatz. *Nonlinear Dynamics and Chaos*. Addison-Wesley Publishing Company, Boston, Massachusetts, 1994.

[30] J-P. Eckmann and D. Ruelle. Ergodic theory of chaos and strange attractors. *Rev. Mod. Phys.*, 57(3):617, 1985.

[31] T. Sauer, J. A. Yorke, and M. Casdagli. Embedology. *J. Stat. Phys.*, 65(3):579, 1991.

[32] F. Takens. Detecting strange attractors in turbulence. *Dynamical Systems and Turbulence, Warwick 1980*, 898:366, 1981.

[33] H. D. I. Abarbanel and M. B. Kennel. Local false nearest neighbors and dynamical dimensions from observed chaotic data. *Phys. Rev. E.*, 47(5):3057, 1993.

[34] H. D. I. Abarbanel. *Analysis of Observed Chaotic Data*. Springer Science & Business Media, New York, 1996.

[35] A. M. Fraser and H. L. Swinney. Independent coordinates for strange attractors from mutual information. *Phys. Rev. A.*, 33(2):1134, 1986.

[36] D. T. Kaplan and L. Glass. Direct test for determinism in a time series. *Phys. Rev. Lett.*, 68(4):427, 1992.

[37] M. B. Kennel, R. Brown, and H. D. I. Abarbanel. Determining embedding dimension for phase-space reconstruction using a geometrical construction. *Phys. Rev. A.*, 45(6):3403, 1992.

[38] P. Grassberger and I. Procaccia. Characterization of strange attractors. *Phys. Rev. Lett.*, 50(5):346, 1983.

[39] A. Ben-Mizrachi, I. Procaccia, and P. Grassberger. Characterization of experimental (noisy) strange attractors. *Phys. Rev. A.*, 29(2):975, 1984.

[40] M. Ding, C. Grebogi, E. Ott, T. Sauer, and J. A. Yorke. Estimating correlation dimension from a chaotic time series: when does plateau onset occur? *Physica D*, 69:404, 1993.

[41] N. Fenichel. Persistence and smoothness of invariant manifolds for flows. *Indiana Univ. Math. J.*, 21(3):193, 1971.

[42] J. H. Curry and J. A. Yorke. A transition from hopf bifurcation to chaos: computer experiments with maps in R 2. In J. C. Martin, N. G. Markley, and W. Perrizo, editors, *The Structure of Attractors in Dynamical Systems, Springer Notes in Mathematics*, volume 668, pages 48–66. Springer, 1978.

[43] D. G. Aronson, M. A. Chory, R. P. McGehee, and G. R. Hall. Bifurcations from an invariant circle for two-parameter families of maps of the plane: A computer-assisted study. *Comm. Math. Phys.*, 83(3):303, 1982.

[44] V. S. Afraimovich and L. P. Shilnikov. On invariant two-dimensional tori, their breakdown and stochasticity. In *Methods of the Qualitative Theory of Differential Equations*, pages 3–26. 1983.

[45] A. Shilnikov, L. Shilnikov, and D. Turaev. On some mathematical topics in classical synchronization. a tutorial. *Int. J. Bifurcation and Chaos*, 14(7):2143, 2003.

[46] A. H. Nayfeh and B. Balachandran. *Applied Nonlinear Dynamics*. Wiley-VCH Verlag GmbH, 2007.

[47] R. Hegger and H. Kantz. Embedding of sequences of time intervals. *Europhys. Lett.*, 38(4):267, 1997.

[48] M. T. Martin, A. Plastino, and O. A. Rosso. Generalized statistical complexity measures: Geometrical and analytical properties. *Physica A*, 369:439, 2006.

[49] C. Bandt and B. Pompe. Permutation entropy: A natural complexity measure for time series. *Phys. Rev. Lett.*, 88(17):174102, 2002.

[50] O. A. Rosso, H. A. Larrondo, M. T. Martin, A. Plastino, and M. A. Fuentes. Distinguishing noise from chaos. *Phys. Rev. Lett.*, 99(15):154102, 2007.

[51] W. Gekelman, B. Van Compernolle, T. DeHaas, and S. Vincena. Chaos in magnetic flux ropes. *Plas. Phys. Cont. Fus.*, 56:064002, 2014.

[52] J. E. Maggs and G. J. Morales. Permutation entropy analysis of temperature fluctuations from a basic electron heat transport experiment. *Plas. Phys. Cont. Fus.*, 55:085015, 2013.

[53] A. N. Kolmogorov. A new metric invariant of transitive dynamical systems and automorphisms of lebesgue spaces. *Dokl. Akad. Nauk. SSSR*, 119:861, 1958.

[54] H. Kantz and T. Schreiber. *Nonlinear Time Series Analysis*. Cambridge University Press, Cambridge, England, 1997.

[55] T. Schreiber. Measuring information transfer. *Phys. Rev. Lett.*, 85(2):461, 2000.

[56] L. Dinis, P. Martin, J. Barral, J. Prost, and J. F. Joanny. Fluctuation-response theorem for the active noisy oscillator of the hair-cell bundle. *Phys. Rev. Lett.*, 109(16):160602, 2012.

[57] T. Risler, J. Prost, and F. Jülicher. Universal critical behavior of noisy coupled oscillators. *Phys. Rev. Lett.*, 93(17):175702, 2004.

[58] Y. Roongthumskul, R. Shlomovitz, R. Bruinsma, and D. Bozovic. Phase slips in oscillatory hair bundles. *Phys. Rev. Lett.*, 110(14):148103, 2013.

[59] V. S. Anishchenko, V. Astakhov, A. Neiman, T. Vadivasova, and L. Schimansky-Geier. *Nonlinear Dynamics of Chaotic and Stochastic Systems*. Springer-Verlag Berlin Heidelberg, 2007.

[60] D. S. Goldobin and A. Pikovsky. Synchronization and desynchronization of self-sustained oscillators by common noise. *Phys. Rev. E*, 71:045201, 2005.

[61] D. S. Goldobin and A. Pikovsky. Antireliability of noise-driven neurons. *Phys. Rev. E*, 73(6):061906, 2006.

[62] A. B. Neiman, K. Dierkes, B. Lindner, L. Han, and A. L. Shilnikov. Spontaneous voltage oscillations and response dynamics of a hodgkin-huxley type model of sensory hair cells. *J. Math. Neurosci.*, 1:11, 2011.

[63] C. Gan. Noise-induced chaos in a quadratically nonlinear oscillator. *Chaos, Solitons & Fractals*, 30:920, 2006.

[64] J. Faber and D. Bozovic. Chaotic dynamics of inner ear hair cells. *Sci. Rep.*, 8:3366, 2018.

[65] R. A. Eatock. Adaptation in hair cells. *Ann. Rev. Neurosci.*, 23:285, 2000.

[66] J. Barral, F. Jülicher, and P. Martin. Friction from transduction channels' gating affects spontaneous hair-bundle oscillations. *Biophys. J.*, 114:425, 2018.

[67] R. Stoop, J. J. V. D. Vyver, and A. Kern. Limit cycles, noise, and chaos in hearing. *Micros. Res. Techniq.*, 63(6):400, 2004.

[68] J. Faber and D. Bozovic. Noise-induced chaos and signal detection by the nonisochronous hopf oscillator. *Chaos*, 29:043132, 2019.

[69] J. E. Marsden and M. McCracken. *The Hopf Bifurcation and its Applications*. Springer-Verlag, New York, 1976.

[70] A. Pikovsky, M. Rosenblum, and J. Kurths. *Synchronization: A Universal Concept in Nonlinear Sciences*. Cambridge University Press, 2001.

[71] J. Faber and D. Bozovic. Chaotic dynamics enhance the sensitivity of inner ear hair cells. *Sci. Rep.*, 9:18394, 2019.

[72] J.-Y. Tinevez, F. Jülicher, and P. Martin. Unifying the various incarnations of active hair-bundle motility by the vertebrate hair cell. *Biophys. J.*, 93:4053, 2007.

[73] C. Zhou and J. Kurths. Noise-induced phase synchronization and synchronization transitions in chaotic oscillators. *Phys. Rev. Lett.*, 88(23):230602, 2002.

[74] D. L. Gonzalez and O. Piro. Chaos in a nonlinear driven oscillator with exact solution. *Phys. Rev. Lett.*, 50(12):870, 1983.

[75] R. B. Patuzzi and M. L. Thompson. Cochlear efferent neurones and protection against acoustic trauma: Protection of outer hair cell receptor current and interanimal variability. *Hear. Res.*, 54(1):45, 1991.

[76] N. Ciganović, A. Wolde-Kidan, and T. Reichenbach. Hair bundles of cochlear outer hair cells are shaped to minimize their fluid-dynamic resistance. *Sci. Rep.*, 7:3609, 2017.

[77] A. S. Pikovsky and J. Kurths. Coherence resonance in a noise-driven excitable system. *Phys. Rev. Lett.*, 78(5):775, 1997.

[78] K. Dierkes, F. Jülicher, and B. Lindner. A mean-field approach to elastically coupled hair bundles. *Eur. Phys. J. E*, 35:37, 2012.

[79] T-Y. Zhang, S. Ji, and D. Bozovic. Synchronization of spontaneous active motility of hair cell bundles. *PLOS One*, 10(11), 2015.

[80] D. M. Freeman, C. C. Abnet, W. Hemmert, B. S. Tsai, and T. F. Weiss. Dynamic material properties of the tectorial membrane: a summary. *Hear. Res.*, 180:1, 2003.

[81] F. Jaramillo and K. Wiesenfeld. Mechanoelectrical transduction assisted by brownian motion: a role for noise in the auditory system. *Nat. Neurosci.*, 1(5):384, 1998.

[82] A. Garfinkel, M. L. Spano, W. L. Ditto, and J. N. Weiss. Controlling cardiac chaos. *Science*, 257:1230, 1992.

[83] J. F. Trahan. Stokes drag on a thin circular disk moving edgewise midway between parallel plane boundaries. *J. Fluids Eng.*, 128:887, 2006.

[84] V. Bormuth, J. Barral, J-F. Joanny, F. Jülicher, and P. Martin. Transduction channels' gating can control friction on vibrating hair-cell bundles in the ear. *Proc. Natl. Acad. Sci. U.S.A.*, 111(20):7185, 2014.

[85] D. Sato, L-H. Xie, A. A. Sovari, D. X. Tran, N. Morita, F. Xie, H. Karagueuzian, A. Garfinkel, J. N. Weiss, and Z. Qu. Synchronization of chaotic early afterdepolarizations in the genesis of cardiac arrhythmias. *Proc. Natl. Acad. Sci. U.S.A.*, 106:2983, 2009.

[86] R. G. Andrzejak, C. Rummel, F. Mormann, and K. Schindler. All together now: Analogies between chimera state collapses and epileptic seizures. *Sci. Rep.*, 6:23000, 2016.

[87] C. Lainscsek, N. Rungratsameetaweemana, S. S. Cash, and T. J. Sejnowski. Cortical chimera states predict epileptic seizures. *Chaos*, 29(12):121106, 2019.

[88] M. J. Panaggio and D. M. Abrams. Chimera states: Coexistence of coherence and incoherence in networks of coupled oscillators. *Nonlinearity*, 28(3):R67, 2015.

[89] Y. Kuramoto and D. Battogtokh. Coexistence of coherence and incoherence in nonlocally coupled phase oscillators. *Nonlin. Phenom. Complex Syst.*, 5:380, 2002.

[90] D. M. Abrams and S. H. Strogatz. Chimera states for coupled oscillators. *Phys. Rev. Lett.*, 93(17):174102, 2004.

[91] M. R. Tinsley, S. Nkomo, and K. Showalter. Chimera and phase-cluster states in populations of coupled chemical oscillators. *Nat. Phys.*, 8(9):662, 2012.

[92] A. M. Hagerstrom, T. E. Murphy, R. Roy, P. Hövel, I. Omelchenko, and E. Schöll. Experimental observation of chimeras in coupled-map lattices. *Nat. Phys.*, 8(9):658, 2012.

[93] C-Q. Wang, A. Pumir, N. B. Garnier, and Z-H. Liu. Explosive synchronization enhances selectivity: Example of the cochlea. *Front. Phys.*, 12(5):128901, 2017.

[94] J. Faber, H. Li, and D. Bozovic. Synchronization and chaos in systems of coupled inner-ear hair cells. *Phys. Rev. Res.*, 3(1):013266, 2021.

[95] Y. Roongthumskul, J. Faber, and D. Bozovic. Dynamics of mechanically coupled hair-cell bundles of the inner ear. *Biophys. J.*, 120:205, 2021.

[96] S. Ji, D. Bozovic, and R. Bruinsma. Amphibian sacculus and the forced kuramoto model with intrinsic noise and frequency dispersion. *Phys. Rev. E*, 97:042411, 2018.

[97] L. Fredrickson-Hemsing, C. E. Strimbu, Y. Roongthumskul, and D. Bozovic. Dynamics of freely oscillating and coupled hair cell bundles under mechanical deflection. *Biophys. J.*, 102(8):1785, 2012.

[98] J. D. Salvi, D. Ó Maoiléidigh, B. A. Fabella, M. Tobin, and A. J. Hudspeth. Control of a hair bundle's mechanosensory function by its mechanical load. *Proc. Natl. Acad. Sci. U.S.A.*, 112(9):E1000, 2015.